UNIVERSITY OF CALIFORNIA,
IRVINE

More Efficient Dynamic Operation of Fueled Dispatchable Power Generation in High Renewable Penetration Grid

DISSERTATION

submitted in partial satisfaction of the requirements
for the degree of

DOCTOR OF PHILOSOPHY

in Mechanical Engineering

by

Gi Jung Lee

Dissertation Committee:

Professor Jack Brouwer, Chair
Professor Scott Samuelsen
Professor Yun Wang

2022

DEDICATION

To

my lovely wife, parents and friends

TABLE OF CONTENTS

Page

LIST OF FIGURES

Page

LIST OF TABLES

Page

ACKNOWLEDGEMENTS

I express my sincere gratitude to my advisor and committee chair, Professor Jack Brouwer for his guidance and support. He has always been a great mentor, professionally and personally. His enthusiasm for renewable energy and hydrogen has been a true inspiration and encouraged me to further pursue my career in these areas. His continuous support has made this work possible.

I thank Professor Scott Samuelsen for establishing the Advanced Power and Energy Program here in UC Irvine which has opened so many doors to graduate students like myself to pursue their professional goals and passions through many exciting and impactful projects in this amazing program.

I thank my members of my dissertation committee and qualifying exam committee, Professor Scott Samuelsen, Professor Yun Wang, Professor Manuel Gamero, and Professor Bagherzadeh for serving on the committees and providing valuable advices on this work.

I express my appreciation to Dr. Luca Mastropasqua and Dr. Alireza Saeedmanesh, without whom this work was not possible. Luca has been a professional mentor and great friend. From day-to-day interaction with him, I have learned tremendously about how to become a better engineer, researcher, and professional. Alireza has helped me learn STRIDES tool, which I used to model SOFC-GT hybrid system for my dissertation. His willingness to help, attention to details, and profound subject knowledge are qualities that I looked up to and make me wish I can help others in a way as he has done with me.

I thank all of my colleagues I worked together in and out of the Advanced Power and Energy Program (APEP), especially Dr. Robert Flores from the APEP and Dr. Zexuan Xu and Dr. Alan

Di Vittorio from Lawrence Berkeley National Laboratory for their helps and co-authoring the publications that are essential parts of this dissertation.

I would like to acknowledge my dad, mom, and brother. Though we live far away from each other, each of them all hold a special place in my heart.

Last, I thank my lovely wife, Sojin, who has been with me along this journey. She has been a great wife and my best friend supporting me unconditionally. She celebrated my success with me and encouraged me to go forward while studying for her bar exam and working tirelessly for her own career during this pandemic. During this hard time, she consistently put the needs of her family before her own and proved to be a selfless individual. Without her love and support, I would not be able to overcome all the hardships and complete my study. I cannot thank her enough for her and I love her deeply.

VITA

Gi Jung Lee

Education

2010-2016	B.S in Mechanical Engineering
	Duke University
2016-2019	M.S in Mechanical Engineering
	Advanced Power and Energy Program, University of California, Irvine
2019-2022	Ph.D in Mechanical Engineering
	Advanced Power and Energy Program, University of California, Irvine

Fields of Study

High temperature energy conversion systems focusing on solid oxide fuel cell and gas turbine

Grid operation focusing on renewable energy integration, climate change impacts, and hydrogen blending

Publications

"Dynamic Modeling of Solid-Oxide Fuel Cell Gas Turbine Hybrid Technology to Complement High Levels of Renewables", In Review

Lee, G.J., Mastropasqua, L., and Brouwer, J.

"More Efficient Dynamic Operation of Dispatchable Power Generation to Complement High Levels of Solar and Wind: Part II. Grid Simulation and Dispatch Strategies", Applied Energy, In Review

Lee, G.J., Flores, R.J., Brouwer, J., Xu, Z., and Di Vittorio, A.V.

"More Efficient Dynamic Operation of Dispatchable Power Generation to Complement High Levels of Solar and Wind: Part I. Fleet Modeling and Simulation", Applied Energy, In Review

Lee, G.J., Flores, R.J., and Brouwer, J.

ABSTRACT OF DISSERTATION

More Efficient Dynamic Operation of Fueled Dispatchable Power Generation in High Renewable Penetration Grid

by

Gi Jung Lee

Doctor of Philosophy in Mechanical Engineering

University of California, Irvine, 2022

Professor Jack Brouwer, Chair

To combat climate change and air pollution many electric utilities have implemented standards to prioritize power generated from renewable sources. However, their intermittency and dynamics have posed challenges to high use of these non-dispatchable resources such as solar and wind. Climate change will further complicate these challenges and thus, the reliable and efficient operation of the electric utility grid network. Among many available options capable of complementing the renewables, natural gas combined-cycle (NGCC) technology, with its high efficiency and flexibility, has demonstrated its potential as a load-following plant. The fleet of load-followers needs to operate at lower part-load and more dynamic operating conditions for extended periods of time to complement the non-dispatchable renewables. In this study, current and next-generation load-following technologies are physically simulated to determine implications of their dynamic operation in a current and future grid affected by increased renewables. For the current load-following technology, novel NGCC control and dispatch strategies are applied to improve an individual plant and grid performance. Compared to the respective base case, the control strategies have improved efficiency by up to 58 percentage points and dispatch strategies have reduced grid wide GHG emissions up to 54%. Furthermore, climate change impacts on grid operation are examined as they affect the renewable dynamics. In response,

not only has capacity of the load-followers been increased but also their operation has become more dynamic to maintain grid reliability. In addition to dynamic dispatchability, transitioning to a 100% renewable grid requires power systems to be fuel-flexible with near-zero emissions. In this context, solid-oxide fuel cell gas turbine (SOFC-GT) hybrid technology is explored as a next-generation load-follower. The proposed system can achieve net efficiency >70% at distributed energy scale (100 kW_{el}). With a developed control strategy, the system can complement high levels of non-dispatchable renewables without incurring component degradation and with its high part-load efficiency maintained >50%. On the other hand, the system can seamlessly operate with up to 72.9%v of hydrogen without any configuration modifications. These conclusions increase confidence that dynamic dispatch of highly efficient and renewable-fueled load-following technologies can facilitate a smooth transition into highly renewable electric grids.

1. Introduction

While access to electricity is indispensable for our lives, electricity and heat generation was responsible for two-thirds of the world's CO_2 emissions in 2014 [1]. These anthropogenic activities have accelerated the change in global climate and environment [2]. Ranging from global warming to desertification and water maldistribution, consequences of changes in climate have already appeared in many forms; moreover, the change in climate is likely to increase the frequency and severity of extreme weather phenomena [2]. Although restricted to specific parts of the world, these damages can potentially increase drastically if adequate steps are not taken.

To counteract climate change impacts, the second largest CO_2 emitting nation, the United States has been enforcing political and bureaucratic measures. At the federal level, the United States has been providing tax credits and financial aid programs to encourage electricity production by renewable means. For example, the Production Tax Credit (PTC) and Investment Tax Credit (ITC) policies respectively allow tax credit based on electricity generated by eligible energy resources and the amount invested to build the eligible infrastructure [3]. In addition, the U.S. Department of Energy's Loan Program has guaranteed billions of dollars to "bridge the clean energy financing gap" for advanced fossil energy and innovative renewable technologies at their initial deployment stages [4]. At the state level, some states have been implementing more stringent goals and policies for emissions reduction and increased shares of renewables than others. Specifically, with the establishment of Renewables Portfolio Standard (RPS) under Senate Bill 1078 as early as in 2002, the state of California has been proposing one of the most progressive clean-energy goals in the world [5]. Signed into law in 2018, SB100 has accelerated the California's RPS to 60 percent by 2030 and set a carbon-free goal by 2045 for its electricity sector [5].

Such goals can only be accomplished when the increase in renewable infrastructures is accompanied by methods to better integrate them with the existing energy infrastructures. For reliable and effective integration of the renewable technologies to meet these targets, the significance of complementing technologies in grid operation has greatly increased. The range of these technologies varies from different types of energy storage to various dispatchable generators such as hydropower, geothermal and fossil-fuels. Among many available technologies, one promising option is, still, to operate conventional power generation units more dynamically [6]. In the state of California and many places around the world, the natural gas combined cycle (NGCC) power plants provide most of the electricity and are dynamically dispatched to enable integration of the non-dispatchable renewable resources such as solar and wind [7]. As these renewable sources are increasingly prioritized over the conventional one, the NGCC plants are to be operated even more dynamically in utility grid networks for grid reliability [7].

As jurisdictions are striving for the carbon-free and pollution-free electricity sector, a new complementing technology needs to replace the combustion-based technology in grids. One of the promising future technologies that can provide dynamic response to sustain high renewable grid penetration and can also achieve ultra-high electrical efficiency and ultra-low pollutant emissions at variable scales is to hybridize solid-oxide fuel cell and gas turbine technology [8,9]. This dissertation will discuss the application and demonstration of the NGCC as the existing load-following technology in a high renewable penetrated grid and at the same time, design, control, and application of the solid-oxide fuel cell-gas turbine (SOFC-GT) hybrid system as a future load-following technology within the same grid.

This dissertation aims to identify and quantify the challenges associated with operation of load-followers in the current grid with high renewable penetration under climate change impacts and,

more importantly, to recommend the optimal grid dispatch strategy that can significantly improve grid operation. The use of the NGCC technology may have to come to an end or may require renewable fuels, such as hydrogen produced from renewable sources, for accomplishing 100% renewable goals for the electricity sector. Regardless, the analysis of this technology as a load-following option contributes to establishing a framework for operation of the future electric grid in which power generation systems using hydrogen such as hydrogen turbines and fuel cells that can replace the fossil-fueled NGCC technology. Furthermore, the analysis will be extended to operation of the load-followers under grid mix scenarios when the climate change is expected to impact availabilities and dynamics of intermittent renewables. By simultaneously accounting for power plant fleet and grid dynamics within various grid mix scenarios, this work will demonstrate the enhanced significance of load-following plants for maintaining grid reliability while pursing progressive environmental targets for the state of California.

Moreover, this dissertation aims to compare SOFC-GT technology with NGCC technology as a load-following option in California grid with high renewable penetration under climate change impacts. Integration of a solid-oxide fuel cell and gas turbine provides more operational synergies than technical difficulties to overcome. Integrating two systems with different operating principles (fuel cell-electrochemistry and turbine-combustion) may cause potential control difficulties in management of flows, heat, and power. When designed and controlled properly, technical synergies coming from 1) gas turbine using unutilized fuel from fuel cell; 2) elimination of parasitic blower loads to cool the fuel cell; 3) pressurization of the fuel cell to favor forward reaction in the fuel cell result in significant efficiency boost. The discussion of SOFC-GT hybrid technology will continue with developing a decentralized control strategy enabling significant load-following and transient operation while maintaining physical constraints on fuel cell thermal

gradients and turbine surge margin. This dissertation will conclude with analyzing methods to better utilize the existing technology and discussing potential of the new systems with high efficiency, ultra-low emissions, and load-following capability in the given circumstances.

2. Goal and Objectives

The goal of this dissertation is to specify the physical behavior, performance characteristics, operational limitations, and grid-wide dispatch of current and future load-following (LF) plants in high renewable penetration grids. The following objectives are set to achieve all aspects of this goal.

1. Conduct a thorough literature review on relevant topics.
2. Develop physical models of the relevant power plants capable of simulating system characteristics upon transient demand loads.
    i. Identify and develop physical models of the relevant power plant technologies in appropriate scale maximizing technological advantage of each plant type.
    ii. Modify and utilize performance maps to simulate off-design performance of the current LF plants.
    iii. Specify system characteristics of the future LF plants for their off-design operation.
3. Assess various system designs and control strategies of the current and future LF plants for improved performance.
    i. Perform fleet-wide analysis with the current LF plant model to determine and improve parameters of interest.
    ii. Estimate system efficiency of the future LF plants in different configurations with an established steady-state calculation tool.
    iii. Develop simple control schemes for the future LF plants with P-I and feed-forward controllers that have >80% turndown and black start capabilities.

4. Optimize dispatch of these power plants in the electric grid with high renewable penetration and determine climate change impacts on fleet and grid operation.
    i. Characterize grid infrastructure, power generation mix and climate change impacts in the region of interest.
    ii. Quantify fleet performance to optimize dispatch of the LFs within grid.
    iii. Analyze potential climate change impacts on dynamics and operation of the grid.

3. Background

Consequences of changes in climate have already appeared in many forms, ranging from global warming to desertification and water maldistribution. The change in climate is also posed to increase the frequency and severity of extreme weather phenomena [10]. The meteorological phenomenon in Asia, called the Yellow Dust Storm, is an epitome of such. While yellow dust storms are not totally new to the region, the occurrence of these phenomena has been intensified by recently accelerated desertification [10]. In the Zabol region of Iran, the total damage costs, which include costs for damages to the community health, due to the intensified and prolonged dust storms during 2000-2004 were approximated to be $1213.976 million USD [11]. Still restricted to specific parts of the world, the damages can potentially increase drastically if adequate steps are not taken because human activities have only accelerated the change in global climate and environment [2]. Not only to prevent further damage from anthropogenic emissions, but also to support the rapid-growing population in these regions, development and adoption of a new utility grid network system with high use of renewable power generation is highly recommended.

3.1 Advancement of Intermittent Renewable Power Generation

The research on distributed renewable energy conversion systems has been focused on 1) lowering cost of electricity generated by different renewable power generation technologies and 2) finding the methods to guarantee efficiency and reliability of the technologies that can potentially replace existing infrastructures for cleaner energy. Not only have stand-alone systems been studied for more efficient operation of each renewable technology, but also various renewable technologies

along with proper energy storage have been explored in combinations to enhance advantages and to complement disadvantages of the various technologies [12]. According to the International Renewable Energy Agency (IRENA), renewable electricity costs have decreased significantly because of improvements in technologies, economies of scale, supply chain competitiveness, and developer experience [13]. Figure 1 demonstrates recent trends in cost of electricity generated by different solar and wind power technologies.

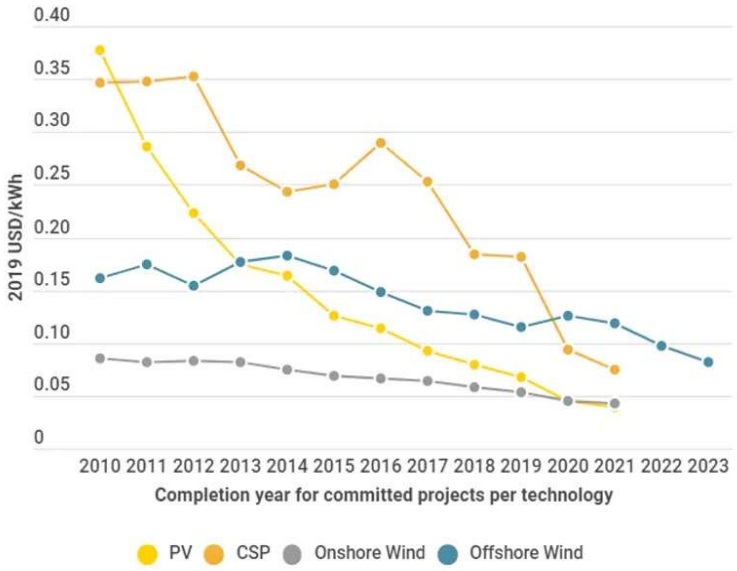

FIGURE 1: TRENDS IN ELECTRICITY COST FOR DIFFERENT SOLAR AND WIND POWER TECHNOLOGIES [13]

In 2019, costs of solar photovoltaics (PV) and concentrated solar power (CSP) have declined respectively by 82% and 47% in reference to year 2010 [13]. The solar PV panels are predicted to supply 27% of the nation's electricity by 2050, resulting in approximately a 10% decrease in greenhouse gas and air pollutants emissions, a 4% decrease in water withdrawals and a 9% decrease in consumption [14], [15]. When all the benefits are converted into monetary values, solar power is expected to provide benefits of approximately $250 billion in the climate sector and $167 billion in air quality and public health sector benefits [14]. On top of a greater market share of PV

technology for distributed energy resources (DER) applications, more attention has been given to the solar technology in utility-scale applications for PV, concentrating photovoltaic (CPV) and CSP technology [16], [17], [18], [19], [20]. The utility-scale solar refers to large-scale facilities utilizing the abovementioned technologies that sell solar-generated electricity directly to utilities or other buyers [19]. Just like with wind turbines, PV and CSP technologies have been jointly investigated with various types of storage and dispatchable generators to counteract their disadvantages coming from the dynamics and diurnal cycle of solar availability. Molina et al. have proposed a three-phase grid-connected PV system and a control algorithm incorporating a maximum power point tracker; they proved the effectiveness of the system and controller by experimentally verifying them in 250kW scale [21]. McTique et al. have proposed to retrofit an existing geothermal power plant with CSP and liquid thermal storage to improve cost effectiveness and operational flexibility [22]. Zhu et al. have optimized the electrical and thermal energy storage for the building energy system resulting in 11.26% reduction in the total annualized cost and 71.26% shift of the peak load compared to the building energy system without any energy storage [23]. In addition to integrating various complementing technologies to boost up the system efficiency, technological advancements ranging from tracking to increase in inverter loading ratio (ILR) have allowed installation of the solar technologies in less solar-favorable sites such as non-Southwestern states of the United States [19], [20].

The wind power technologies have become economically and technologically competitive with traditional means of power generation. According to Figure 1, the costs of electricity generated by onshore and offshore wind power technologies have dropped by 39% and 29% to $0.053/kWh and $0.115/kWh respectively primarily because of costs reduction associated with installment, operation, and maintenance of wind turbines as well as boosts in their capacity factors . Though

wind power has become more competitive, the irregularity in wind availability often requires other power generation means or more importantly long-term energy storage technologies for reliable operation. Gonzalez et al. have optimized the sizing of a hybrid renewable energy system integrating photovoltaics and wind power systems that could save up to 40% of present cost structure relying on the electrical grid [24]. Sun et al. have proposed an operational strategy based on the hybrid system consisting of pumped hydro storage, wind and solar that could decrease the total revenue loss by 30% due to payment for grid regulating services [25]. Wind turbines when integrated with hydrogen infrastructures such as fuel cells, electrolyzers, and compressed hydrogen storage systems have been very effective in accommodating the fuel needs for fuel cell vehicles and power needs for microgrids. Maton et al. have proposed and proved that the system consisting of wind turbines, electrolyzers and salt caverns storing hydrogen is able to produce electric power and accommodate up to 14,000 fuel cell vehicles with hydrogen fuel [26]. Valverde-Isorna et al. have presented a wind-hydrogen energy system and successfully simulated the office building dynamics with an error less than 2% in average [27].

3.2 Impacts of Climate Change on Renewable Resources

Renewable power generation solely depends on availabilities of the renewable resources. These availabilities are directly associated with geography and climate phenomena that often require sophisticated computational tool to predict. Prăvălie et al. have assessed global solar potentials using global horizontal irradiance (GHI) and direct normal irradiance (DNI) to investigate the status quo and to identify solar development opportunities [28]. Niblick et al. have assessed energy production potentials of brownfields, closed landfills, and abandoned mine lands in the United

States; soybeans, when sunflowers, and microalgae are considered for biodiesel and solar and wind for electricity, the energy produced would satisfy up to 39% of the total U.S. demand for diesel and electricity [29]. In addition to the question of where the renewable resources are located, predicting the climate phenomena becomes more significant to answer the question of when the renewable resources are going to be available to maintain grid reliability as the grid renewable penetration increases. Feng et al. have characterized and quantified the forecastability of wind series at more than 126,000 sites in the U.S. using machine learning framework and the Weather Research and Forecasting model [30]. In their series of works, He et al. have investigated wind and solar availability in China at high spatial and temporal resolution using GIS and capacity factor simulation model [31], [32].

Climate change has made it more difficult to predict climate phenomena and spatial and temporal availabilities of renewable resources. For example, exacerbation of desertification and water maldistribution may affect water availability at locations of hydro power generation units and eventually the grid operation in the future as Tarroja et al. have analyzed [33], [34]. The water maldistribution may affect solar power generation capabilities by changing cloud formation and rainfall of semi-dry or arid regions where previous analysis has approved of solar installations. Even though simply increasing the grid renewable penetration will not resolve issues that the grid operators are facing in efforts to decarbonize their grids and the climate change impacts will only make it harder for the operators to achieve their goal, grid operation strategies have to be modified to accomplish political and policy targets.

3.3 Significance of Complementary Technologies

For reliable and effective integration of the renewable technologies to meet stringent RPS targets, the significance of complementing technologies in grid operation has greatly increased [7]. These complementing technologies include different types of energy storage to various types of dispatchable generators such as hydropower and geothermal power as well as fossil fuel-based power generation from gas turbines, steam turbines and fuel cells [35]. For the energy storage, the primary challenges are to determine appropriate type, capacity, control scheme and locations to properly shift peak demands while, for the dispatchable renewable generators, primary challenges include local resource availability in terms of climate and geography [23], [36].

One promising option is to operate load-following plants more dynamically and then to transform their operation to a renewable fuel such as biogas or renewable hydrogen. In the state of California and many places around the world, the natural gas combined cycle (NGCC) plants currently provide most of the electric energy and are dynamically dispatched to enable integration of the non-dispatchable renewable resources [37]. As these renewable sources are increasingly prioritized over fossil fueled generation, however, the NGCC plants are to be operated even more dynamically in the utility grid networks for grid reliability [38], [39]. To do so, the operation and control of the NGCC power plants during transient and more highly dynamic operation modes should be analyzed and advanced.

Different modes of the NGCC power plants' transient and dynamic operation such as start-ups, load-following, and cyclic operation are assessed techno-economically and physically. Brouwer et al. have analyzed operation of the power plants in several low-carbon scenarios: they concluded that the low-carbon scenarios require approximately 50% increases in start-ups and operational variability; under current market design, all the scenarios are viable to pay back only 84% of the total generation costs per MWh [39]. Beiron et al. have analyzed the three types of flexibilities

(operational, product and thermal flexibilities) in terms of their relative impacts on operation and plant revenue to assess the economic viability of cogeneration combined cycle power plants [40]. Yu et al. have proposed an improved combined heat and power economic dispatch (CHPED) model incorporating an additional constraint of demands' feasibility requirements; the improved CHPED model demonstrated enhanced economic performance and operational reliability and security of plants [41]. Keatley et al. have developed a model that can forecast lifetime hot, warm, and cold per-start costs for a baseload power generation unit within high wind-penetration scenarios that relate fatigue-life consumption and damage accumulation during cyclic operation [42].

In addition to the economic consequences, the physical consequences of the transient and highly dynamic operation have been analyzed. Various dynamic models have been developed and compared to better understand the plants' physical responses to the transient demands [43], [44], [45], [46], [47], [48]. Operating the power plants in highly dynamic and transient manners make the systems vulnerable compromise in system electrical efficiency. In the wake of rising dynamic requirements with more renewables being integrated into electric grids, efforts to compensate for efficiency compromised from highly dynamic operation are made in various ways. Novel control strategies have been explored compared to find an optimal control for flexible operation. Haji et al. have applied adaptive model predictive control (AMPC) for the speed and temperature control of the gas turbine in the combined cycle power plant [49]. Rua et al. have compared linear and nonlinear model predictive control of the combined cycle power plant with stress monitoring; they concluded that while the linear controller demonstrates superior computational performance, non-linear controller is more applicable to start-ups and shut-downs where large stresses arise owing to large temperature gradients [50]. Novel optimization mechanisms have been developed to

optimize the NGCC plant for different purposes for further optimization studies. Huang et al. proposed a novel system integrating water desalination system with a Rankine cycle-based combined heat and power plant and demonstrated that water consumption objective optimization of the new system can reduce freshwater consumption by 54.8% while duel objective optimization can reduce fuel and water consumption by 1.7% and 21.0% respectively [51]. Furthermore, not only has the plant design been optimized for efficiency boost in both full-load and part-load operation modes but also the plant components (gas turbine, HRSG, and steam turbine) and their operation during transient have been studied extensively [52], [53], [54], [55], [56], [57], [58], [59], [60], [61], [62].

The highly transient and dynamic operation of LF power plants could result in further physical consequences. Neshumayey et al. have semi-empirically concluded that the increase in fuel consumption during ramping up and subsequent stabilization was higher than the decrease in the fuel consumption during the ramping down resulting in 2-4% increase in fuel consumption rate during the full 100%-50%-100% cycle and 0.12% increase in the consumption rate during the 100-75-100% cycle [63]. Rossi et al. have developed a simple and reliable model capable of evaluating stress on turbine rotor with less than 5% error which can be used to optimize start-up process in terms of a trade-off between start-up time reduction and damage on steam turbine rotor due to stress [64].

As grids are being decarbonized, stationary fuel cells can displace NGCCs and can be dispatched with relatively high efficiency. Because the fuel cells are only renewable when operating on renewable fuels, the fuel cell systems can contribute to a seamless transition from fossil fuels to renewable sources. In addition, the fuel cells demonstrate higher part-load efficiencies compared to the gas turbines. The gas turbines demonstrate dramatic efficiency decreases in lower part-load

conditions as power generation in the gas turbines is driven by temperature gradient; however, power generation in the fuel cells is driven by electrochemical reactions [65]. While the electrochemical reaction rates are temperature dependent, the temperature gradient is not the sole driver of the fuel cells' power generation [65]. Despite these advantages that the stand-alone fuel cell systems have, a rapid transient load-following capability has been historically indicated as their weakness. By integrating with gas turbines, fuel cells can not only achieve ultra-high efficiency but also improve its capability to respond to the rapid transients with proper control schemes [9], [66], [67]. Specifically, this fuel cell-gas turbine hybrid technology has achieved 74.4% fuel-to-electricity efficiency with molten carbonate fuel cells and >75% fuel-to-electricity efficiency with solid oxide fuel cells [9], [66]. However, this integration poses various control challenges which will be discussed in Section 3.5.

3.4 Design and Optimization of SOFC-GT Hybrids

Numerous studies have thermodynamically analyzed hybrid fuel cell gas turbine system feasibility. These thermodynamic studies analyze systems with a wide variety of design configurations, employed technologies, and nominal capacities [68], [69], [70], [71], [72], [73], [74], [75], [76], [77], [78], [79], [80], [81].While varying in many aspects, the SOFC-GT hybrid technology has demonstrated the ultra-high efficiency, ultra-low emissions and fuel flexibility required to achieve seamless transition from fossil fuels to renewable energy sources.

Still, commercialization of the hybrid technology requires considerable improvements in components and system. On a system level, the SOFC-GT hybrid systems are likely to undergo thermal management issues, mostly originated from difference in desired system operating

temperature between SOFC and GT. Specifically, SOFCs operate between 800 and 1000 K while gas turbines have a wide range of operating temperature depending on their types and capacities [65]. Radial machines, usually smaller in nominal capacity (sub-MW), require turbine inlet temperature (TIT) between 900 and 1100 K while axial machines, much larger in their nominal capacities (10-100 MW scale), operate at TIT as high as 1400 K. On a component level, the hybrid systems are likely to experience pressure and flow management issues. The design pressure ratio of gas turbines ranges from 3 to approximately 30 and their operation points are determined by characteristic performance maps, specific to each gas turbine system, dictating a combination of a flow rate and pressure ratio for each operation point [82], [83]. On the other hand, pressurizing SOFCs above atmospheric pressure increases their efficiency at the expense of additional development and capital cost. However, a significant performance improvement is noticed as the cells are pressurized. Raising the pressure from 1.4 bar to 3 bar has resulted in a 23% increase in power density while raising it from 1.4 bar to 7 bar has resulted in a 32% increase in power density in previous studies [82], [83]. Along with thermal, flow and pressure management issues, high costs involved in the hybrid system have casted doubt upon the feasibility of the SOFC hybrids [84]. However, some of the industry leaders have made significant progress. Siemens Westinghouse has demonstrated the world's first SOFC-MGT hybrid system at University of California, Irvine's National Fuel Cell Research Center from 1999 to 2003. Fuel Cell Energy has demonstrated a molten carbonate fuel cell-gas turbine hybrid system in 2004. General Electric has re-entered the business with its SOFC hybrid for power generation and propulsion technologies in 2014. Mitsubishi Heavy Industries has begun its SOFC-MGT model demonstration at Senju Techno Station in September 2016 and achieved demonstration of the same product with cumulative operating time of 10,000 hours in Kyushu University Ito Campus in October 2016.

Fuel Cell Energy has been continuing its efforts to commercialize the fuel cell-gas turbine hybrid system with solid-oxide fuel cell technology under Advanced Research Projects Agency-Energy (ARPA-E) funding from 2017.

3.5 Control and Response of SOFC-GT Hybrids

The potential future applications of the SOFC-GT hybrid technology in a highly renewable electric grid require rapid transient load-following capability. This capability has been known to be a weakness of high temperature fuel cell systems because such transient load-following could result in excessive local hot spots or spatial thermal gradients, which may impact the thermo-mechanical stability, and ultimately the system lifetime and performance [85], [86]. The optimal controller design has to focus on: 1) maximizing system transient capability; 2) minimizing risk of cell degradation. To accomplish these two contradicting goals, the decentralized control scheme is chosen over centralized control scheme for the hybrid system controller. The means by which hybrid systems load-follow and maintain operating systems vary. Kandepu et al. manipulates current to control SOFC power output and air blow off valve position at the compressor outlet to control the fuel cell temperature [87]. Chen et al. compares impacts of having and not having anode inlet temperature control during the 10% load change in two different anode recycle configurations [88], [89]. Ferrari introduces a compressor/turbine bypass valve to account for the difference between the small mechanical inertia of a microturbine and high thermal capacitance of the fuel cell; at the same time, the valve position is maintained a small Fractional Opening (FO = 0.05) to control the shaft rotational speed during load increase [90]. Using their hybrid performance (Hyper) facility, researchers in the National Energy Technology Laboratory (NETL) have been

analyzing and developing controls for a pressurized SOFC-GT hybrid system. Zhou et al. evaluates impacts of cathode mass flow rate modulation on the hybrid system performance using Hyper facility; they control the cathode mass flow rate with turbine speed and bypass valve controls [91]. Emami et al. have further investigated the impacts of the cathode mass flow rate modulation and determined ranges of PID coefficients to ensure to increase the reliability and robustness of the hybrid system [92]. Compared to the previous NETL studies focusing on the faster system response, Zaccaria et al. reinforce the importance of controlling the cell temperature gradient and voltage to offset and reduce the effect of fuel cell degradation [93]. To enhance dynamic response capabilities, Mueller et al. manipulates current to control the combustor temperature utilizing the fuel cell thermal capacitance and ability to vary the fuel reaction rate while employing the gas turbine inertia to buffer the fuel cell as it is ramping [94]. McLarty et al. has developed a decentralized control scheme with cascade P-I controllers with feed-forward focusing on greater dynamic response and achieved a 4:1 turndown ratio [9].

3.6 Summary

Hybridizing fuel cell and gas turbine technology will be a step forward to 100% renewable grid with its ultra-high efficiency, ultra-low-emission, and dispatchable power generation capability. Many hybrid designs have been thermodynamically analyzed and their proof-of-concepts have been experimentally tested. However, no prior analysis has examined the hybrid's full potentials as the dispatchable power generation unit in a grid. The dynamic dispatchability will only become more significant as the grids have higher renewable penetration and become more vulnerable to intermittency of the renewable availabilities exacerbated by climate change. This dissertation is

dedicated to delineating the physical behaviors, performance characteristics, constraints, and real-grid application of SOFC/GT technology by employing proven physical modeling methods, developing appropriate control schemes, but more importantly to exploring their full potentials as future load-following plants within associated grids under operation and climate scenarios that the plants are likely to encounter.

4. Approach

In this work, I have sought to design, control, and study load-following power plants of the present and future by employing detailed physical dynamic models. I have attempted to verify the designed models with the real-world data of the relevant components. This dissertation begins with model development and verification, continues to a system design and control study, and concludes with a macro-system analysis employing the results from the system modeling. A series of objectives are set to achieve the dissertation goal and each objective has its own tasks to be accomplished.

4.1 Task 1: Literature Review

Task 1 is established to address the first dissertation objective to conduct a thorough literature review on relevant topics. To achieve the goal of this dissertation requires an interdisciplinary approach ranging from climatology, renewable energy, and to thermodynamics and control study. Because of the wide range of disciplines, extensive yet focused literature review on various relevant subjects is indispensable. The literature review begins with search for interconnection between climate change and availabilities of renewable energy sources, leading to need for review of advancements on intermittent renewable power generation technologies and for review of complementing technologies to better integrate these renewable sources into electric grids. Among many existing and potential complementing technologies, natural gas combined-cycle (NGCC) and solid oxide fuel cell- gas turbine (SOFC-GT) hybrid technologies will be explored as current and future load-following plants in electric grids. Therefore, the literature review continues with search for publications relevant to development of physical models and controllers associated with the two technologies for more dynamic operation.

4.2 Task 2: Model Development

Task 2 is to develop physical models of the relevant power plants capable of simulating system characteristics upon transient demand loads. Chapters #1 and #2 will introduce the modeling techniques employed at National Fuel Cell Research Center (NFCRC) to simulate the physical dynamics of various components required for systems employing turbines and SOFCs; the components include power generation components such as turbomachinery and SOFC themselves as well as subsidiary components such as heat exchangers, mixing volumes and reformers. Chapter #1 is dedicated to delineating the turbomachinery modeling techniques while Chapter #2 is to delineating the modeling techniques of SOFCs and the subsidiary parts required to operate SOFC system. Due to interconnected nature of components in a SOFC-GT system, the interactions among the components can be complex and dependent on each component's dynamic response; even a small perturbation in one system component could lead into larger fluctuations in other components. Successful physical models should be able to accurately and efficiently capture physical transients of the hybrid systems occurring at the electrochemical, mechanical, and bulk thermal time scales.

4.3 Task 3: Evaluation of System Designs and Control Strategies

Task 3 is to evaluate various system designs and control strategies of the current and future LF plants for improved performance. Chapter #3 will introduce limitations regarding operation of the current LF plants within a utility grid of high renewable penetration and evaluate different fleet control strategies to resolve the limitations. As more power is generated from intermittent

renewable sources for the grid, the LF plants have to be operated more dynamically to complement the renewable sources. The dynamic operation of the conventional LF units will have consequences such as need for extended part-load operation and subsequently compromised efficiency. Chapter #3 will target these negative consequences of the dynamic operation with different fleet control strategies. Chapter #4 will examine different layouts of a 100-kW scale and 10-100 MW scale SOFC-GT hybrid systems. Particular attention is paid to selection of commercial turbomachinery for optimal integration with state-of-the-art solid-oxide fuel cell. Chapter #5 outlines the development of simple decentralized control schemes composed of PID controllers and look-up tables that are capable of load-following and simulating transients such as start-ups. The integration of SOFC and radial/axial turbomachinery has previously demonstrated both synergies and challenges. Chapter #6 will continue with evaluation of the synergies in the various layouts with discussion about differences in bypass locations and control schemes and their contributions increasing the system transient capability. Chapter #6 will also discuss the challenges from the integration and how these challenges can be resolved with different control schemes. The differences in speed control of radial vs. axial turbomachinery and in bypass locations will be discussed in the context.

4.4 Task 4: Dispatch Optimization

Task 4 is to optimize dispatch of these power plants in grid with high renewable penetration and determine climate change impacts on fleet and grid operation. Chapter #7 will discuss the optimal dispatch strategy of the LF plants within a grid with high renewable penetration. To do so, Chapter #7 will begin with generating grid and fleet operation scenarios. The hourly grid mix profiles for 365 days-period with varying grid renewable penetration values are to be generated using the

Holistic Grid Resource Integration and Deployment (HiGRID) tool [82]. While generating the fleet operation scenarios with the grid profiles, physical constraints of the current and future LF plants such as number of the LF plants in a grid and lower operational limit of the plants will be considered. The optimization criterion to determine the dispatch strategy will be based on grid-wide emissions, which will take account of operational greenhouse gas emissions of the LF plants as well as the emission penalties of the plants' transient and dynamic operation. Chapter #8 will complete the discussion with the optimal dispatch strategy in the grid with high renewable penetration by incorporating climate change impacts on availabilities of non-dispatchable and intermittent renewable resources. For the non-dispatchable renewable resources, solar and wind energy will be considered. Predicting natural phenomena that contribute to solar and wind power generation such as solar radiation and wind speed requires a computationally intensive tool such as Variable-Resolution Community Earth System-Model (VR-CESM). For scope of this dissertation, VR-CESM outputs will be used to incorporate climate change impacts on the intermittent renewable availabilities and how the changes in the availabilities impact the individual plants and associated grid operation.

5. Dynamic Modeling of Gas Turbine Systems and Components

The gas turbine model used in this work has been adapted from a gas turbine model previously developed in the Advanced Power and Energy Program (APEP) at UC Irvine. The model is intended to simulate Solar Turbine's Titan 130, a 14,250-kW single-shaft axial flow gas turbine system installed in the UC Irvine central plant. For the utility scale model, the Titan 130 gas turbine model is modified to simulate the Ansaldo AE94.3A 340-MW gas turbine that is named Moncalieri 2nd GT system, located in Moncalieri, Italy. The normalized compressor map, used for UC Irvine system, has been tuned to simulate a 340 MW class F turbine system operation. The specifications of these GT systems are presented in Table 1.

TABLE 1: COMPARISON OF PLANT SPECIFICATIONS BETWEEN UCI CENTRAL PLANT AND MONCALIERI 2GT PLANT

Specification	UC Irvine	Utility
Configuration	1 GT x 1 ST	1 GT x 1 ST
Capacity	19.1 MW	395 MW
GT output	13.5 MW	270 MW
ST output	5.6 MW	125 MW
GT mass flow	50.55 kg/s	660 kg/s
ST configuration	Single Press.	3PRH*
ST inlet temp.	225 °C	542/542/225 °C
ST inlet pressure	15 bar	94/28/4.6 bar

* Three-Pressures with Reheat

5.1 Compressor and Turbine

The gas turbine system model incorporates thermodynamic principles pertaining and dynamics of its rotating parts by using compressor and turbine performance maps, mass, momentum, and energy conservation equations as well as an interpolation strategy to determine efficiencies. Shaft speed, pressure ratio, and flow rate are normalized using the following Equation 1, Equation 2, and Equation 3. With the normalized values, the compressor and turbine maps have been scaled to a new pressure ratio using Equation 4:

$$N_{RPM} = \frac{RPM}{RPM_{des}} \sqrt{\frac{T_{in}}{T_{des}}} \quad \text{Equation 1}$$

$$N_{Flow} = \frac{Flow}{Flow_{des}} \frac{P_{des}}{P_{in}} \sqrt{\frac{T_{in}}{T_{des}}} \quad \text{Equation 2}$$

$$N_{PR} = \frac{P_{out}}{P_{in} PR_{des}} \quad \text{Equation 3}$$

$$PR_{new} = 1 + (PR_{des} - 1) \frac{PR_{orig} - 1}{PR_{des,orig} - 1} \quad \text{Equation 4}$$

Where N represents normalized values, P pressure T temperature, and PR pressure ratio. The subscripts, $in, out, des,$ and $orig$, represent inlet, out, design and original respectively. The compressor model takes inlet temperature, pressure, species concentrations, shaft speed, and an exhaust pressure as inputs. The flow rate into the compressor is determined from the empirical correlations using turbine speed, pressure ratio, and temperature. Then, using the look-up tables built based on the normalized speed, flow rate and pressure, the compression efficiency is determined. Subsequently, the pressure ratio and compression efficiency are used to determine the compressor work applied by the shaft as in Equation 5. Incorporating the compression work,

convective and radiative heat transfer within control volumes, the energy conservation principle is applied as shown in Equation 6 and Equation 7:

$$\dot{W}_C = \dot{n}_{out} \frac{h_{isen} - h_{in}}{\eta_C} \quad \text{Equation 5}$$

$$\dot{n} C_V \frac{dT_{fluid}}{dt} = \dot{W}_C + \dot{E}_{in} - \dot{E}_{out} + \dot{Q}_{conv} \quad \text{Equation 6}$$

$$\dot{m} C_P \frac{dT_{solid}}{dt} = \dot{Q}_{conv} + \dot{Q}_{rad} \quad \text{Equation 7}$$

where $\dot{W}_C$ is compressor work, $\dot{n}$ and $\dot{m}$ are molar and mass flow rates, η_C is compressor efficiency, h_{isen} is isentropic enthalpy, h_{in} is enthalpy at inlet, C_P and C_V are heat capacities, $\dot{E}_{in}$ and $\dot{E}_{out}$ are energy coming in and out of a control volume, and $\dot{Q}_{conv}$ and $\dot{Q}_{rad}$ are convective and radiative heat transfer rate.

The turbine model takes inlet temperature, species concentrations, flow rate, and exhaust pressure as inputs. As shown in Equation 8, the pressure immediately upstream of the first turbine stage is determined using a mass balance of the incoming and exhaust flow rates within a control volume while the exhaust flow rate is determined using the scaled performance map. The expansion efficiency and pressure ratio, as in Equation 9, determine the amount of work extracted from the fluid and transmitted through the shaft to the entire system. Subsequently, the turbine work and heat transfer between the solid turbine components and the working fluid completes the energy balance equations that are used to determine the solid metal and fluid exhaust temperatures in Equation 10 and Equation 11:

$$V \frac{dP}{dt} = (\dot{n}_{in} - \dot{n}_{out}) R_u T_{in} \quad \text{Equation 8}$$

$$\dot{W}_T = \dot{E}_{in} - \dot{n}_{out}(h_{in} - \eta_T(h_{isen} - h_{in})) \quad \text{Equation 9}$$

$$\dot{n}C_V \frac{dT_{fluid}}{dt} = \dot{W}_T + \dot{E}_{in} - \dot{E}_{out} + \dot{Q}_{conv} \quad \text{Equation 10}$$

$$\dot{m}C_P \frac{dT_{solid}}{dt} = \dot{Q}_{conv} + \dot{Q}_{rad} \quad \text{Equation 11}$$

where V is volume, P is pressure, $\dot{n}$ and $\dot{m}$ are molar and mass flow rate, R_u is universal gas constant, T_{in} is inlet temperature, $\dot{W}_T$ is turbine work, η_T is turbine efficiency, h_{isen} is isentropic enthalpy, h_{in} is enthalpy at inlet, $C_V$and C_P are heat capacities, $\dot{E}_{in}$ and $\dot{E}_{out}$ are energy coming in and out of a control volume, and $\dot{Q}_{conv}$ and $\dot{Q}_{rad}$ are convective and radiative heat transfer rate.

Axial and radial turbomachinery operates on single or multiple concentric shafts to eliminate gearings, mechanical losses, and failure. This constrains the single-shaft compressor and turbine sets to the same shaft speed which is either synchronous, operating at multiples of 60 Hz (50 Hz in Europe), or asynchronous. To account for the shaft dynamics, the shaft model in this study employs simple torque balance with rotational inertia in Equation 12 and Equation 13:

$$\frac{d\omega}{dt} = \frac{\dot{W}_T - \dot{W}_C - \dot{W}_{Gen}}{\omega I_o} \quad \text{Equation 12}$$

$$I_o = \frac{\rho L \pi r^4}{2} \quad \text{Equation 13}$$

where ω is shaft speed in radian, $\dot{W}_T$ is turbine work, $\dot{W}_C$ is compressor work, $\dot{W}_{Gen}$ is power generated by the shaft, I_o is rotational inertia, ρ L, and r are density, length and radius of the shaft. If the calculated mass flow rate from the turbine exceeds that of the compressor, the pressure decreases until equilibrium is reached. Similarly, if the mass flow rate exiting the compressor exceeds that exiting the turbine, the upstream pressure will increase until the turbine exhaust mass flow matches its inlet. On rare occasions, this pressure increase can cause the compressor blades to stall, leading to a stall/surge event.

5.2 Heat Recovery Steam Generator

In terms of modeling, because an HRSG typically includes liquid water heating followed by water evaporation followed by superheating steam, what might seem like a simple heat exchange problem is turned into a series of moving boundary problems that cannot be easily solved mathematically. For the scope of this study, the problem is simplified into a series of simple boundary value problems by making the following assumptions [59], [60]:

1) Water at the economizer outlet is at its saturated liquid state.
2) Phase change from liquid to gas (boiling) only takes place within the evaporator.
3) Because of relatively slow thermal response of pipe metals compared to exhaust gas flow speed, inertia of the gas is neglected.
4) Convection is the only mode of heat transfer from gas to water/steam.
5) Because the heat transfer coefficient of the water side is much higher than that of the gas side, the evaporator pipe metal temperature is assumed to be equal to the temperature of water/steam mixture, the saturation temperature.
6) Fluid properties are considered constant.

With these assumptions, the energy conservation principle inside control volumes along the length of the pipe is modeled with heat exchange within HRSG pipes as in Equation 14 and Equation 15:

$$\dot{E}_{pipe} = \dot{E}_{g,in} - \dot{E}_{g,out} + \dot{E}_{w,in} - \dot{E}_{w,out} \qquad \text{Equation 14}$$

$$\frac{dE_{pipe}}{dt} = M_m C_m \frac{dT_m}{dt} \qquad \text{Equation 15}$$

where $\dot{E}_g$ is heat transfer rate from gas, $\dot{E}_w$ is heat transfer rate from water, $\dot{E}_{pipe}$ is heat transfer rate to pipes, M_m is mass of the pipe metal, C_m is heat capacity of the pipe metal, T_m is temperature of the pipe. For modeling the superheater, the energy balance is rewritten in terms of temperatures, mass flow rates, heat capacities, heat transfer coefficients and areas to solve for three unknown temperatures, $T_{g_{out}}$, $T_{w_{out}}$, and T_m. The gas side equations are shown in Equation 16 and Equation 17 while the water side equations are shown in Equation 18 and Equation 19:

$$\dot{E}_{g,in} - \dot{E}_{g,out} = \dot{m}_g c_{p_g}\left(T_{g_{in}} - T_{g_{out}}\right) \quad \text{Equation 16}$$

$$= h_g A_{outer}(\overline{T_g} - T_m) \quad \text{Equation 17}$$

$$\dot{E}_{w,in} - \dot{E}_{w,out} = \dot{m}_w c_{p_w}\left(T_{w_{out}} - T_{w_{in}}\right) \quad \text{Equation 18}$$

$$= h_w A_{Inner}(T_m - \overline{T_w}) \quad \text{Equation 19}$$

The heat transfer coefficient of the water side is calculated using the Dittus-Boelter equation, an explicit function to calculate Nusselt number for forced convection in a turbulent pipe flow as shown in Equation 20 [95]:

$$Nu_D = \frac{hk}{D} = 0.023 Re_D^{\frac{4}{5}} Pr^{0.4} \quad \text{Equation 20}$$

where h is heat transfer coefficient, k is conductivity, D is diameter of a pipe, Re_D is Reynolds number for pipe flow, Pr is Prandtl number. While Prandtl number for water/steam is an off-the-table constant, Reynolds number of the steam/water flow inside pipes is represented differently when a mass flow rate is known instead of fluid velocity as shown in Equation 21:

$$Re_D = \frac{\rho V D}{\mu} = \frac{4\dot{m}}{\pi D \mu} \quad \text{Equation 21}$$

where ρ, is density, V is fluid velocity, D is diameter of the pipe, μ is dynamic viscosity of the fluid, ṁ is mass flow rate. While the heat transfer rate on the water side is obtained for fluid flow

inside a circular pipe, the heat transfer rate on the gas side is for fluid flow across banks of tubes [95]. Thus, the gas side heat transfer coefficient is obtained with Zukauskas correlation shown in Equation 22 [95].

$$\overline{Nu}_D = C\ Re_{D,max}^{m} Pr^{0.36} \left(\frac{Pr}{Pr_s}\right)^{1/4} \quad \text{Equation 22}$$

where $Re_{D,\max}$ is Reynolds number based on the max fluid velocity, V_{max}, Pr is Prandtl number, Pr_s is Prandtl number of the pipe. Depending on a tube arrangement and Reynolds number, the constants, *C* and *m*, may vary. The staggered tube arrangement is considered for all parts of the HRSG. With Equation 14 through Equation 19, three sets of equations are solved iteratively each time step to obtain pipe metal temperature as well as gas and water exit temperatures.

For modeling the evaporator section of the HRSG, a slightly modified energy balance equation as well as mass balance of steam generated, and water supplied are applied to the steam-water mixture. They are as shown in Equation 23 through Equation 28:

$$\dot{E}_{pipe} + \dot{E}_{st/w} = \dot{E}_{g,in} - \dot{E}_{g,out} + \dot{E}_{w,in} - \dot{E}_{st,out} \quad \text{Equation 23}$$

$$\frac{dM_{st/w}}{dt} = \dot{m}_w - \dot{m}_{st} \quad \text{Equation 24}$$

$$\frac{dE_{pipe}}{dt} = M_m C_m \frac{dT_m}{dt} \quad \text{Equation 25}$$

$$\frac{dE_{st/w}}{dt} = \frac{d(M_{st}u_{st})}{dt} + \frac{d(M_w u_w)}{dt} \quad \text{Equation 26}$$

$$\dot{E}_{st,out} - \dot{E}_{w,in} = \dot{m}_{st}h_{st} - \dot{m}_w h_{wt} \quad \text{Equation 27}$$

$$M_{st/w} = M_w + M_{st} \quad \text{Equation 28}$$

where $\dot{E}$ is change in energy, $\dot{m}$ is mass flow rate, $M$is mass, C is heat capacity, u is internal energy, and h is enthalpy. The subscripts pipe, st, w, g, and m respectively represent pipe, steam, water, gas and metal. The above-mentioned assumptions make modeling the evaporator and economizer much easier than modeling the superheater. The assumptions 1) and 5) pre-determine steam conditions at the economizer outlet; therefore, there is no need to model the economizer operation. Furthermore, the assumptions 2) and 5) simplify that the evaporator metal temperature matches the saturation temperature as in Equation 29:

$$T_m = T_{sat} \qquad \text{Equation 29}$$

where $T_m$is metal temperature and T_{sat} is saturation temperature. After applying the assumptions, the water side equation can be expressed simply as the enthalpy difference between saturated steam and liquid water as in Equation 27. With the economizer outlet conditions on the water side known, the energy required to convert liquid water into steam at a specific temperature and pressure is determined. Since the gas side equations used for determining $\Delta\dot{E}_g$, stays the same as in the superheater case, the unknown temperature at the evaporator outlet on the gas side can be calculated with Equation 16 and Equation 17.

At the same time, change in fluid pressure within the HRSG is dealt with separately from the exchanges of heat energy. For the scope of this study, because controlling the pressure at the inlet of the steam turbine is of the significance, estimating the pressure drop of water and steam within HRSG tubes is important. Although there are many factors that can affect the pressure of fluid flow inside the tubes, friction is the major contributing factor to the pressure drop. The contribution of friction to the pressure drop is determined by the varying fluid properties in Equation 30 and Moody friction factor, f, a dimensionless parameter defined in Equation 31 and Equation 32 for different flow conditions [95]:

$$\frac{dp}{dx} = -f\frac{\rho u_m^2}{2D} \quad \text{Equation 30}$$

$$f = \frac{64}{Re_D} \quad \text{Equation 31}$$

$$\frac{1}{\sqrt{f}} = 1.14 - 2\log_{10}\left(\frac{e}{D} + \frac{9.35}{Re_D\sqrt{f}}\right) \quad \text{Equation 32}$$

where p is pressure, x is length, D is diameter of the pipe, ρ is density, u_m is average fluid velocity in the pipe, $Re_D$is Reynolds number in respect to the diameter of the pipe, e is relative roughness. Using the given flow conditions and pipe design parameters, dimensionless parameters such as the Reynolds number and relative roughness are calculated to characterize the fluid flow inside the pipes. If the pipe flow is laminar, the friction factor is simply calculated withEquation 31. If turbulent, the friction factor is iteratively calculated due to the implicitness of Colebrook-White equation as in Equation 32. The calculated friction factors eventually allow back-calculation of the change in pressure along the length of the pipes in the HRSG.

5.3 Steam Turbine

The main governing equation for turbine operation is Stodola's ellipse equation, shown in Equation 33, where it dictates off-design calculations when the turbine nozzles are not choked [96]. Representing the off-design turbine operation points, the elliptical path is dictated by the equation below. There are two versions of the equation; however, for scope of this study, the temperature version of the equation is employed as follows:

$$\emptyset = \frac{\dot{m}\sqrt{T}}{P} = K\sqrt{1 - \left(\frac{B}{P}\right)^2} \quad \text{Equation 33}$$

where $\emptyset$ is a dimensionless number that is calculated depending upon the structural design of a turbine system such as number of stages within a turbine and number of turbines within a system, $\dot{m}$ is the mass flow rate into the turbine system, T is the turbine inlet temperature, P is the turbine inlet pressure, K is the Stodola constant, and B is turbine outlet pressure. The number of stages within a turbine comes into effect only when the number of stages is limited to a few. Setting the mass flow coefficient and Stodola constant, calculated by the design parameters, constant allows back-calculation of the corresponding inlet or outlet pressure when all other parameters such as outlet or inlet pressure, inlet temperature and mass flow rate are known. With the back pressure and temperature of each turbine known, the steam specific enthalpy and entropy at the outlet can be obtained from steam tables; with the obtained entropy and calculated inlet pressure, the steam enthalpy at the inlet can be obtained, again from the table. Assuming a quasi-steady equilibrium condition along with the obtained inlet and outlet steam conditions, the following mass and energy conservation equations for the control volume, drawn around a turbine, can be solved as shown in Equation 34 through Equation 38:

$$V\frac{d\rho}{dt} = \dot{m}_{in} - \dot{m}_{out} \quad \text{Equation 34}$$

$$V\frac{d(\rho e)}{dt} = \dot{E}_{in} - \dot{E}_{out} - \dot{W}_s - \dot{E}_{gen} \quad \text{Equation 35}$$

$$\dot{E}_{gen} = \dot{E}_{in} - \dot{E}_{out} \quad \text{Equation 36}$$

$$= \dot{m}_{st}\varepsilon_{isen}(h_{in} - h_{out}) \quad \text{Equation 37}$$

$$\dot{W}_s = \dot{E}_{in} - \dot{E}_{out} - \dot{E}_{gen} = \omega I_o \frac{d\omega}{dt} \quad \text{Equation 38}$$

where $\dot{m}_{in,out}$ is the mass flow rate at inlet and outlet of the control volume, $\dot{E}_{in,out}$ is the energy coming in and out of the control volume, $\dot{W}_s$ is the work by the shaft, $\dot{E}_{gen}$ is the power generated, I_o is the shaft rotational inertia, ω is the speed of the shaft. The quasi-steady assumption, for each time step, sets the mass flow rate at turbine inlet and outlet equal to each other. For steady-state operation, there is no need to exert any power to change the speed of the shaft; that is the rate of change of shaft power, $\dot{W}_s$, for any given timestep is negligible. Therefore, $\dot{E}_{gen}$ can be simplified as in Equation 36. However, for transient operation in which power demand to the model is different from one time step to another, the energy balance within the control volume is achieved with $\dot{E}_{gen}$ that is determined by a controller, and with the $\dot{W}_s$ that involves the shaft rotational inertia and change in shaft speed.

6. Dynamic Modeling of SOFC and System Components

For the electricity sector, grid decarbonization is the key to counteract climate change impacts. With increasing renewable penetration, fossil fuel power plants with proven flexibility and durability can be dynamically operated to supply demand loads and to maintain grid reliability for the time being [35]. However, the fossil fuel power plants need to be replaced with renewable infrastructures that are dynamically dispatchable as the grids are decarbonized. For their fuel flexibility ranging from fossil-fuels to renewable fuels and dynamic dispatchability, high temperature fuel cell systems can seamlessly replace the fossil fuel power plants in the grids [65]. Furthermore, these advantages of the high temperature fuel cells allow integration of turbomachinery for improved efficiency and dynamic capability [65]. The system integration and dynamic operation of the integrated system requires accurately predicting the system and component behaviors as well as detailed understanding of physical phenomena within the system under a variety of possible operation scenarios. Chapter 6 discusses modeling techniques to predict and comprehend the behaviors of components that are commonly used in SOFC systems. For components involving high operating temperature and chemical reactions, detailed spatial discretization is required to capture local performance and thermal gradients that are largely dependent on local species concentrations, temperature, and material properties. Sections 6.1, 6.2 and 6.3 discuss how physical dynamics and performance of a heat exchanger, reformer and SOFC are respectively simulated using the spatial discretization strategy. The following sections, Sections 6.4 discusses the methods chosen to simulate the components that do not employ the same spatial discretization technique yet are essential in system operation.

6.1 Heat Exchanger

Although the heat exchangers used in the scope of this study may vary in size, they are all modeled as hot and cold flows exchanging heat through a layer of solid heat exchanger material. While the quasi-3-D simulation of the fuel cell requires discretization of the component in three directions (which will be further discussed in Section 6.3), performance simulation of the heat exchanger only requires calculating thermal gradient in 1-D if the heat exchanger is modeled as explained above. The details on how the heat exchangers are discretized into nodes are shown in Figure 2.

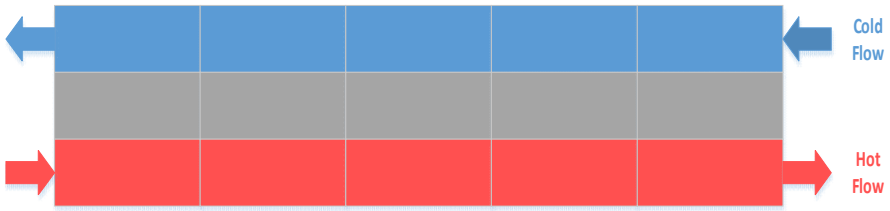

FIGURE 2: NODE DISCRETIZATION WITHIN HEAT EXCHANGER (COUNTER-FLOW)

For the scope of this study, the heat exchanger is discretized into five nodes in the flow direction each comprising the two flows and a solid that separates the flows for modeling. Heat is transferred from the hot flow to the solid and then to the cold flow through convective heat transfer; at the same time, heat is also transferred through conductive heat transfer within the solid. The convective heat transfer is modeled as shown in Equation 39 while the conductive heat transfer is modeled as in Equation 40. Using these modes of heat transfer, the dynamic conservation of energy equations are subsequently applied into each node as shown in Equation 41 and Equation 42:

$$Q_{conv} = h_c A_{surf} \left(\frac{T_{in} + T_{out}}{2} - T_{solid} \right) \quad \text{Equation 39}$$

$$Q_{cond} = kA_{surf}(T_{n+1} + T_{n-1} - 2T_{solid})/L_{node} \quad \text{Equation 40}$$

$$\frac{dT_{solid}}{dt} = \frac{Q_{conv,hot} - Q_{conv,cold} + Q_{cond}}{C_v V_{solid} \rho_{solid}} \quad \text{Equation 41}$$

$$\frac{dT_{out}}{dt} = \frac{[\dot{n}h]_{in} - [\dot{n}h]_{out} - Q_{conv}}{C_v V_{node} \rho} \quad \text{Equation 42}$$

where h_c is the convective heat transfer coefficient, A_{surf} the surface area, k the thermal conductivity, L the length, T the temperature, C_v the specific heat at constant volume, V the volume, and ρ the density. The subscripts, in, out, $solid$, and $node$, represent inlet, outlet, solid and each discretized node respectively. The conservation of energy principle is applied onto the solid nodes to calculate the solid temperature. This energy balance also accounts for thermal mass of the solid within heat exchangers. On the other hand, the same principles are applied to each flow node to calculate outlet temperature of the two flows. Different from the energy balance of the solid nodes, the energy balance of each flow node includes enthalpies associated with incoming and outgoing flows.

6.2 Pre-Reformer

The pre-reformer is a reactor volume usually located in front of the fuel cell anode to reform 10-15% of the fuel, in this case methane. The pre-reforming process involves steam methane reforming and water-gas shift reactions respectively shown in Equation 43 and Equation 44. As a whole, one mole of methane along with two moles of water results in one mole of carbon dioxide and four moles of hydrogen as in Equation 45. The chemistry calculations of the reforming reactions use the established kinetic reaction mechanisms outlined by Achenbach et al where the kinetic of the CH_4 reforming process is estimated as shown in Equation 46 [97]:

$$CH_4 + H_2O \rightarrow CO + 3H_2 \quad \text{Equation 43}$$

$$CO + H_2O \rightarrow CO_2 + H_2 \quad \text{Equation 44}$$

$$CH_4 + 2H_2O \rightarrow CO_2 + 4H_2 \quad \text{Equation 45}$$

$$\dot{r} = \left(p_{CH_4}\right)_w k_0 \left(1 - \frac{p_{CO} p_{H_2}^3}{p_{CH_4} p_{H_2O} K_p}\right) e^{\left(-\frac{E}{RT}\right)} \quad \text{Equation 46}$$

For the scope of this study, the pre-reformer is modeled as an adiabatic reformer; the discretization technique is not applied to simulate temperature gradient within a component. Because the chemistry behind the fuel reforming process in the pre-reformer is equal to that behind the internal reforming occurring within the fuel cell, the details about the reforming process are further shared in Section 6.3.

6.3 Solid Oxide Fuel Cell

For scope of this study, modeling SOFC stack involves quasi-3-D approach. The stack is discretized into five control volumes; two bipolar plates, two flow channels and positive electrode-electrolyte-negative electrode (PEN) assembly. Each control volume is divided into 5x5 nodes in which each node accounts for different physical phenomena including electrochemistry, conservation of mass, momentum, and energy along with heat and mass transfer within and between each control volume. The details on how the SOFC stack is discretized into a total of 125 control volumes are shown in Figure 3.

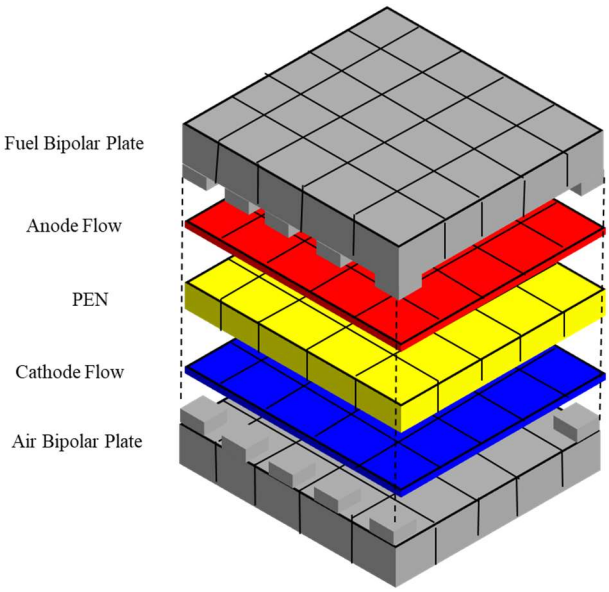

FIGURE 3: NODE DISCRETIZATION WITHIN A FUEL CELL STACK

The electrochemistry inside the fuel cell is modelled with a series of generic equations. Subtracted from the Nernst potential in Equation 47 are three types of polarization; activation polarization, ohmic polarization and concentration polarization as shown in Equation 48 through Equation 52:

$$E = E_0 + \frac{RT}{2F}\ln\left(\frac{P_{H_2} * P_{O_2}^{0.5}}{P_{H_2O}}\right) \qquad \text{Equation 47}$$

where E is the reduction potential, E_0 the standard electrode potential, R the universal gas constant, T the temperature, F the Faraday constant, P the partial pressure. The subscripts, H_2, O_2, and H_2O, represent hydrogen, oxygen and water respectively. The activation polarization is an alteration of famous Butler-Volmer equation whose transfer coefficient is set to 0.5. The ohmic polarization is modeled as a product of current density and ohmic resistance, which is modeled as thickness over conductivity. The concentration polarization of each electrode is modeled as natural log of a partial pressure ratio of relevant species:

$$\eta_{act} = \frac{RT}{\alpha nF}\ln j_0 + \frac{RT}{\alpha nF}\ln j = \frac{2RT}{nF} sinh^{-1}\frac{j}{2j_0} \qquad \text{Equation 48}$$

$$\eta_{ohm} = j * \frac{t_i T}{\sigma_{0,i} e^{-\Delta G_{act}/RT}}$$ Equation 49

$$\eta_{conc,a} = -\frac{RT}{nF}\ln\left(\frac{P_{H_2}}{P_{H_2O}}\right) = -\frac{RT}{2F}\ln\left[\frac{1-\frac{RT}{2F}\frac{jt_a}{D_{a,eff}P_{H_2,in}}}{1+\frac{RT}{2F}\frac{jt_a}{D_{a,eff}P_{H_2O,in}}}\right]$$ Equation 50

$$\eta_{conc,c} = -\frac{RT}{nF}\ln\left(\frac{P_{O_2}}{P_{O_2,in}}\right) = -\frac{RT}{4F}\ln\left[\frac{\frac{P_c}{\delta_{O_2}} - \left(\frac{P_C}{\delta_{O_2}} - P_{O_2,in}\right) * e^{\frac{RT\, j\, \delta_{O_2} t_c}{4F D_{c,eff} P_c}}}{P_{O_2,in}}\right]$$ Equation 51

$$\delta_{O_2} = \frac{D_{O_2,k(eff)}}{D_{O_2,k(eff)} + D_{O_2-N_2(eff)}}$$ Equation 52

where R is the universal gas constant, T the temperature, α the charge transfer coefficient, n the number of moles, F the Faraday constant, j_0 the limiting current density, j the current density, t the material thickness, σ_0 the electrical conductivity, G_{act} the activation energy, P the pressure/partial pressure, and D the diffusivity. The subscripts, i, H_2, H_2O, a, c, eff, k, and in, represent different materials, hydrogen, water, anode, cathode, effective, Knudsen diffusion, and inlet respectively. The hydrogen and water partial pressure ratio are substituted with effective diffusivity, material thickness and inlet pressure of species at the anode. The ratio of oxygen partial pressure and oxygen partial pressure at inlet is used to calculate cathode concentration polarization. Again, the partial pressure ratio is substituted with cathode pressure, partial pressure oxygen at the inlet, effective diffusivity, material thickness and charges at cathode.

The energy balances of solid and flow control volumes take a slightly different general form. The energy balance of the plates is sum of different modes of heat transfer in and out of the plates as in Equation 53. Compared to the energy balance for the two bipolar plates, PEN assembly energy balance incorporates heat generated form chemical reactions along with heat transfers as in

Equation 54. To calculate local convective heat transfer in and out of each node assumes two conditions: 1) fully developed flow; 2) uniform temperature within each control volume. Along with the assumptions, a Nusselt number of four, determined from standard engineering tables, is used to calculate convective heat transfer coefficient, h with hydraulic diameter, D_h, and conductivity, k of the channel as in Equation 55:

$$m_{plate}C_{plate}\frac{dT}{dt} = Q_{conv} + Q_{cond} + Q_{rad} \quad \text{Equation 53}$$

$$\rho V C_{elec}\frac{dT}{dt} = Q_{conv} + Q_{cond} + Q_{rad} + Q_{gen} \quad \text{Equation 54}$$

$$Nu_D = \frac{hD_h}{k} \quad \text{Equation 55}$$

where m is the mass, C the heat capacity, T the temperature, Q the heat transferred, ρ the density, V the volume, Nu the Nusselt number, h the convective heat transfer coefficient, D_h the hydraulic diameter, and k the thermal conductivity. The subscripts, $plate$, $conv$, $cond$, rad, $elec$, and gen, respectively represent a plate, convection, conduction, radiation, electrolyte, and generated. The energy balances of the cathode and anode channels are similar to those of the solids except that there are enthalpies related to incoming and outgoing flows. The cathode and anode flow channels are modeled as in Equation 56 and Equation 57 respectively:

$$\dot{n}_{\text{air}}\mathrm{C}_P\frac{dT}{dt} = \dot{n}_{in}h_{in} - \dot{n}_{out}h_{out} + Q_{conv} + Q_{cond} + Q_{rad} - Q_{ion} \quad \text{Equation 56}$$

$$\dot{n}_{\text{fuel}}\mathrm{C}_P\frac{dT}{dt} = \dot{n}_{in}h_{in} - \dot{n}_{out}h_{out} + Q_{conv} + Q_{cond} + Q_{rad} + Q_{ion} - P_{gen} - Q_{gen} \quad \text{Equation 57}$$

where $\dot{n}$ is the molar flow rate, C_P the specific heat at constant pressure, h the specific enthalpy, Q the heat transferred, and P the power. The subscripts, air, in, out, ion, $fuel$, and gen, respectively represent air, inlet, outlet, oxygen ion transferred, fuel and generated. For cathode, on top of incoming and outgoing enthalpies and different modes of heat transfer, there is heat

transferred out of cathode flow by oxygen ion crossing over. For anode, heat transferred out of the cathode by oxygen ion is transferred into anode flow while power and heat generated are pulled out of the fuel flow.

All the mass balance equations used in this model are solved using the general dynamic mass balance equation shown in Equation 58. The fuel flow rate at anode inlet solely depends upon the electrochemistry and utilization as shown in Equation 59. While the air flow rate at cathode inlet may be determined through electrochemistry, the air flow is responsible for cooling the stack that air flow rate should be dependent on the stack temperature:

$$\dot{n}\frac{dX_i}{dt} = \dot{n}_{in}X_{i,in} - \dot{n}_{out}X_{i,out} + R_{ref} + R_{consumed} \quad \text{Equation 58}$$

$$\dot{n}_{fuel} = \frac{I}{2U_{fuel}F\left(4X_{CH_4} + X_{CO} + X_{H_2}\right)} \quad \text{Equation 59}$$

where $\dot{n}$ is the molar flow rate, X the molar ratio of a species, R the reaction rate, I the current, and U the utilization ratio. The subscripts, i, ref, $consumed$, $fuel$, CH_4, CO, and H_2, respectively represent different species, reformed, consumed, fuel, methane, carbon monoxide, and hydrogen. On top of the incoming and outgoing species, the mass balance equations should account for reaction rates associated with internal reforming and/or electricity generation. The reforming reactions include steam-methane reforming and water-gas shift reactions as in Equation 43 and Equation 44 respectively. The chemistry calculations of the reforming reactions use the established kinetic reaction mechanisms outlined by Achenbach et al as in Equation 46. On the other hand, the electricity is generated through hydrogen and oxygen forming water in the fuel cell that the mass balance within the fuel cell should take account for consumption of oxygen and hydrogen in cathode and anode as well as the gas species participating in the reforming as in Equation 60 and Equation 61.

$$R_{reform} = f(P, T, X_{out})$$ Equation 60

$$\frac{dX_i}{dt} = \frac{R_{reform} + R_{use} + (\dot{n}X)_{in} - (\dot{n}X)_{out}}{P_i V_i / R_u \, T_i}$$ Equation 61

where $\dot{n}$ is the molar flow rate, X the molar ratio of a species, R the reaction rate, P the pressure, V the volume, R_u the universal gas constant, and T the temperature. The subscripts, $reform$, use, in, out, and i, respectively represent reformed, used, inlet, outlet and a type of species. As a whole, the SOFC stack model takes net current, two streams and outlet pressures as inputs and outputs voltage, current, power, various temperatures, two streams and inlet pressures.

6.4 Mixing Volume & Oxidizer

The mixer is simulated as a volume that mixes two or more flows into one flow. The mass balance is simply modeled as shown in Equation 62; the outlet flow rate equals all the inlet flow rates added together. As shown in Equation 63, the energy balance is simply a collection of enthalpies associated with inlet and outlet flows.

$$\dot{n}_{out} = \sum \dot{n}_{in}$$ Equation 62

$$\dot{n}_{out} C_p \frac{dT}{dt} = \sum \dot{n}_{in} h_{in} - \dot{n}_{out} h_{out}$$ Equation 63

where $\dot{n}$ is the molar flow rate, C_P the specific heat at constant pressure, T the temperature, and h the enthalpy. The subscripts, out and in, respectively represent outlet and inlet. In this SOFC-GT hybrid system, oxidizer is located after the fuel cell to oxidize remainder of the fuel. To model the oxidizer, the same mass and energy balance equations from those of the mixer (Equation 62 and Equation 63) are incorporated to calculate changes in temperature and pressure of the flow going

through this component. In addition, chemical reactions shown in Equation 64 and Equation 65 are incorporated into the model oxidizing carbon monoxide and hydrogen into carbon dioxide and water respectively.

$$CO + \frac{1}{2} O_2 \rightarrow CO_2 \qquad \text{Equation 64}$$

$$H_2 + \frac{1}{2} O_2 \rightarrow H_2O \qquad \text{Equation 65}$$

Through these combustion reactions, the temperature of the fuel cell outlet flow is raised from its operating temperature (800-1000K) to above a certain level to ensure high enough turbine inlet temperature for proper integration with the turbomachinery. For the hybrid configuration analyzed in this study, size of the second heat exchanger on air side is a factor to consider to ensure high enough turbine inlet temperature for turbomachinery operation and cathode inlet temperature for efficient fuel cell operation.

7. Analysis of SOFC-GT Hybrid System Configurations

Although various SOFC-GT hybrid configurations have been previously studied in the literature, many of these design studies have not taken highly dynamic operational scenarios that these hybrid systems are likely to encounter in real world into account when designed. For SOFC topping cycle, the system configurations from emulator facilities in Thermochemical Power Group of University of Genoa (TPG) and National Energy Technology Laboratory of U.S. Department of Energy (NETL), shown in Figure 4 and Figure 5 respectively, are representative of those that have considered dynamic operation as they have been designing the hybrid system and proven their capabilities to operate dynamically. The SOFC-GT hybrid configurations from these emulator facilities have been analyzed and compared to develop a system configuration that will synergistically improve performance of the hybrid system upon dynamic transients.

7.1 Description of HYPER facility at NETL & at TPG of University of Genoa

Each of these systems employs different methods to emulate the cathode and anode operation of fuel cells and to control the system upon dynamic demand loads. The facilities at TPG and NETL have three main bypass valves at the same locations (TPG names in parentheses): bleed valve (VB), cold air bypass valve (VC) and hot air bypass valve (VR). While the bleed valve at NETL and VB at TPG are used to bleed air out of each system after its compressor to prevent system failure from compressor surge, the two other valves direct flows to different locations on the systems. While the cold air bypass directs airflow from compressor outlet to post-combustor outlet, VC directs the pressurized air from compressor outlet to before its cathode inlet.

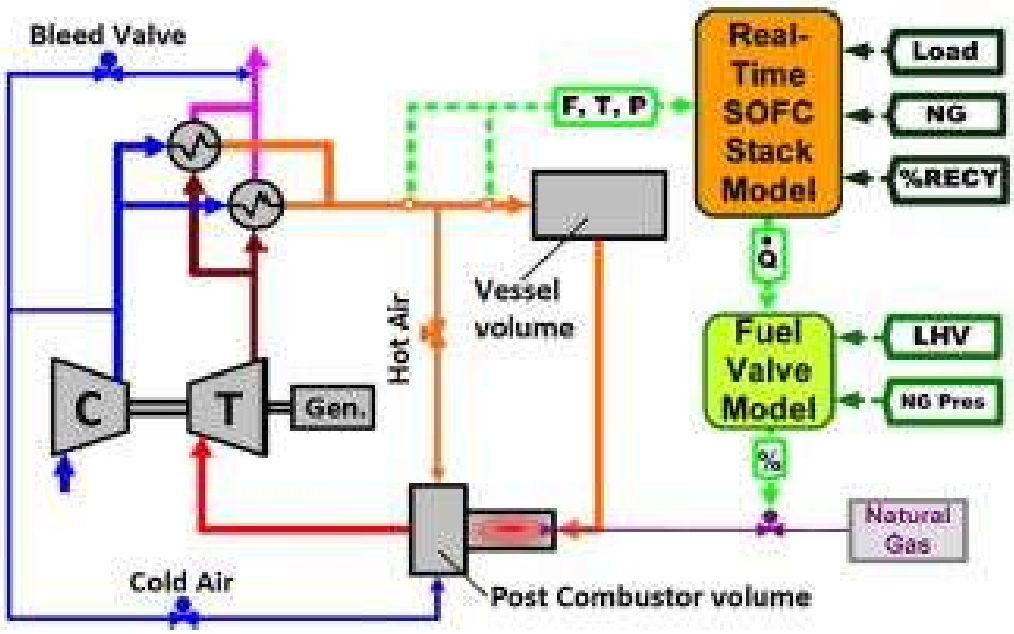

FIGURE 4: EMULATOR CONFIGURATION AT NATIONAL ENERGY TECHNOLOGY LABORATORY AT MORGANTOWN, WV [84]

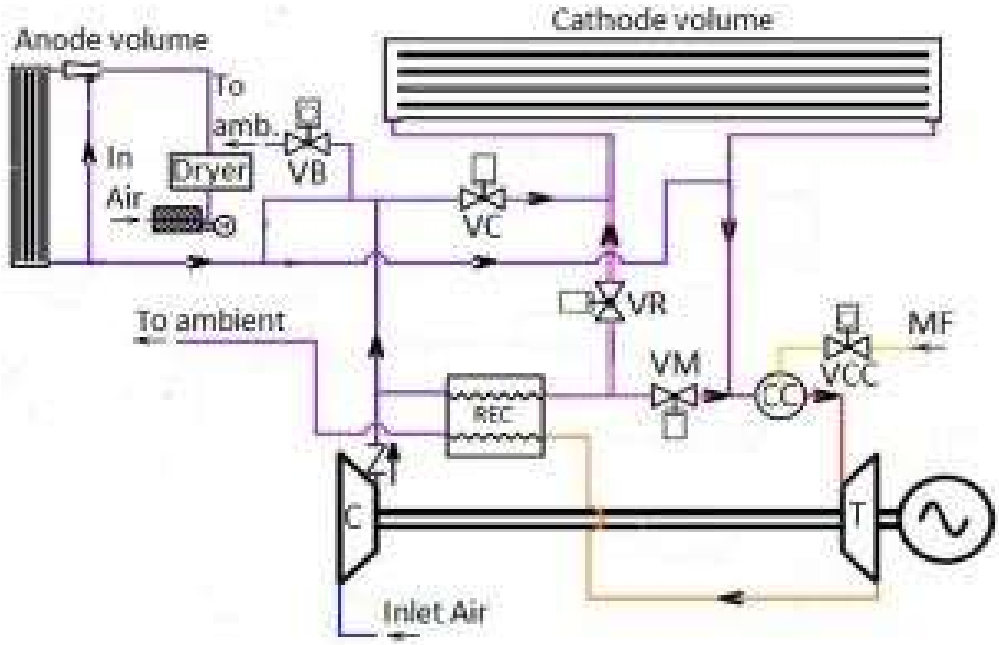

FIGURE 5: EMULATOR CONFIGURATION AT THERMOCHEMICAL POWER GROUP

AT UNIVERSITY OF GENOA [84]

The cold air bypass has an indirect impact on cathode inlet temperature by manipulating air flow rate into its recuperator. On the other hand, VC has more direct impact on cathode inlet temperature by directly mixing cold air flow with the main air flow. Both the hot air bypass valve and VR take the flows after the recuperator, but the hot air bypass directs its flow to the post-combustor outlet while VR is used to split the main air flow after the recuperator into the cathode and to the post-combustor.

7.2 Description of the Proposed SOFC-GT Hybrid System

Compared to the system configurations of the emulator facilities in NETL and TPG, the proposed configuration allows design of a more intuitive control strategy. To enable highly dynamic operation of the system, 1) the number and location of bypass valves are determined and 2) number of flows mixed at mixing points are minimized to avoid any potential complications of manipulating a manipulated variable impacting multiple control variables. Figure 6 demonstrates the proposed configuration of the SOFC-GT hybrid system for this dissertation and how the main bypass valves are used differently.

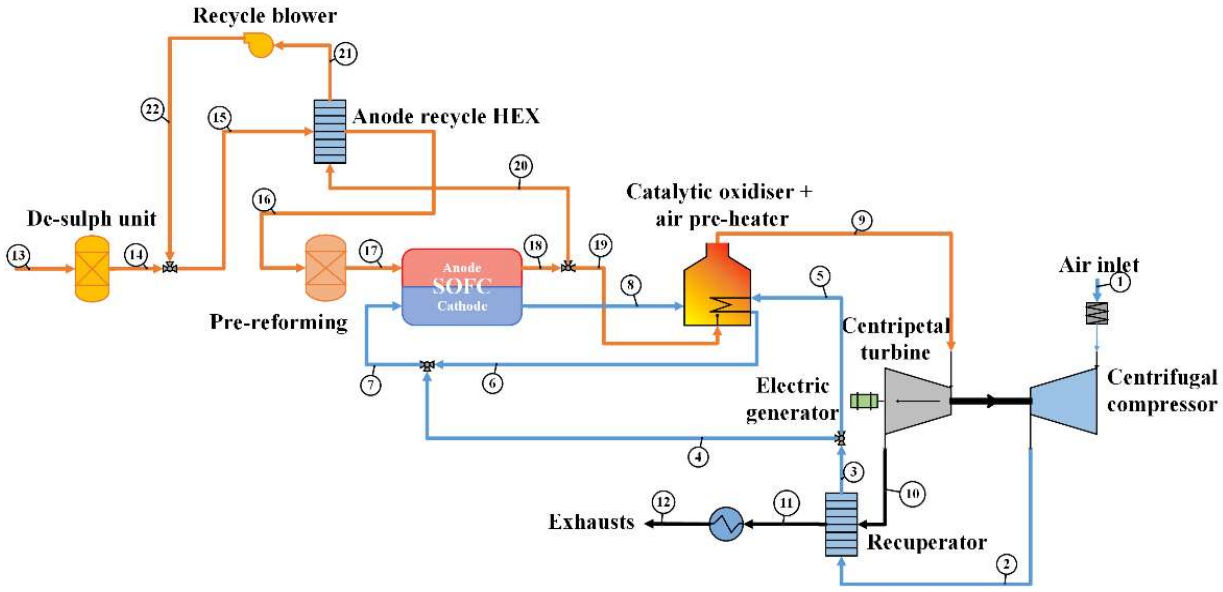

FIGURE 6: PROPOSED PLANT CONFIGURATION FOR THE SOFC-GT HYBRID POWER PLANT

For the air side, the proposed configuration only has a cold air bypass valve. This bypass valve directs the air flow from the recuperator outlet to a mixing volume in front of the cathode inlet to control the cathode inlet temperature. A bleed valve is not necessary even for a very dynamic demand load as long as the rpm and air flow rate are carefully controlled (details about the control strategy will be shared in the next section). A hot air bypass is also not included in the proposed layout because the air flow rate into the cathode can be managed for a wide range of operation with the control scheme that will be discussed in the next section. However, as the discussion leads into start-up operation of the system, one or both valves may become necessary. For example, for the start-up, a hot air bypass may have to be implemented to direct the air flow from the cathode inlet bypassing the fuel cell to the cathode outlet to allow enough air flow and time to heat up the system.

The proposed configuration has eliminated a mixing location where more than two flows are mixed (for NETL facility, the mixing point is after the post-combustor and for TPG facility, the point is before the cathode). The removal of these mixing points allows operation and control of the system

to be more intuitive and clearer. Specifically, the hot air bypass (if implemented in the proposed design) will only be used to control the cathode air flow rate without any potential complications towards the cathode inlet temperature or turbine inlet temperature. For example, at TPG facility, the cathode inlet temperature is subject to change by manipulating either VC or VR while at NETL facility, the turbine inlet temperature is subject to change by manipulating either the cold air bypass or hot air bypass valve without addition fuel supply directly into the post-combustor.

8. Development of Controller for SOFC-GT Hybrid System

8.1 Controller Schematics

To facilitate dynamic operation of the SOFC-GT hybrid system, its controller must be capable of maintaining system reliability and minimizing risk of cell degradation during the operation. Thus, the keys to the controller development are to maintain operating temperature and thermal gradient. With these goals and key points in mind, the control scheme has been developed. Compared to a stand-alone SOFC system, the SOFC-GT hybrid system offers a wider range of variables that can be either manipulated or controlled. Thus, not only have these variables been more carefully selected, but also they have to be paired up properly. Figure 7 shows the developed control scheme. While Table 2 demonstrates a list of controlled and manipulated parameters,

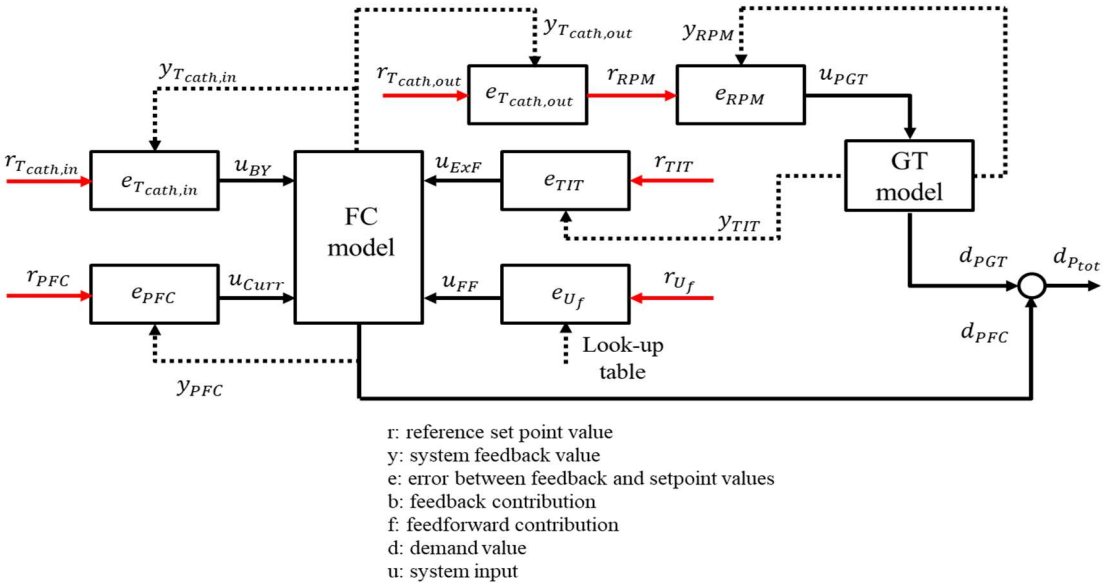

FIGURE 7: CONTROL SCHEME DEVELOPED FOR SOFC-GT HYBRID SYSTEM

TABLE 2: LIST OF CONTROLLED AND MANIPULATED PARAMETERS

	Controlled	Manipulated	Controller Type	Set point	Notes
1	$T_{cath,out}$	$RPM_{setpoint}$	Cascade Feedback	$\mathrm{T}^{0}_{\mathrm{cath,out}} + 2 * (1 - \mathrm{PR_{FC}}) * 10$ $\mathrm{T}^{0}_{\mathrm{cath,out}} = 1024.2$ K	Maintain $T_{cath,out}$
2	RPM	P_{GT}	Cascade Feedback	$RPM_{setpoint}$ set by Loop #1	
3	$T_{cath,in}$	VO	Feedback	$\mathrm{T}^{0}_{\mathrm{cath,in}} + 1 * (1 - \mathrm{PR_{FC}}) * 5$ $\mathrm{T}^{0}_{\mathrm{cath,in}} = 997.1$ K	Maintain $T_{cath,in}$
4	P_{SOFC}	$Current$	Feedback	Look-up	
5	U_{fuel}	$\dot{m}_{fuel}$	Look-up table	$\frac{Current * \#_{cells} * 0.001}{2 * F * U_{fuel} * (4 * \%_{CH_4} + \%_{CO} + \%_{H_2})}$	
6	TIT	$\dot{m}_{fuel,excess}$	Feedback	$\mathrm{TIT}^{0} - 8 * (1 - \mathrm{PR_{FC}}) * 10$ $\mathrm{TIT}^{0} = 1152$ K	Maintain TIT
7	$S2C^{*}$	$\dot{m}_{st,excess}$	Look-up table	$9 * 10^{-5} * 24^{1-\frac{PR_{FC}}{0.15}**}$	S2C > 2 <15% Load

*S2C is steam-to-carbon ratio

**PR_{FC} is a ratio of the fuel cell power output over the nominal output

The control scheme is a decentralized P-I control with feedforward, feedback loops and look-up tables. The cathode outlet temperature, cathode inlet temperature, and TIT target values are fixed via empirical linear functions of the SOFC/GT power ratio (PR), as shown in Equation 66 through Equation 69 below. The first two loops consist of a cascade loop. In the first loop, the shaft revolutions per minute (RPM) set point is manipulated to control the cathode outlet temperature. The RPM set point is determined by a feedforward and feedback. The fuel cell power target determines the feedforward as in Equation 69 and the difference between cathode outlet

temperature and its set point determines the feedback. In the following loop, gas turbine power set point is manipulated to control the shaft RPM based on the RPM set point. Because the second loop in the cascade control loop is an open loop, the actual gas turbine output is not controlled. The bypass valve opening is manipulated to control the cathode inlet temperature; the current density is manipulated to match the fuel cell power, which is fixed by the load demand. The fuel flow rate is manipulated to control the fuel utilization whose variation is dictated by Equation 70. Equation 70 calculates the fuel flow rate using the current, previously determined by the feedback control loop, number of cells ($\#_{cells}$), global fuel utilization ratio (FU), molar ratio of each relevant species ($\%_i$) in the fuel. The excess fuel flow rate is manipulated to control the TIT in order to avoid temperatures lower than 1152 K at partial load. Finally, the steam flow rate produced using process water in the heat recovery steam generation unit is manipulated to control the steam-to-carbon ratio (S2C) at the inlet of the pre-reforming reactor (stream #18), at loads lower than 15% of the nominal load.

$$T_{cath,out} = T^0_{cath,out} + 2 * (1 - PR_{FC}) * 10, T^0_{cath,out} = 999.3\ K \quad \text{Equation 66}$$

$$T_{cath,in} = T^0_{cath,in} + 1 * (1 - PR_{FC}) * 5, T^0_{cath,in} = 988.3\ K \quad \text{Equation 67}$$

$$TIT = TIT^0 - 6 * (1 - PR_{FC}) * 10, TIT^0 = 1152\ K \quad \text{Equation 68}$$

$$\mathrm{RPM} = \mathrm{RPM}^0 * (1 - 0.4 * (0.35 * (1 - \mathrm{PR_{FC}}))^{\frac{3}{4}}), \mathrm{RPM}^0 = 142800 \quad \text{Equation 69}$$

$$\dot{\mathrm{n}}_{\mathrm{fuel}} = \frac{\#_{\mathrm{cells}} * \mathrm{Current}}{2\mathrm{F} * \mathrm{FU} * (4 * \%_{\mathrm{CH_4}} + \%_{\mathrm{CO}} + \%_{\mathrm{H_2}})/1000} \quad \text{Equation 70}$$

The cathode inlet and outlet temperature targets are increased with decreasing fuel cell load to compensate for lack of heat generated within the fuel cell at lower part-load conditions. The turbine inlet temperature targets are decreased with decreasing fuel cell load to match reduction in the gas turbine power with that in the fuel cell power and, at the same time, to keep the TIT high enough for air preheating in the recuperator. Lastly, the feedforward RPM equation is determined by recalibrating the feedforward gain and coefficient of the feedforward speed control used in McLarty et al. [9].

8.2 Zero-Load and Start-up

Zero-load (i.e., controlled transient from full load to zero load ending with a stack operating at OCV at its nominal temperature) and hot start-up (i.e., controlled transient from zero load to full load starting from a hot stack run at open circuit voltage) transients are also simulated in our model and we develop a specific strategy to manage those conditions in a controlled fashion. These conditions feature the operation of the SOFC close or at the open circuit voltage (i.e., low or zero current, i.e., low or zero fuel utilization factor), and with minimum air and fuel flow rates. For this reason, lest the control strategy is changed, the following risks to the SOFC stack are possible: i) local anode fuel starvation at low currents, i.e., insufficient fuel supply to all sections of the cell, which may determine local current reversal; ii) anode electrode materials oxidation if the anode flow rate goes to zero, which may determine thermos-mechanical stresses in the cell; ii) carbon deposition due to insufficient steam in the anode recycle stream, caused by low hydrogen and methane oxidation in the anode channel at low currents; iii) uneven pressure differential between

the anode and cathode compartments; iv) temperature values outside the suggested safety ranges. Two preventive measures are implemented.

First, proper fuel flow rate control can preclude anode material oxidization. The fuel flow rate is maintained at the 15% level to ensure enough reactant concentration for safe shutdown process. Starting at the 15%, the controlled and manipulated variables of the fuel flow rate-fuel utilization control loop is flipped that now the fuel flow rate is controlled by the fuel utilization ratio. When the hybrid system is being shut-down (the fuel cell power output is decreased to below 5% of its nominal condition) with the fuel flow rate manipulated to maintain the fuel utilization ratio, the full cell stack model demonstrates negative local current density. Figure **8** and Figure **9** demonstrate current density maps for the fuel cell with and without negative local current density respectively.

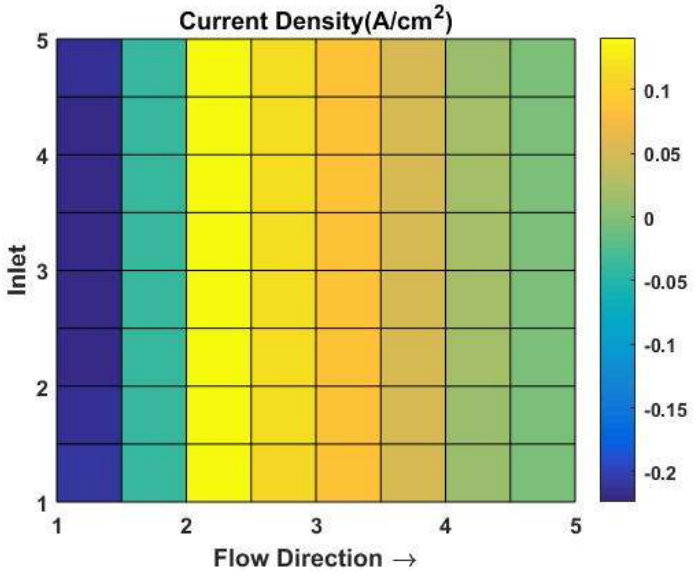

FIGURE 8: CURRENT DENSITY MAP WITH NEGATIVE LOCAL CURRENT DENSITY

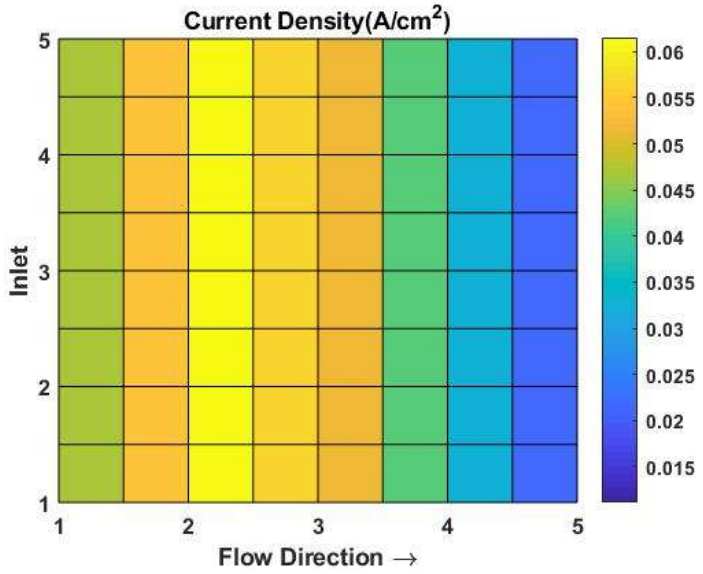

FIGURE 9: CURRENT DENSITY MAP WITHOUT NEGATIVE LOCAL CURRENT DENSITY

The negative local current density is a numerical anomoly that indicates that the reverse reaction (electrolysis) is being favored as hydrogen concentration at the anode inlet is too low. However, as the fuel utilization ratio goes down to maintain the fuel flow rate, another problem occurs in operation in the lower current density regime, which is carbon deposition.

Second, for the normal range of operation (15%-100% of the nominal condition), the steam-to-carbon ratio is maintained above 2 to prevent potential carbon deposition by manipulating anode recycle ratio. However, in the fuel cell, the electrochemical reaction responsible for generating electricity is also responsible for generating water and heat. Thus, lower current density (for below 15%) inevitably means less water and heat that even a higher recycle ratio of the anode flow does not guarantee the high enough steam-to-carbon ratio. In real-life, a low steam-to-carbon ratio incurs carbon deposition within the fuel cell potentially causing its failure. To facilitate the lower current density operation without anode material oxidization or carbo deposition, extra steam flow rate is supplied into the system. The amount of the excess steam supply is determined based on the

fuel cell power ratio ($\frac{FC\ Power}{FC\ Nominal\ Power}$). The relation between the excess steam supply rate and fuel cell power demand is as shown in Equation 71.

$$\dot{n}_{st,extra} = 5 * 10^{-6} * 24^{(1-\frac{PR_{FC}}{0.15})} \quad \text{Equation 71}$$

8.3 Load Matching Loop

In the control scheme presented in Section 8.2, the gas turbine power output is not controlled as the second loop of the cascade control loop is open at the end. Since the gas turbine output is mainly a function of turbine inlet temperature and shaft RPM, the dependent variables of the gas turbine power output are already parts of the whole control scheme, imposing a challenge of lacking a manipulative variable to control the gas turbine output. In this section, load matching loop is introduced and analyzed on how its integration maximizes system-wide load-following capability. The load matching loop is applied through balancing power generation, power consumption, energy loss and demand. Equation 72 demonstrates the power balance equation among power generated, consumed, and load requested for the default control loop. Equation 73 demonstrates the balance equation for the load matching loop, in which difference between the net power generated and load is matched by manipulating the fuel cell power set point.

$$0 = P_{FC} + P_{GT} - P_{Blower} - Load \quad \text{Equation 72}$$

$$\frac{dP_{FC,setpoint}}{dt} = P_{FC} + P_{GT} - P_{Blower} - Load \quad \text{Equation 73}$$

With the same demand to the system given, the presence of the load matching loop makes a difference in the hybrid system's load-following capability. Figure 10 compares the total power output with and without the load matching loop.

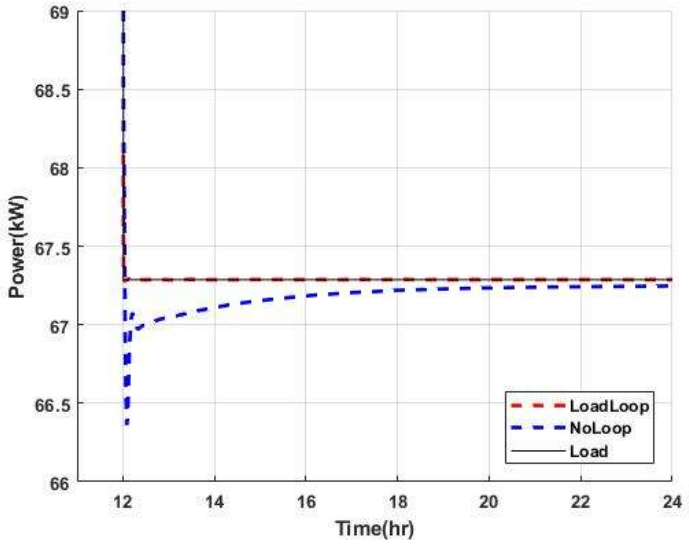

FIGURE 10: COMPARISON OF TOTAL SYSTEM POWER OUTPUT WITH AND WITHOUT LOAD MATCHING LOOP

With the load matching loop, the total power generated matches perfectly with the demand. On the other hand, without the loop, the total power generated by the system demonstrates a mismatch with the demand by up to 1.3% for 8 hours after the step change takes place. In order to fully assess the situation, the total system output is broken down into gas turbine and fuel cell power output. Figure 11 and Figure 12 respectively compares the gas turbine and fuel cell power output to their own set points with and without the load matching loop.

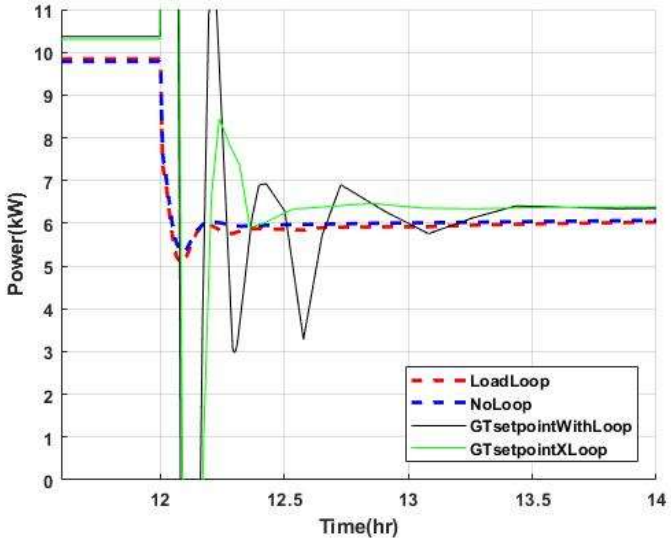

FIGURE 11: COMPARISON OF THE GAS TURBINE POWER OUTPUT WITH AND WITHOUT THE LOAD MATCHING LOOP

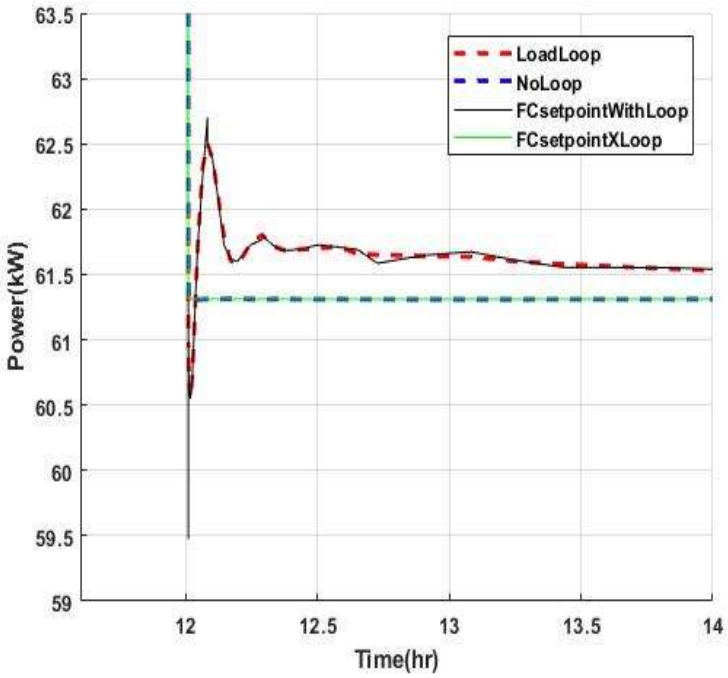

FIGURE 12: COMPARISON OF THE FUEL CELL POWER OUTPUT WITH AND WITHOUT THE LOAD MATCHING LOOP

Since the gas turbine power output is not directly controlled, the gas turbine power set point does not match the actual gas turbine power output. More importantly, the presence of the load matching loop does not cause any significant change in the gas turbine output. As shown in Figure 12, the difference between the net system power and load is going to be matched by manipulating the fuel cell power set point, thus the fuel cell power output. The fuel cell power output balances out the trough of the gas turbine power output taking place after the step change. While the implementation of the load matching loop in the controller maximizes the load-following capability of the hybrid model, this extra control loop layering the existing power control loops decreases the ramping capability by 38% from 5.33%/min to 3.33%/min.

9. Performance Improvement of NGCC technology

The natural gas combined cycle power plant is the most popular type of a power plant around the world. For last decades, it has not only been one of the major power sources but also been dynamically dispatched as a complementing technology. As integrating more renewables into grids, these conventional power generation units have to be operated even more dynamically 1) to complement non-dispatchable renewable sources such as solar and wind and 2) to maintain grid reliability. Although the NGCC power plants are capable of such flexible operation, the plants experience significant compromise in their efficiency at low part-load operating conditions. To compensate for the compromise in efficiency, an individual plant fleet can be controlled differently. For scope of this study, two other control strategies have been investigated: variable inlet guide vane (VIGV) and variable speed controls. For the VIGV control scheme, airflow into the compressor of a gas turbine system is regulated for improved performance at part-load. On the other hand, for the VS control scheme, the speed of the generator (shaft) of the gas turbine system is controlled to achieve higher efficiency performance for each of the part-load conditions. Shown in Figure 13, both VIGV and VS control schemes have demonstrated efficiency improvement for the overall NGCC system compared to the base case control scheme. Specifically, VIGV control improves performance by efficiency points ranging from 2.8% to 13.5%; while VS control improves performance from 4.1 to 28.4 efficiency points over the range of conditions explored.

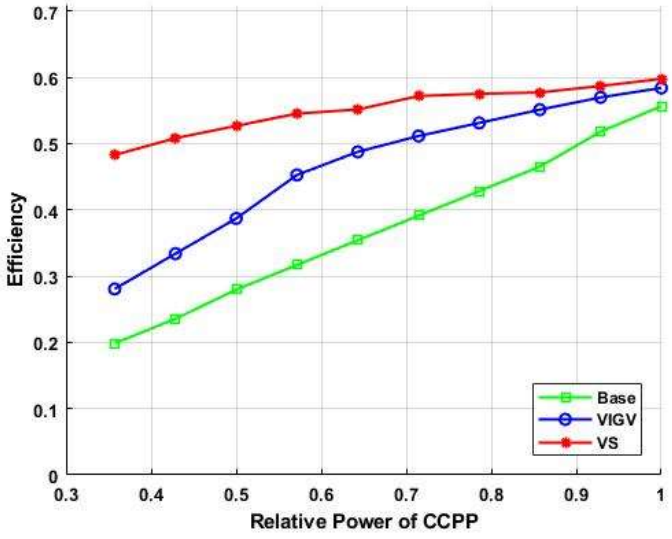

FIGURE 13: COMPARISON OF EFFICIENCY CURVES FOR THREE DIFFERENT NGCC CONTROL STRATEGIES

For gas turbine combined-cycle technology, one or two gas turbines serve as a primary power source whose exhaust heat is used to produce steam for a steam turbine. Because of the interconnectedness between these two types of power sources, changes in the control scheme of the GTs will result in changes in operating conditions of the connected downstream components such as the HRSG and ST. As shown in Figure 14, the efficiency curves of the utility-size class CCPP and its components (GT and ST) with different control schemes resemble those of the GT and ST for the same schemes.

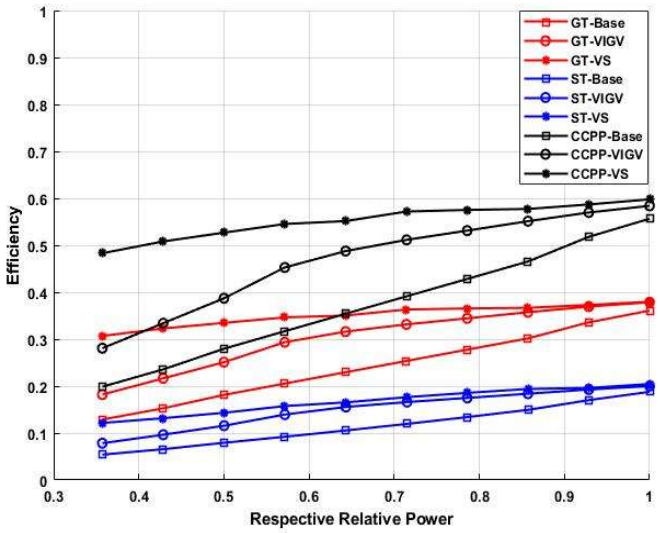

FIGURE 14: EFFICIENCY COMPARISON OF GAS AND STEAM TURBINES UNDER DIFFERENT CONTROL STRATEGIES

Although the connections among GT, HRSG and ST have allowed a boost in system efficiency, the control schemes might complicate the operation of each component of the system. Operating the combined system at part-load conditions introduces transients in airflow and turbine exhaust temperature (TET) of the gas turbine. Figures # and # show how air flow rate and TET change over the range of operation explored with the different control schemes implemented. Note that the VIGV case lowers air flow for part-load operation to keep turbine inlet temperature higher while the VS case controls the shaft speed (for a single-shaft unit, one shaft connects a compressor, turbine and generator) which changes in speed selected affect system air intake non-monotonically. Compared to these two novel control cases, the base case does not directly control mass flow or shaft speed so that the mass flow rate for the base case is constant as shown in Figure 15. On the other hand, less work is extracted in the base case as indicated by TET increases as shown in Figure 15.

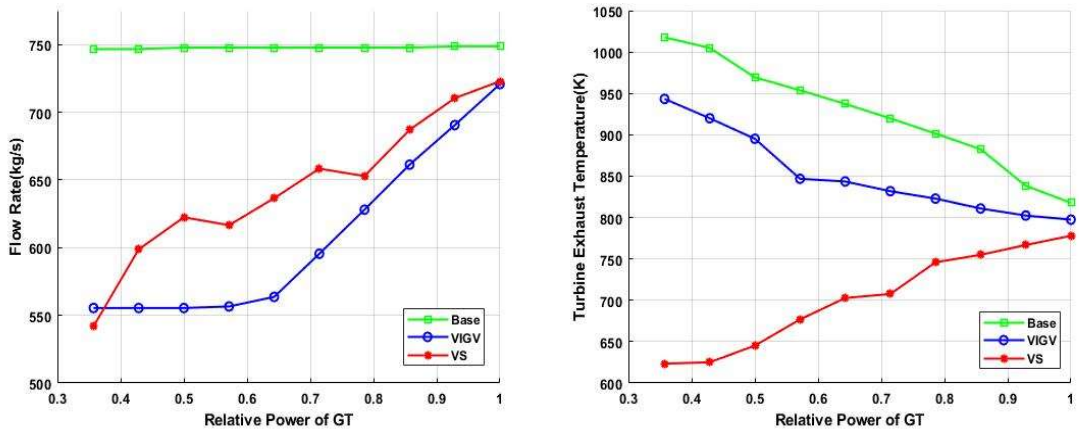

FIGURE 15: FLOW RATE AND TEMPERATURE AT TURBINE EXIT FOR DIFFERENT CONTROL STRATEGIES OVER THE RANGE OF OPERATION

Responsible for producing steam for a ST with the exhaust heat of GTs, the HRSG might suffer from complications due to transients in the amount of heat input by changes in either airflow or TET (or both) from the GT exhaust. Figure 16 demonstrates how HRSG steam flow rate changes with the relative power when the system is controlled with each of the control strategies implemented.

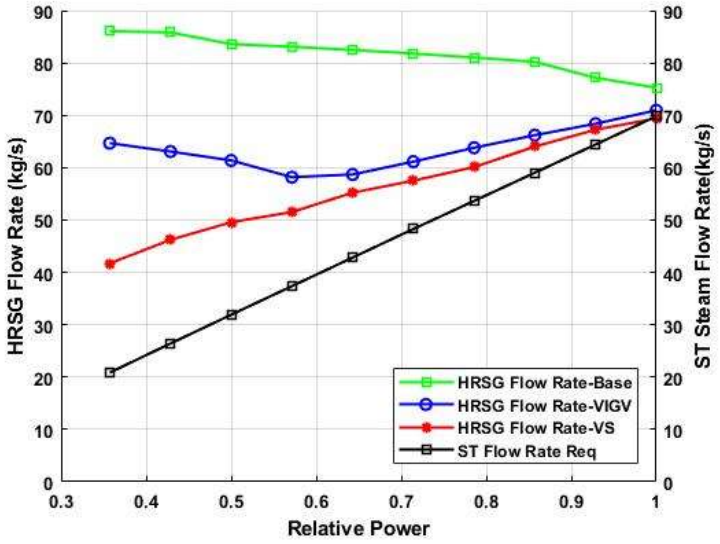

FIGURE 16: STEAM PRODUCTION CAPACITY OF HRSG WITH THE DIFFERENT CONTROLS ALONG WIH STEAM FLOW RATE REQUIREMENT

The amount of steam that the ST requires for the range of operation is directly proportional to the amount of generated power. At the same time, the HRSG suffers from slight compromises in its steam production rate with the application of VIGV and VS control schemes. However, for all the control schemes implemented, the HRSG is capable of producing more than enough steam for the ST over the range of operation because of the higher TET achieved at part load conditions in the GT exhaust. This is primarily a result of raising TIT by lowering air flow in the VGV control scheme and by lowering speed in the VS control scheme, which extracts less energy from the flow through the GT leaving TET higher.

10. Development and Application of Dispatch Models

One of the novelties of this study is at its integration of the power plant physical models to the grid dispatch model. The grid dispatch model developed in this study is capable of communicating with various tools and models, Holistic Grid Resource Integration and Deployment (HiGRID) tool [98], the NGCC models previously developed in SIMULINK/Matlab, and the SOFC-GT hybrid models developed for this dissertation in STRIDES (Matlab) [99], to apply operational dynamics and constraints of a power plant fleet on the grid mix simulation. In addition, the dispatch model can apply climate change impacts on solar and wind availabilities to adjust the renewable generation profiles using VR-CESM outputs. The following sections discuss how outputs of the different abovementioned models are used within the dispatch model to quantify grid performance in terms of emissions. Section 10.1 discusses the grid mix scenarios generated by the HiGRID tool. Section 10.2 discusses climate change impacts applied to the grid mix scenarios using VR-CESM outputs. Section 10.3 discusses how the dispatch model generates different dispatch strategies based on operational constraints of power plant fleets and the grid associated with the fleets.

10.1 Scenario Generation with the HiGRID tool

The three scenarios for future California grid have been generated with the Holistic Grid Resource Integration and Deployment (HiGRID) tool whose validity was verified with Federal Energy Regulatory Commission (FERC) data of 2000 and 2001. The specific methodology that the tool uses to produce future grid projection is presented by Eichman et al. [98]. A representative weekly prediction from the annual HiGRID results for three scenarios is presented in Figure 17, Figure 18, and Figure 19. These scenarios represent annual projections of the California grid mix comprising various types of generators. Shown in Figure 17 and Figure 18, two of the three grid

scenarios have 33% and 50% renewable penetration, respectively, as set by California's Renewable Portfolio Standards (RPS). Shown in Figure 19 is the 80% scenario, which has been analyzed as a pathway scenario relevant to the 100% renewable future. Note that the 80% RPS target can only be achieved with energy storage, which reduces the effective time-of-delivery renewable penetration to 72.5%.

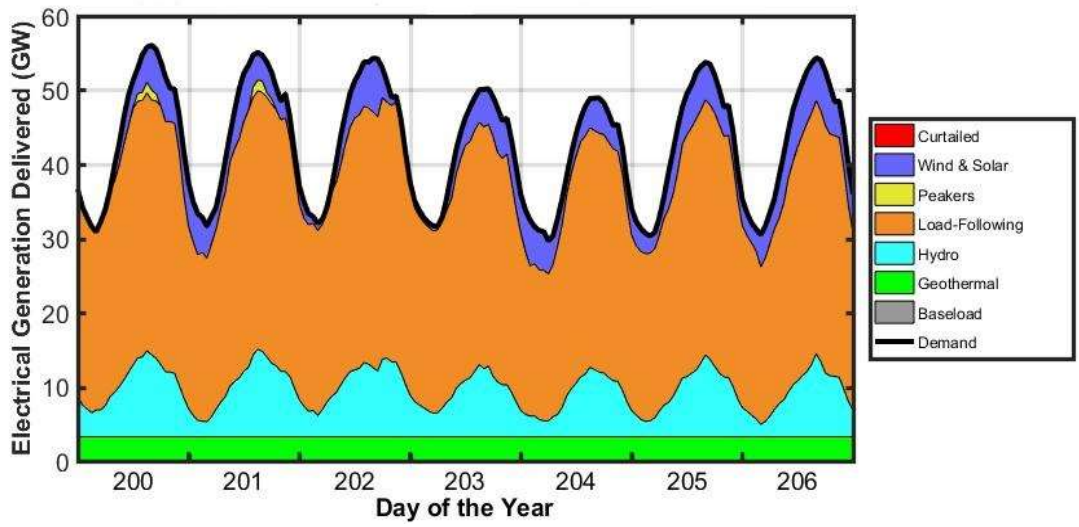

FIGURE 17: CALIFORNIA GRID SCENARIO WITH 33% RENEWABLE PENETRATION

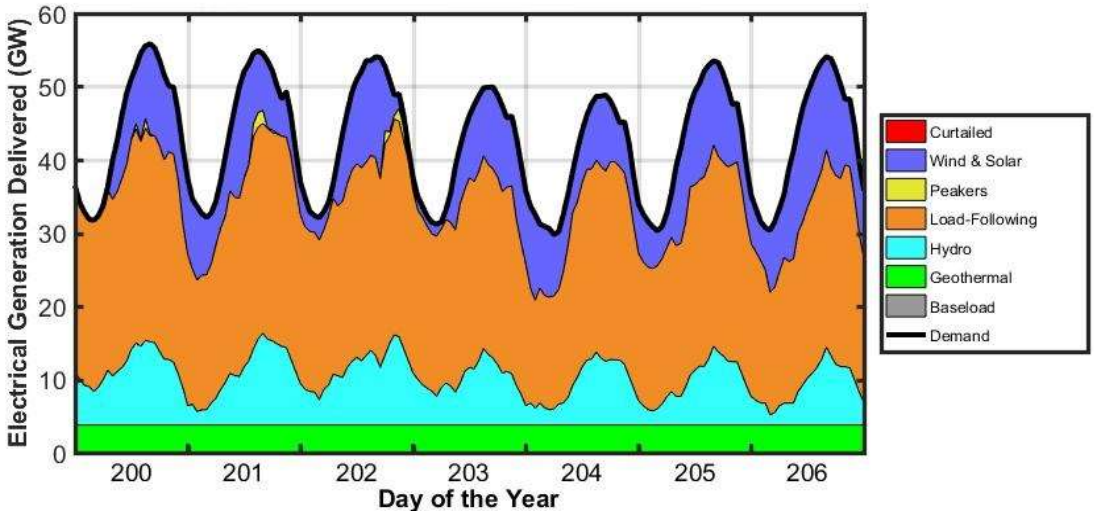

FIGURE 18: CALIFORNIA GRID SCENARIO WITH 50% RENEWABLE PENETRATION

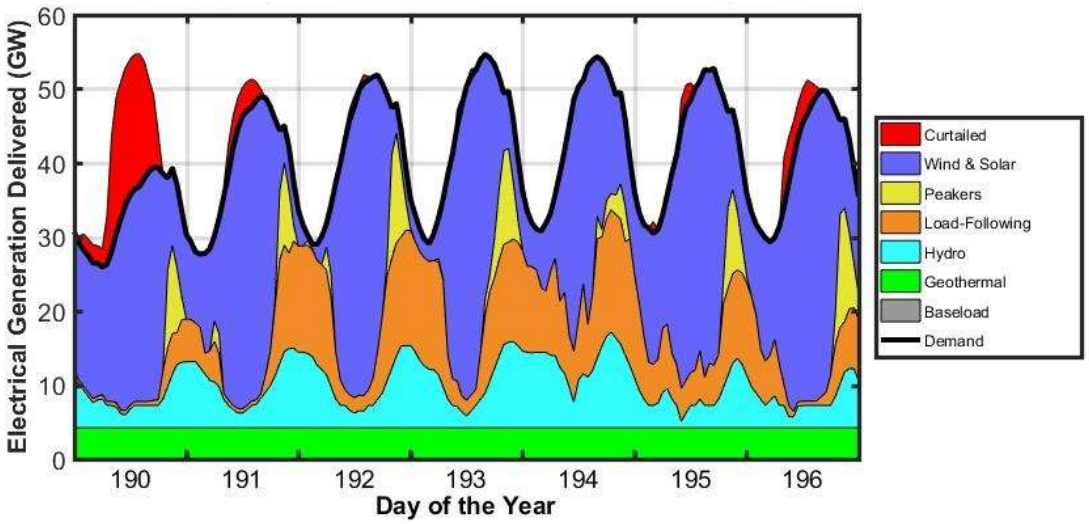

FIGURE 19: CALIFORNIA GRID SCENARIO WITH 80% RENEWABLE PENETRATION

From the three scenarios, the load follower plant dispatch profiles of the grid projections are extracted and compared in Figure 20. As expected, these three load-following profiles demonstrate a decreasing trend in average capacity factor from 0.55 to 0.42 and to 0.21 as renewable penetration is increased from 33% to 50% to 80%. Then, the extracted profiles are normalized and input into the verified physical NGCC model developed to ensure that an NGCC plant would have the physical capability to meet the dynamic dispatch required. The base case scenarios have been simulated using the physical NGCC model as shown in Figure 21. They have been generated by assuming that all the load-followers within the grid have the same nominal capacity of 395MW (the size of NGCC plant for which the physical model was verified to simulate accurately) and that they are all operating in load-following mode.

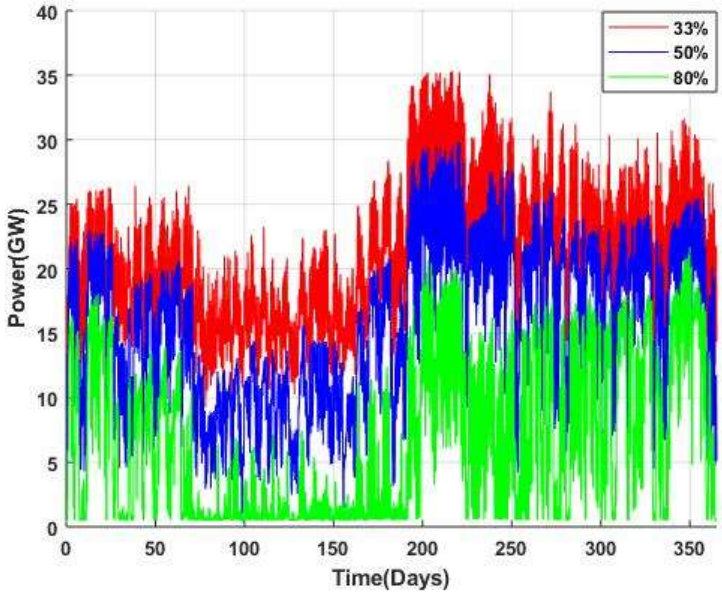

FIGURE 20: COMPARISON OF THE LOAD-FOLLOWER PROFILES EXTRACTED FROM THE THREE CALIFORNIA GRID SCENARIOS

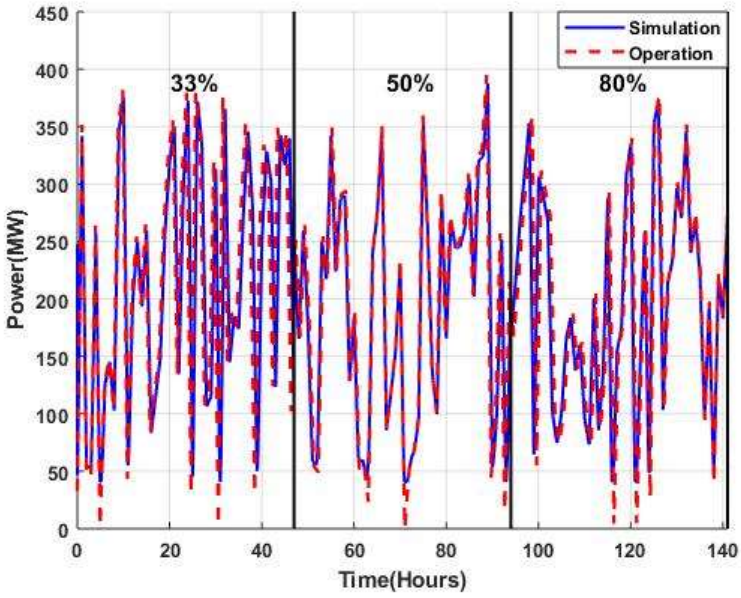

FIGURE 21: TWO DAYS OF NGCC PHYSICAL MODEL SIMULATION RESULTS FOR THE DYNAMIC DISPATCH REQUIRED OF THE THREE RENEWABLE PENETRATION SCENARIOS

Based upon these base case demand profiles, the amount of time that a power plant would be required to operate in various part-load conditions follows the decreasing trend of the average

capacity factor. Shown in Figure 22, as the grid renewable penetration increases, an individual load-follower would be required to operate at lower part-load conditions for extended periods of time. Among the 8760 hours in a year, the number of hours that a load-follower operates in either a near-full or full operating condition does not vary significantly; specifically, the percentage of hours at full or near-full capacity decreases from 8.8% to 6.5% and then to 4.2% of the total 8760 hours. This implies that even with high renewable power penetration the full capacity of current dispatchable generation may still be needed periodically. On the other hand, the percentage of hours that a load-follower might operate in the 0-20% part-load range increases from 0% to 2.4% and then to 41.7% as the renewable penetration increases from 33% to 50% and then to 80%.

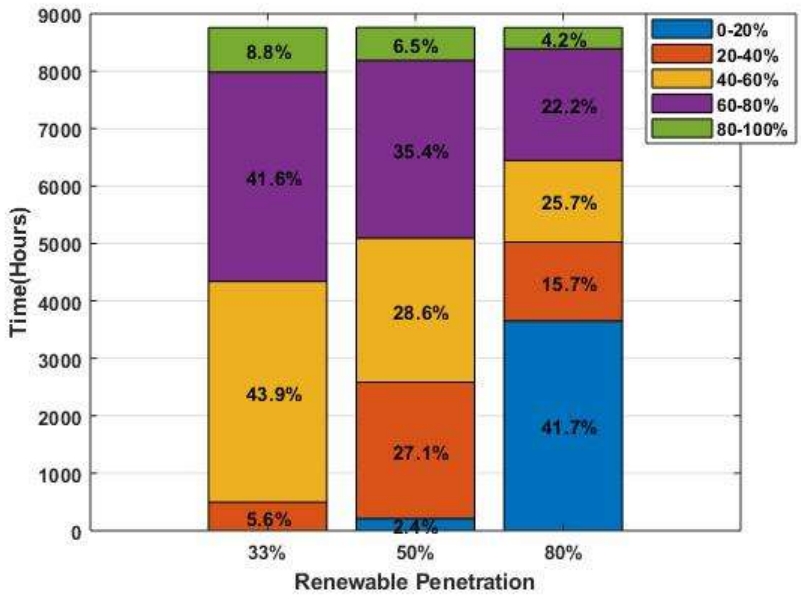

FIGURE 22: BREAKDOWN OF HOURS THAT A LOAD-FOLLOWER MIGHT OPERATE IN VARYING PART-LOAD CONDITIONS FOR THE THREE RENEWABLE PENETRATION SCENARIOS

Due to the abovementioned changes in the grid operation, we hypothesize two load-following power plant dispatch improvements that may lead to more reliable and more efficient grid operation as more non-dispatchable renewables are used in utility grid networks. First, an

improvement in part-load efficiency of the dispatchable power plant fleet (whether NGCC or fuel cell) is needed. As shown in Figure 22, because load-followers are likely to operate in lower part-load conditions for extended periods of time, improvements in the part-load efficiency of the individual plants are needed, especially in the lower part-load conditions in which its efficiency drops significantly. Second, a better overall fleet dispatch strategy is needed. The base case annual dispatch profiles represent the maximum variable range of operation that a fleet of NGCC may experience within the grid for each renewable scenario. While each and every NGCC could be dispatched to follow this highly dynamic load, fleet dispatch could include full-power dispatch of the hourly appropriate number of plants plus only one or two plants dispatched at part-load to meet the overall grid demand.

10.2 Dispatch Strategy

To investigate the optimum fleet dispatch strategy within the scope of this study, first the number of NGCC plants required to complement annual renewable production for each scenario is determined and then all of the NGCC plants in the grid are classified into one of three categories at every hour of the year; that is, plants that are shut down completely, plants that are turned on and off only to their full-capacity, and plants that are load-following.. Assuming that all NGCCs in the grid are of 395MW capacity the total number of plants is determined by the required dispatchable capacity in California for each of the scenarios. After the number of plants that are required for each renewable penetration scenario is calculated, the number of plants that are at each of the three operating states (full-capacity, load-following, or off) are calculated for each hour of the year. As discussed in the previous section, for the base case profile, all of the plants operate as load-followers; thus, none of the plants are operating at its full capacity that 100% of the demand

loads are met by the load-followers. The left-hand side Figure 23 of shows how the “Min” case is structured: the blue dashed line represents total demand load; the black solid line represents total power generated by the plants operating at their full capacity; each box represents power generated by single fleet. For the “Min” case, the number of plants that are operating at its full-capacity is increased up to the maximum number that is just below total hourly demand while only a few plants are dispatched to operate at part-load depending upon the hourly demand. The right-hand side of Figure 23 shows the demand profile for a load-following plant in the Min case.

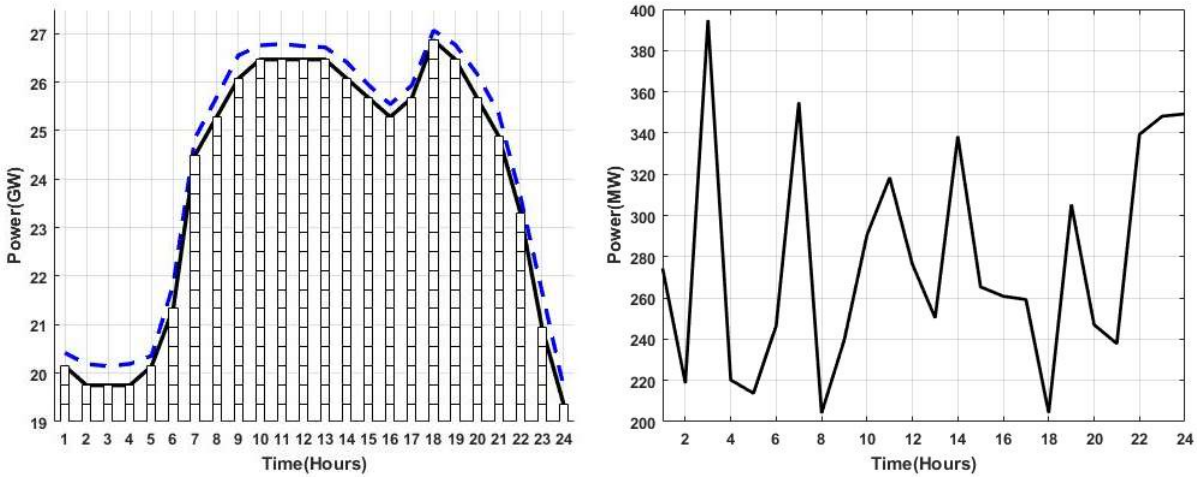

FIGURE 23: GRAPHICAL REPRESENTATION OF PLANT CLASSIFICATION MECHANISM FOR "MIN" DISPATCH AND AN EXAMPLE OF DEMAND PROFILE FOR A LOAD-FOLLOWING PLANT

In the results that follow, the degree to which this fleet dispatch strategy can be deployed is analyzed from 100% load-followers (the base case) in 10 percentage point decrements down to the “Min” case, which retains the number of load-following plants that is minimally required to meet all hourly dispatchable loads for each scenario. Figure 24 demonstrates that as renewable penetration increases the number of required dispatchable power plants decreases (more plants in the current fleet can be turned off). In addition, using the fleet dispatch strategy of Figure 23 to

varying degrees from 100% load followers down to the minimum number of load followers is presented for the 33%, 50% and 80% renewable penetration scenarios, respectively, in Figure 24.

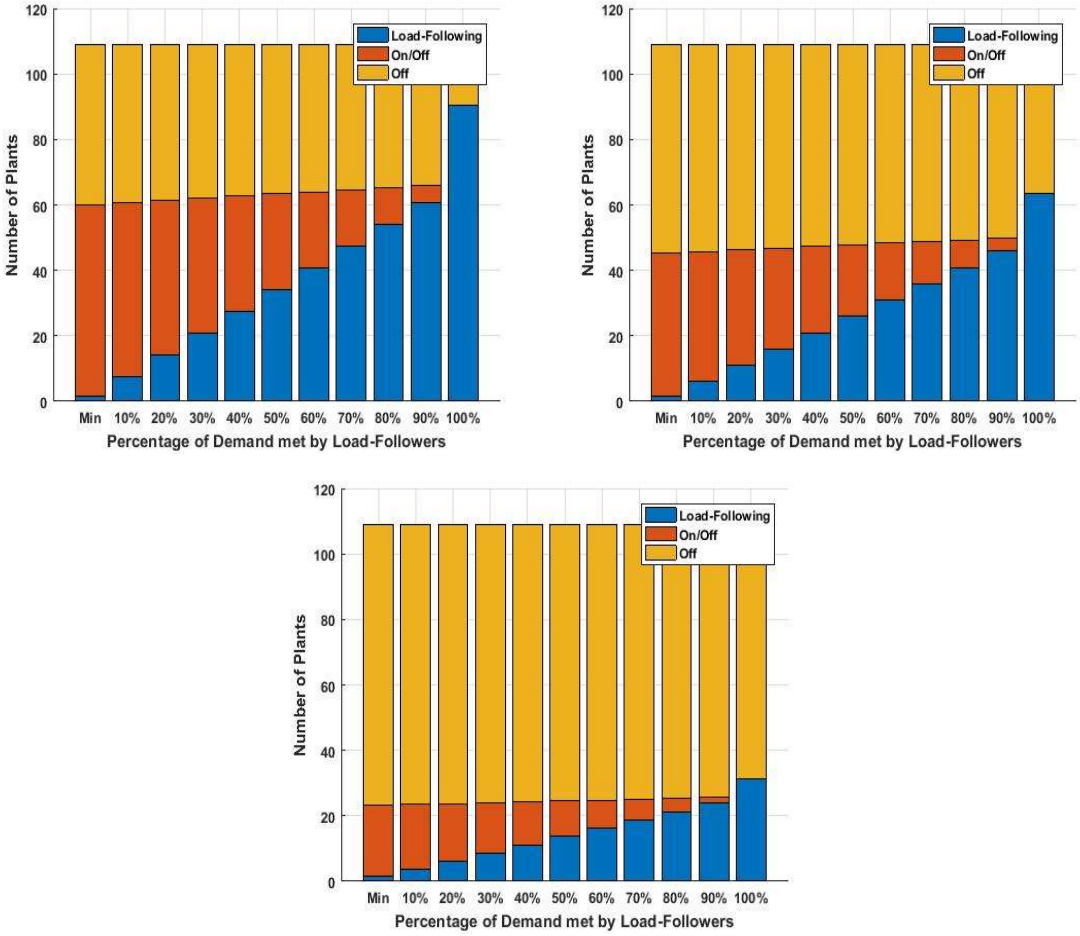

FIGURE 24: NUMBER OF PLANTS REQUIRED FOR VARIOUS FLEET DISPATCH SCENARIOS FOR 33%, 50%, AND 80% RENEWABLE PENETRATION

If every NGCC is of 395 MW capacity, then the total 42,777 MW of natural gas generation currently installed in California is represented by 109 of these NGCCs. For the dispatch scenarios of the 33% renewable penetration, 82.5% of the total plants is required to load-follow for the base case profile. As the number of load-following plants decreases from 82.5% (the base case) to 1.4% of the total plants (the Min case), the number of the on-and-off plants increases from 0% to 54% of the total. The inversely proportional relationship between the number of load-following and of

switching on-and-off plants are demonstrated, in less degree, in the dispatch scenarios of the 50% and 80% renewable penetration. For the dispatch scenarios with 50% renewables, the number of load-following plants decreases from 58.3% to 1.4% while the number of switching on-and-off plants increases from 0 to 40% of the total plants. For the dispatch scenarios with 80% renewables, the number of load-following plants decreases from 28.9% to 1.4% while the number of switching on-and-off plants increases from 0 to 20% of the total plants.

10.3 Emissions Analysis of Dispatch Strategies

In order to analyze the impacts of the fleet-wide dispatch strategies applied, the extent of the impacts in grid operation are calculated in terms of CO_2 emissions for the marginally varying dispatch scenarios with three different fleet control strategies and shown in Figure 25, Figure 26, and Figure 27. The emissions calculation considers emissions associated not only with steady-state power generation but, more importantly, extra emissions associated with dynamic operation. Ebrahimi et al. have presented emissions penalties associated with start-up, ramping and part-load operation [100]. The emissions penalties for different types of generators associated with different types of dynamic operation are shown in Table 3. Ebrahimi et al. have utilized these penalties by multiplying them to the full-load emissions factors presented in Table 4 [101]. In addition, although Ebrahimi et al. have considered part-load emissions only for operation under 30% of the full-load, in this work the part-load emissions penalties have been interpolated from the given factors up to the zero-penalty case of full-load emissions.

TABLE 3: EMISSIONS PENALTY ASSOCIATED WITH DYNAMIC OPERATION OF DIFFERENT TYPES OF GENERATORS [100]

Generator	Fuel	Start-up			Ramping			Part-load		
		NO_x	SO_x	$CO_{2,e}$	NO_x	SO_x	$CO_{2,e}$	NO_x	SO_x	$CO_{2,e}$
Coal	Coal	1	0.8	1.2	0.08	0.07	0.03	-0.03	-0.2	0.06
Petroleum coke	PC	1	0.8	1.2	0.08	0.07	0.03	-0.03	-0.2	0.06
Gas turbine	NG	1.8	0	0.3	0.01	0	0.01	0.16	0	0.17
Cogeneration	NG	1.8	0	0.3	0.01	0	0.01	0.16	0	0.17
Biomass	BIO	1.8	0	0.3	0.01	0	0.01	0.16	0	0.17
Steam turbine	NG	0	0	0.9	0.08	0	0.01	-0.19	0	0.06
Combustion turbine	NG	1.8	0	0.4	0.01	0	0.01	0.16	0	0.17
Internal combustion engine	NG	1.8	0	0.4	0.08	0	0.01	0.03	0	0.17
Combined cycle	NG	6.1	0	0.3	0.08	0	0.01	0.29	0	0.15
Oil gas turbine	Oil	1.8	0	0.4	0.01	0	0.01	0.16	0	0.17
Hydrogen fuel cell	H2	0	0	0	0	0	0	0	0	0

TABLE 4: EPA GENERATORS EMISSIONS FACTORS (LB/MMBTU) [101]

Generator	Fuel	NO_x	SO_x	CO	PM_{10}	NMOC	$CO_{2,e}$
Coal	Coal	2.854	8.100	0.210	7.725	0.025	2035.971
Petroleum coke	PC	2.854	8.100	0.210	7.725	0.025	2035.971
Gas turbine	NG	0.069	0.003	0.524	0.068	0.026	699.791
Cogeneration	NG	0.430	0.474	0.597	0.461	0.039	963.906
Biomass	BIO	1.316	0.150	3.589	1.735	0.233	1794.737
Steam turbine	NG	0.360	0.006	0.795	0.018	0.052	1149.657
Combustion turbine	NG	0.069	0.004	0.524	0.068	0.026	699.791
Internal combustion engine	NG	0.069	0.004	0.524	0.068	0.026	699.791
Combined cycle	NG	0.0532	0	0.437	0	0.011	628.718
Hydrogen fuel cell	H2	0.07	0.1	0.1	0.05	0.02	850
Oil gas turbine	Oil	0.069	0.004	0.524	0.0684	0.026	699.791

The calculated emissions including the impacts of dynamic operation penalties have been applied to the different NGCC generation profiles for an individual fleet under marginally varying dispatch strategies. Specifically, the number of start-ups for switching on-and-off plants in the grid is counted and multiplied by the start-up penalty. In addition, the emissions penalty associated with ramping-up to full-load is added to the start-up penalties for the on-and-off plants while that associated with ramping-up is calculated for each of the load-following plants that are required to ramp-up at any hour. The emissions penalties for different levels of part-load conditions are multiplied by the emissions factor of the combined-cycle plant in Table 4. All the calculated emissions are summed up on an annual basis for each of the dispatch strategies under different renewable penetration and presented in Figure 25, Figure 26, and Figure 27, by the type of NGCC

plant control schemes in Chapter 9, namely for the base-case control, for variable inlet guide vane (VIGV) control, and for variable speed (VS) control of the NGCC plants, respectively.

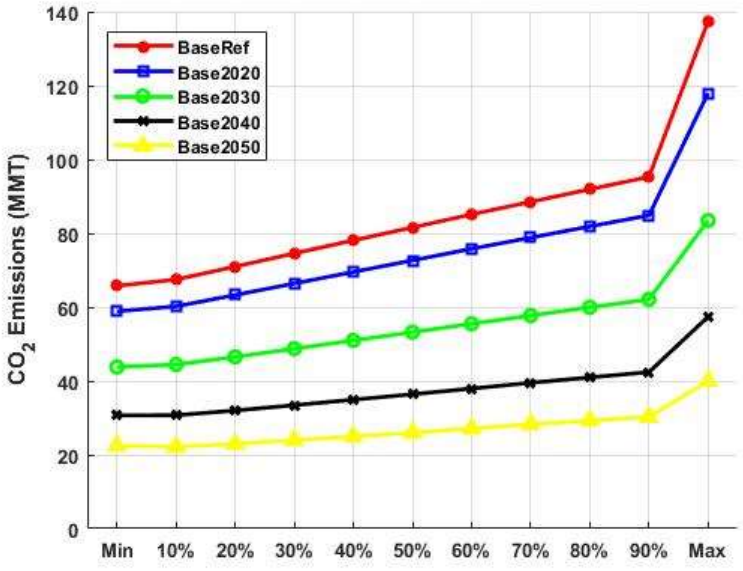

FIGURE 25: CO_2 EMISSIONS RESULTS OF DIFFERENT DISPATCH SCENARIOS WITH THE BASE CASE CONTROL FOR THE THREE RENEWABLE PENETRATION VALUES

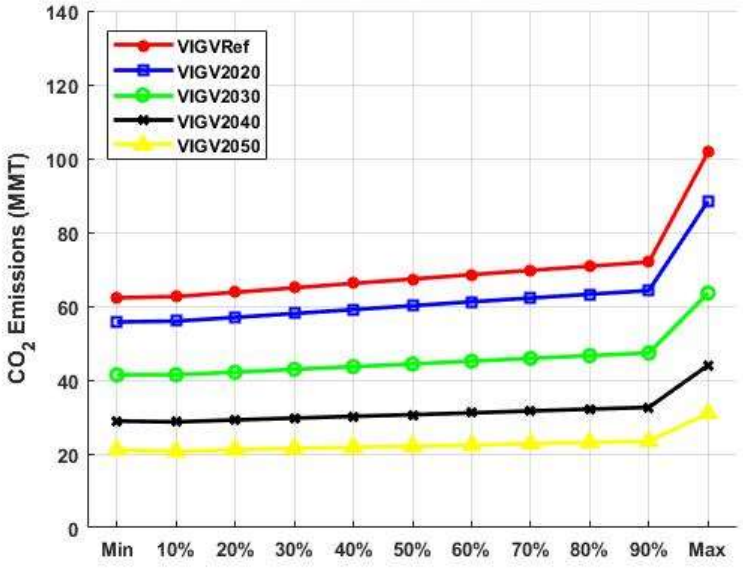

FIGURE 26: CO_2 EMISSIONS RESULTS OF DIFFERENT DISPATCH SCENARIOS WITH VIGV CONTROL FOR THE THREE RENEWABLE PENETRATION VALUES

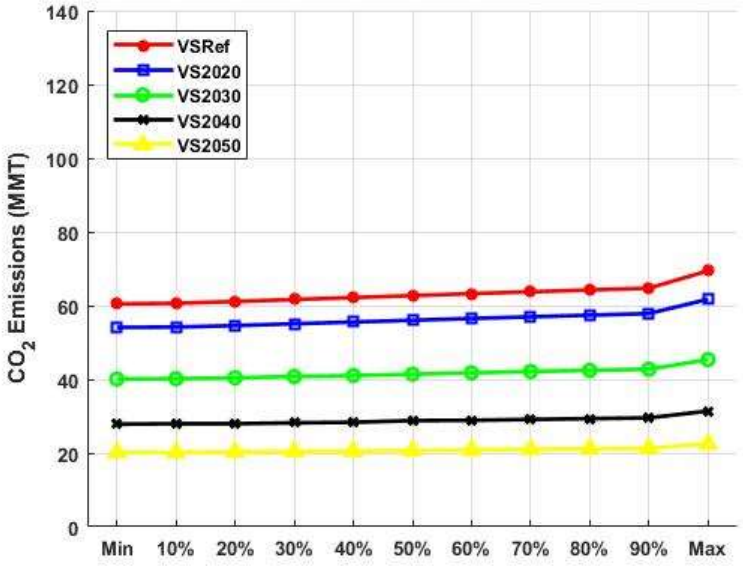

FIGURE 27: CO_2 EMISSIONS RESULTS OF DIFFERENT DISPATCH SCENARIOS WITH VS CONTROL FOR THE THREE RENEWABLE PENETRATION VALUES

For all three NGCC plant control strategies and for all three grid renewable penetration levels, significant emissions reductions are realized as one moves from dispatching all NGCC plants dynamically to dispatching only a few plants dynamically in the "Min" dispatch strategy. All of the "Min" dispatch cases deploy the maximum number of the on-and-off plants in the on-state while deploying the minimum number of load-following plants at each operating hour of the year, leading to the least total annual emissions. For the same renewable penetration, the base cases exhibit the most total emissions while the VIGV and VS cases follow in a decreasing order.

10.4 Climate Change Impacts on Grid Operation

10.4.1 Variable Resolution Community Earth System Model (VR-CESM)

Many climate projections are publicly available (e.g., CMIP5 (Coupled Model Intercomparison Project) datasets, Taylor et al., 2012), however, they generally are at relatively coarse spatial

resolution (1 degree) for application to renewable energy studies. In this study, the variable-resolution community Earth system model (VR-CESM) is used to generate a refined-resolution (14 km) climate projection over the western U.S under the Representative Concentration Pathway (RCP) 8.5 scenario, which assumes that emissions continue to rise throughout the 21st century. This refined resolution improves simulation accuracy and provides projections that are more spatially consistent with the renewable power generation facilities. The technical details of VR-CESM and its climatological evaluation were presented in Xu et al. (2021) and are only briefly introduced here [102].

The VR-CESM simulation is global with 14 km resolution over the western U.S. and eastern China and 1 degree resolution over the rest of the globe. The simulation spans 1970 to 2006 for the historical period and 2007 to 2050 for the future RCP8.5 period, and is driven by prescribed monthly sea ice and sea surface temperature datasets. The radiation and wind speed model outputs were resampled to a regular spatial grid for this study.

10.4.2 Consequences of Climate Change Impacts on Grid Operation

To apply climate change impacts on availabilities of solar and wind, VR-CESM outputs of incident solar radiation and wind speed data are used with appropriate spatial filters under the assumption that the state fully utilizes its utility solar and wind potentials to meet the RPS goal for each target year. For solar, coordinates of the desert areas in Southeastern California have been used as the filters while, for wind, locations with Weibull shape factor (k) between 1.5 and 2.5 in Weibull probability distribution density function and Weibull scale parameter (c) calculated with the average wind speed, respectively shown in Equation 74 and Equation 75 are used:

$$f(v) = \frac{k}{c}\left(\frac{v}{c}\right)^{k-1} e^{\left[-\left(\frac{v}{c}\right)^{k}\right]}$$ Equation 74 [103]

$$c = \frac{2}{\sqrt{\pi}}\bar{v}$$ Equation 75 [103]

Where k is the Weibull shape factor, v the wind speed, and c the Weibull scale parameter. The shape factor is determined by regression fitting the average wind speed data for each data point (14km resolution mesh) over the state of California. The Weibull shape factor characterizes the how often and how fast the wind is going to blow and the Weibull shape factor of 2 represents a location with consistent wind and occasional hard wind [103]. Thus, based on the assumption that the state of California is going to fully utilize its inland wind potentials in order to meet its RPS targets, the regions with Weibull shape factor between 1.5 and 2.5 are selected. Even if the appropriate spatial filters have been applied, hourly profiles of solar and wind power profiles impacted by climate change have to be generated from the daily average provided by VR-CESM. To do so, the hourly solar and wind profiles from HiGRID are respectively scaled with the dimensionless scale factors of solar and wind power, calculated as a daily ratio of target year data over 2016 data. Table 5 demonstrates grid renewable penetration for different scenarios in different target years.

TABLE 5: GRID RENEWABLE PENETRATION VALUES OF DIFFERENT TARGET YEARS FOR DIFFERENT SCENARIOS

	Grid Renewable Penetration				
Year	Reference (2016)	2020	2030	2040	2050
Reference	25.8%	33.3%	50.14%	61.7%	72.66%
Climate Change	25.8%	32.24%	48.07%	56.8%	66.69%
Resolving CC	25.8%	33.23%	50.1%	61.7%	72.65%

When the dimensionless scale factors are applied to reflect the climate change impacts on renewable availabilities and their power generation profiles, the planned increase in the solar and wind capacities cannot fulfill the RPS targets in the future. To address this concern, solar and wind installment has been increased; the extent of extra increases in solar and wind is determined through an optimization mechanism minimizing the extra installments. With the proposed extra increases, real grid penetration values can finally meet the renewable penetration targets. Figure 28 compares grid-wide greenhouse gas emissions with and without climate change impacts when the different dispatch strategies have been applied.

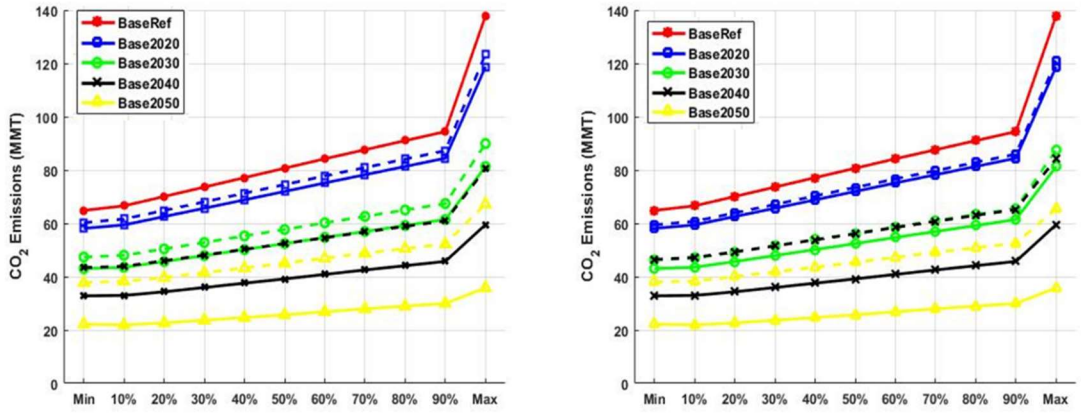

FIGURE 28: TOTAL CO2 EMISSIONS WITH THE BASELINE FLEET CONTROL FOR DIFFERENT DISPATCH STRATEGIES AND RENEWABLE PENETRATION WITH (DASHED) AND WITHOUT (SOLID) CLIMATE CHANGE IMPACTS (LEFT: REFERENCE SCENARIO; RIGHT: RESOLVING CC SCENARIO)

Along with the extra increases in solar and wind capacities to meet the grid RPS targets, there are other consequences of the climate change related to grid operation. First, the grid wide GHG

emissions will increase. The emissions increase due to climate change for a target year is greater with increasing grid renewable penetration. With more solar and wind, the grid becomes more susceptible to intermittency of solar and wind that the NGCCs need to operate more dynamically resulting in more GHG emissions. When the solar and wind capacities are manipulated to meet the proposed RPS targets, the climate change impacts on the renewable availabilities and consequently the emissions are mitigated, but not completely. While mitigated by manipulating the solar and wind capacities, the climate change impacts make the operational profiles of the natural gas-based power generation units more dynamic by increasing startups and shutdowns occurrences of the on/off plants and extending duration of operation in lower part-load conditions. Figure **29** demonstrates another consequence of the climate change impacts on grid operation, the increase in the NGCC units.

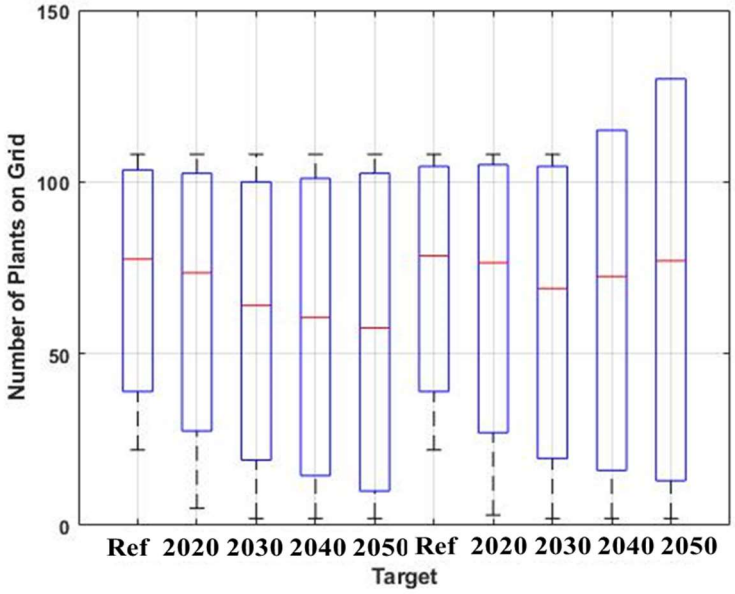

FIGURE 29: CHANGES IN NGCC OPERATION WITHIN THE GRID WITH AND WITHOUT CLIMATE CHANGE

The first fives boxplots in Figure **29** represent number of the plants in the grid to complement renewables without climate change impacts for the different grid renewable penetration while the second fives represent the number of the plants to do the same with climate change impacts yet without the wind and solar capacity manipulation. The maximum of the box plots refers to the NGCC capacity in grid and the upper quartile of the box plots refers to total number of the plants operating at respective peak load and the minimum refers to the minimum number of the plants in-operation. Note that the NGCC capacity needs to increase for 61.5% and 72.5% RPS targets with the climate change impacts just to meet the peak demand for the grid.

11. SOFC-GT Hybrid System Simulation

The transition to a 100% renewable grid requires power systems to be dynamically dispatchable and fuel flexible with near-zero emissions. Large-scale fossil fuel power plants with proven flexibility and durability can be dynamically dispatched to maintain grid reliability. However, these power plants need to be replaced with renewable infrastructure as grids are decarbonized. Solid oxide fuel cell (SOFC) systems are known for their fuel flexibility ranging from natural gas to biogas to renewable hydrogen and for high efficiency even at the distributed power scale. If SOFC systems could also be engineered for highly dynamic dispatchability, they could locally and seamlessly support high renewable use in future grids. When SOFCs are integrated with gas turbine (GT) engines, the integrated system boosts very high efficiency, fuel flexibility, and ultra-low emissions, but unproven dynamic dispatch capabilities. In this work, we propose a novel SOFC-GT system configuration and control strategy, and we show dynamic dispatch capabilities when fueled with natural gas and mixtures of natural gas and hydrogen. The hybrid systems can achieve net electrical efficiencies higher than 70% at nominal conditions, even at the distributed power scale of 100 kW_{el}. It is also proven – using real wind and solar photovoltaic generation profiles – that such an SOFC-GT system, with a proper control strategy, can complement high levels of variable renewable power without incurring component degradation and maintaining a net electric efficiency >50% at part-load conditions as low as 27% of the nominal load. Furthermore, the SOFC-GT systems will be able to seamlessly transition to rich renewable hydrogen-natural gas blends up to 70%v of hydrogen, without any configuration modification. These conclusions support the considerable technical advantages that SOFC-GT systems may provide compared to competing fossil fuel combustion-based technologies and increase

confidence that highly renewable electric grids can be implemented with complementary, highly efficient and zero emissions dynamic dispatch of renewable-fueled SOFC-GT systems.

11.1 Description of the Proposed Hybrid System Configuration

For air side, the proposed configuration has two heat exchangers in series to ensure more air preheating and one bypass valve mainly to control the cathode inlet temperature. For fuel side, the configuration includes one heat exchanger and pre-reformer to ensure fuel preheating as well as high efficiency. In addition, the configuration is equipped with a recycle blower to compensate for pressure loss during the fuel cycle. Figure 30 shows the schematic diagram of the SOFC-GT hybrid system proposed in this study.

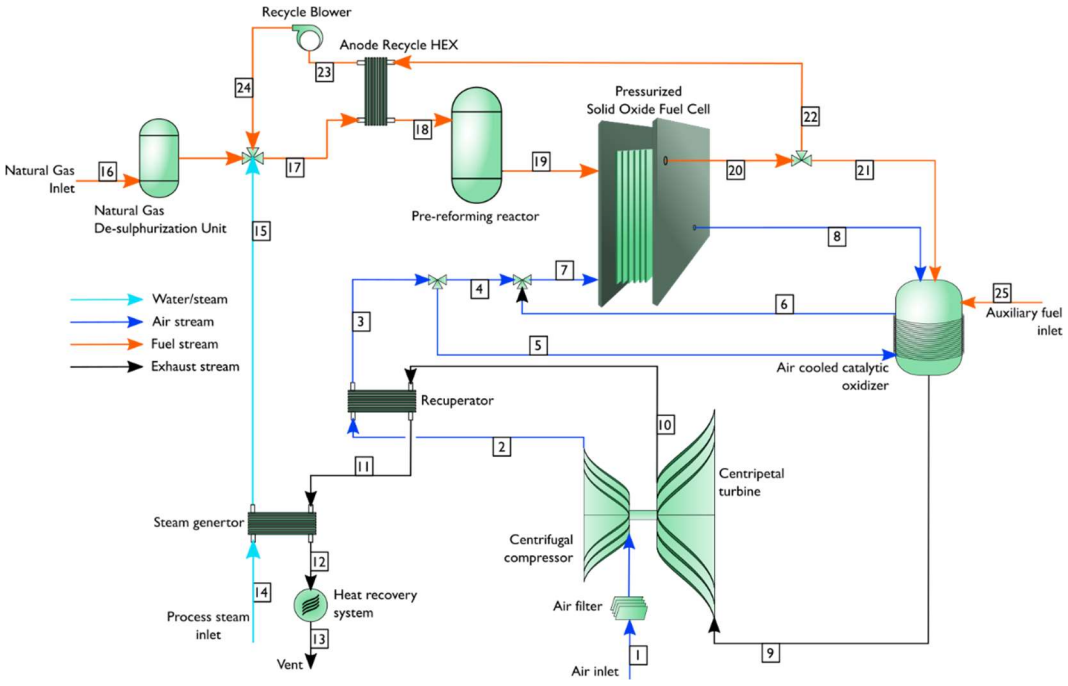

FIGURE 30: SCHEMATIC DIAGRAM OF A PROPOSED SOFC-GT HYBRID SYSTEM

There are two main streams: the fuel stream begins with #13 on the very left of Figure 30. Depending on the recycle ratio, some of it will be heading to an oxidizer for more power generation in GT while the rest will be recycled to not only to heat up the main fuel stream but to be fed back into the main fuel stream to ensure steam-to-carbon ratio. The air stream begins with #1 on the right of Figure 30. It is pressurized by a compressor and heated up by two heat exchangers in series and then led into the fuel cell for giving up oxygen and cooling the stack.

Inside the stack not only includes the cell where the electrochemical reactions occur for power generation, but also includes the empty volume, called manifold. As this fuel cell stack runs with pressurized air and fuel flows, change in pressure dynamics could affect the fuel cell performance so as the performance of the turbine downstream. Furthermore, a drastic change in flow pressure can be detrimental to the cell, possibly causing a system failure. The manifold is incorporated into the stack before the inlet to function as a pressure buffer maintaining pressure steady upon change in system pressure dynamics.

TABLE 6: COMPONENT PARAMETER ASSUMPTIONS

Component parameter assumptions	
Ambient temperature (K)	298
Ambient pressure (kPa)	101.3
Water temperature (K)	288
Generator Efficiency (%)	.95
DC-AC efficiency (%)	.97
AC-AC efficiency (%)	.80
Compressor isentropic efficiency (%)	.73
Turbine isentropic efficiency (%)	.785
Turbine inlet design temperature (K)	1223
Gas turbine design pressure ratio	3
Gas turbine design flow rate (kg/s)	0.1643
Blower isentropic efficiency (%)	.65

11.2 System Performance at Nominal Operating Conditions

The SOFC-GT hybrid system generates 124.5 kW of nominal net electric output at 71.38% net electric efficiency (based on the LHV of the fuel) when the global fuel utilization ratio is set at 82%. Out of 124.5 kW, 116.9 kW is generated by the fuel cell stack at the operating voltage and current density of 0.876 V and 0.485 A cm^{-2}, respectively. The gas turbine is responsible for 7.83 kW of the power, resulting in a SOFC/GT power ratio of 15. Before the power electronics, the hybrid system in nominal condition generates 144.4 kW gross power output at 82.8% overall efficiency. Out of 144.4 kW, 130.3 kW is the gross power generated by the fuel cell stack and the gas turbine combined while 14.1 kW is the thermal power output at the system exhaust. Table 7 summarizes variables relevant to performance of the entire hybrid system as well as that of the fuel cell stack within the system and Table 8 provides thermodynamic properties of the flows for the nominal operating condition.

TABLE 7: OVERALL ENERGY BALANCE OF THE SOFC-GT HYBRID PLANT

Plant performance	
Fuel inlet (LHV) [kW]	174.37
Fuel cell gross power [kW]	120.5
Fuel cell net AC power [kW]	116.89
GT gross power [kW]	9.78
GT net power [kW]	7.83

Blower power [kW]	-0.25
Overall gross power [kW]	130.28
Overall net power [kW]	124.47
Gross efficiency [%]	74.71
Net electric efficiency LHV [%]	71.38
CO2 emissions [kg s^{-1}]	0.0097
CO2 specific emission [kg MWh^{-1}]	279.59

TABLE 8: THERMODYNAMIC PROPERTIES OF FLOWS FOR NOMINAL OPERATING CONDITION

	Temp (°C)	Pressure (kPa)	MassFlow (g/s)	MolarFlow (mol/s)	m x LHV	CH_4	CO	CO_2	H_2	H_2O	N_2	O_2
1	25.0	101.3	159.1	5.517	0.000	0%	0%	0%	0%	0%	79%	21%
2	222.8	322.8	159.1	5.517	0.000	0%	0%	0%	0%	0%	79%	21%
3	632.3	321.8	159.1	5.517	0.000	0%	0%	0%	0%	0%	79%	21%
4	632.3	321.8	84.6	2.934	0.000	0%	0%	0%	0%	0%	79%	21%
5	632.3	321.8	74.5	2.583	0.000	0%	0%	0%	0%	0%	79%	21%
6	826.7	321.8	74.5	2.583	0.000	0%	0%	0%	0%	0%	79%	21%
7	724.1	319.8	159.1	5.517	0.000	0%	0%	0%	0%	0%	79%	21%
8	752.2	315.8	147.7	5.161	0.000	0%	0%	0%	0%	0%	84%	16%
9	881.3	310.8	162.8	5.740	0.000	0%	0%	4%	0%	8%	76%	13%
10	657.4	103.0	162.8	5.740	0.000	0%	0%	4%	0%	8%	76%	13%
11	280.1	102.0	162.8	5.740	0.000	0%	0%	4%	0%	8%	76%	13%
12	277.0	101.5	162.8	5.740	0.000	0%	0%	4%	0%	8%	76%	13%
13	100.0	101.3	162.8	5.740	0.000	0%	0%	4%	0%	8%	76%	13%
14	15.0	101.3	2.7	0.150	0.000	0%	0%	0%	0%	100%	0%	0%
15	126.6	101.3	2.7	0.150	0.000	0%	0%	0%	0%	100%	0%	0%
16	15.0	350.0	3.7	0.222	0.174	98%	0%	1%	0%	0%	1%	0%
17	381.0	340.2	26.2	1.208	0.236	18%	7%	21%	13%	41%	1%	0%
18	705.6	316.8	26.2	1.208	0.236	18%	7%	21%	13%	41%	1%	0%
19	574.1	315.8	26.2	1.288	0.242	14%	6%	23%	25%	32%	0%	0%

20	822.7	315.8	37.6	1.642	0.102	0%	8%	25%	16%	50%	0%	0%
21	822.7	313.8	15.1	0.657	0.041	0%	8%	25%	16%	50%	0%	0%
22	822.7	313.8	22.6	0.985	0.061	0%	8%	25%	16%	50%	0%	0%
23	390.4	305.2	22.6	0.985	0.061	0%	8%	25%	16%	50%	0%	0%
24	397.0	340.2	22.6	0.985	0.061	0%	8%	25%	16%	50%	0%	0%
25	15.0	350.0	0.0	0.000	0.000	98%	0%	1%	0%	0%	1%	0%

11.3 Sensitivity Analysis on Volume of Manifolds within Fuel Cell Stack

In order to assess the effect of volume of the fuel cell manifolds on pressure dynamics, the volume of the manifolds is halved, doubled, tripled, and quadrupled; at the same time, the hybrid system model simulates a 100-80-100% step change. The simulation results are compared to the one with the default manifolds volume. Figure 31 demonstrates how changes in the manifolds volume affect the pressure dynamics across the cathode.

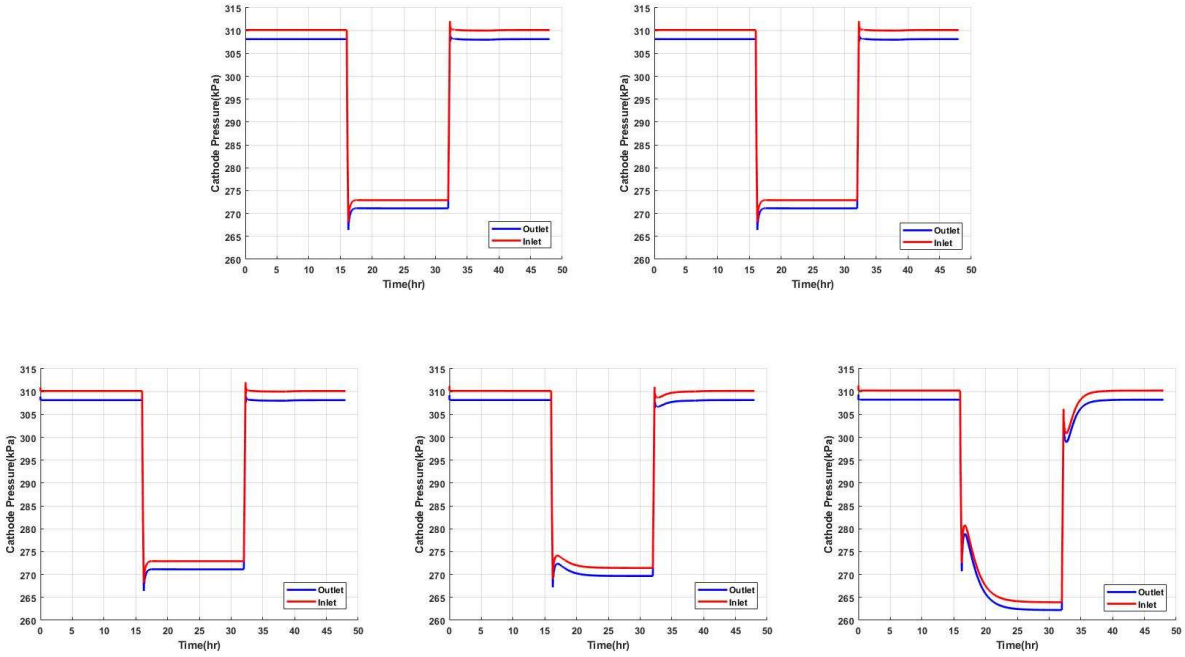

FIGURE 31: SENSITIVITY ANALYSIS ON VOLUME OF THE FUEL CELL MANIFOLDS

(TOP LEFT: X 1/2, TOP RIGHT: DEFAULT, BOT LEFT: X 2, BOT MID: X 3, BOT RIGHT: X 4)

The volume of the manifolds begins to affect the cathode pressure dynamics only when the volume is tripled. When tripled, the time it takes for the pressure to stabilize increases to 3 hours; when quadrupled, the time it takes to stabilize increases to 5.5 hours. In addition to the increase in the stabilizing time, additional 3% pressure loss occurs when there is the step change.

11.4 End-of-Life Performance

For commercial deployment of the SOFC-GT hybrid system, detailed understanding of the system behaviors and characteristics throughout its life-cycle is required. As the fuel cell approaches its end-of-life, power generation with the fuel cell will become less and less efficient with polarization potentials, especially ohmic and anode polarization, expecting to increase [104], [105], [106]. To simulate the end-of-life performance of the fuel cell and the increasing polarization potential, ohmic resistance of the fuel cell materials is increased. Table 9 compares the hybrid system performance of the three cases when 1) the fuel cell normally operates, 2) the fuel cell reaches its end-of-life and is asked to generate the same current level as the base case, 3) the current level and fuel utilization ratio are manipulated to operate the system within its operational constraints.

TABLE 9: PERFORMANCE COMPARISON BETWEEN NORMAL AND DEGRADED FUEL CELL

	Base	**Constant Current**	**35% Decrease + FU 75%**
FC Power (kW)	120.5	103.1	66.7
GT Power (kW)	9.8	19.9	11.89
System Efficiency (%)	71.4	67.7	61.0
TIT (K)	1152.6	1405.3	1168.2
Voltage (V)	0.876	0.749	0.766
Current Dens (A/cm2)	0.485	0.485	0.307
Tcath,out (K)	1024.4	1304.7	1025.3
Tpen, avg (K)	1087.2	1364.3	1085.3
ΔT (K)	28.1	94.1	29.0

Compared to the base case, there are two conspicuous trends emerge in the system level when the fuel cell reaches its end-of-life. First, the power output decreases by 15%. The voltage output decreases with increasing ohmic polarization even when the fuel cell generates the same level of current. The power output decreases by 15% from 120.5 kW to 103.1 kW corresponding to the 15% decrease in voltage from 0.876 V to 0.749 V. Second, the system operating temperature increases. The cell degradation causes increases in material resistivity, resulting in higher ohmic polarization. When the same level of current flows through the material with higher resistivity, more power is dissipated in form heat contributing to higher material and flow temperature. As a result, the temperatures downstream of the fuel cell as well as gas turbine power output increase; the cathode outlet temperature increases by 27%, the temperature gradient across the stack by 235%, turbine inlet temperature by 22%, and gas turbine power output by 103%. However, the gas turbine is designed to generate 12kW at its nominal condition that gas turbine system might not be able to physically tolerate the simulated TIT and power output.

In response, the fuel utilization ratio and current are manipulated to prevent any temperature overshooting and to maintain the system operation point within its limits. The current is decreased 35% to reduce the amount of heat generated within the fuel cell through its electrochemical reactions. However, according to the current control scheme, the decrease in current leads into decrease in main fuel flow rate; with the global fuel utilization ratio maintained at the design condition, these decreases eventually decreases the turbine inlet temperature. To ensure that there are enough fuel left at the fuel cell outlet for TIT above 1150K, the fuel utilization ratio is decreased from 82% to 75%. As a result, all the temperatures ($TIT, T_{cath,out}, T_{pen,avg}, \Delta T_{stack}$) become

comparable to those of the design conditions, only different by 1.4%, 0.08%, 0.17%, and 3% respectively.

At the same time, with the abovementioned operating conditions, the gas turbine is able to generate 11.89 kW of power, a physically possible power output for a 12kW radial turbine. The fuel cell power output decreases by 45% from its design power output and 35% from its end-of-life maximum power output.

11.5 Dynamic Simulation of the Hybrid System

11.5.1 Step Response

The dynamic model for SOFC-GT hybrid system and its controller have been developed. To verify dynamic performance of the SOFC-GT hybrid system, the model has simulated a simple demand load profile of various step changes. The step change simulation has taken place within a 24-hour period and ramping down-and-ups are evenly separated (8 hours apart) to allow the model enough to reach steady-state electrochemically, mechanically, and thermally. The system characteristics, including power generated by fuel cell and gas turbine, fuel flow rate, system electrical efficiency, and global fuel utilization ratio, upon 100-90-100%, 100-70-100%, 100-50-100% step changes are shown in Appendix: Dynamic Simulation – Step Change. Figure 57 and Figure 58 entail fuel cell and gas turbine specific characteristics while the hybrid system simulates the 100-50-100% step change. Figure 32 shows the power demand profile simulated by the fuel cell and the system (FC+GT) power as a result of controlling the fuel cell relevant parameters for the 100-20-100% step change. Figure 33 shows the changes in system parameters including global fuel utilization, system efficiency, and valve positions for the same step change.

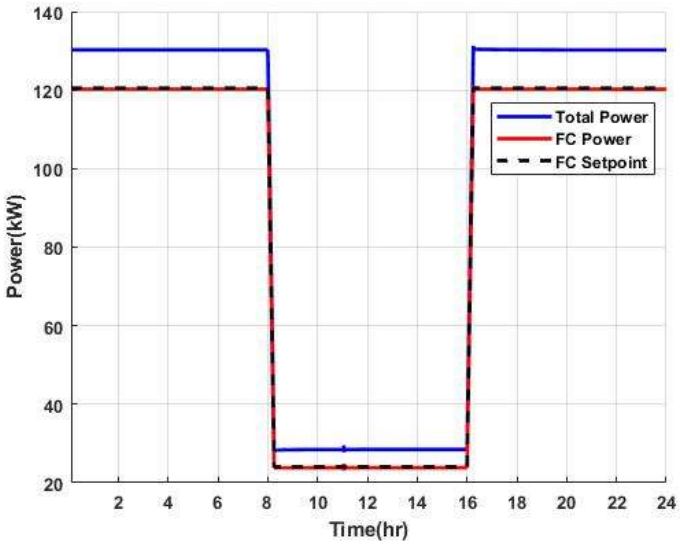

FIGURE 32: SYSTEM AND FUEL CELL POWER PROFILES

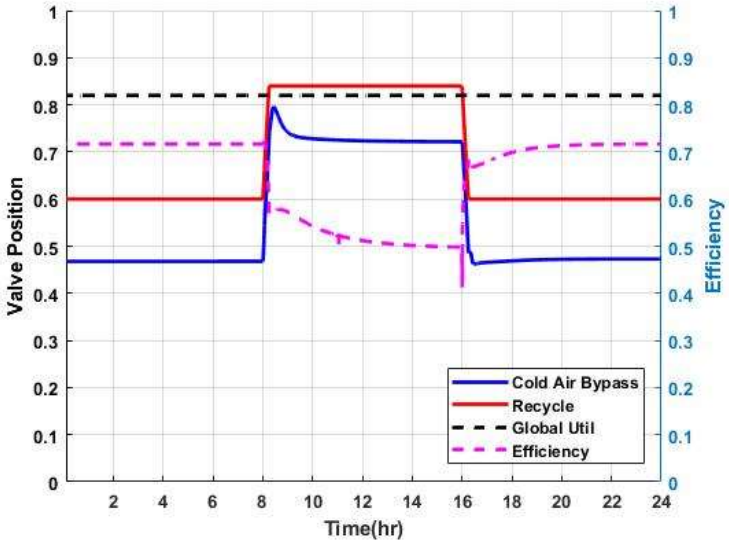

FIGURE 33: SYSTEM PARAMETERS OVER THE STEP CHANGE SIMULATION

The fuel cell power is controlled with the current and the gas turbine power is controlled with RPM setpoint imposed by cathode outlet temperature. The simulated power result demonstrates smooth profiles over the 100-20-100% step change. Over the step change, the global fuel utilization ratio

of the fuel cell (fuel utilization ratio including the recycle) is controlled at 82% by manipulating fuel flow rate at the system inlet as well as the fuel recycle ratio. This hybrid system has a nominal electrical efficiency of slightly over 70% and even for such a large step change, the efficiency is maintained above 50%. The last system parameter to discuss is the cold air bypass valve position, which is manipulated to control fuel cell cathode inlet temperature, leading to discussion of two main challenges in dynamic operation of the SOFC-GT hybrid system. They are thermal and flow management. Figure 34: Compressor and turbine maps shows the compressor and turbine performance maps and Figure 35 shows mass flow rates at various points throughout the system.

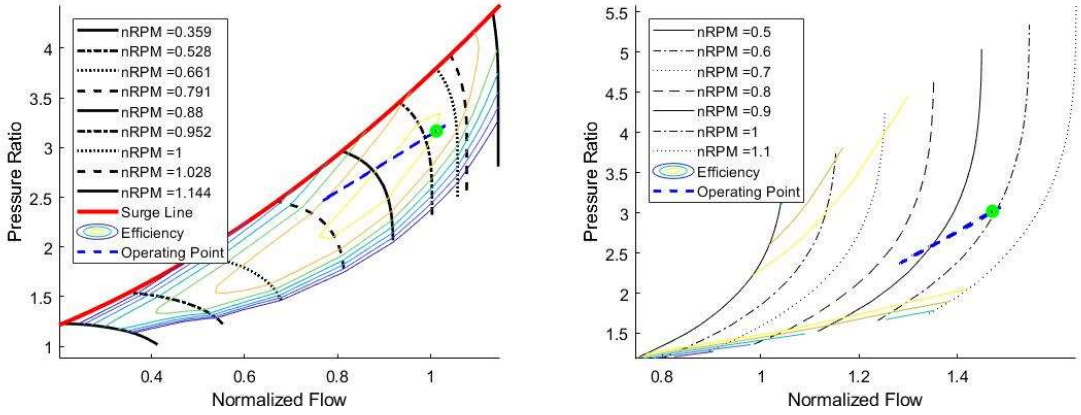

FIGURE 34: COMPRESSOR AND TURBINE MAPS

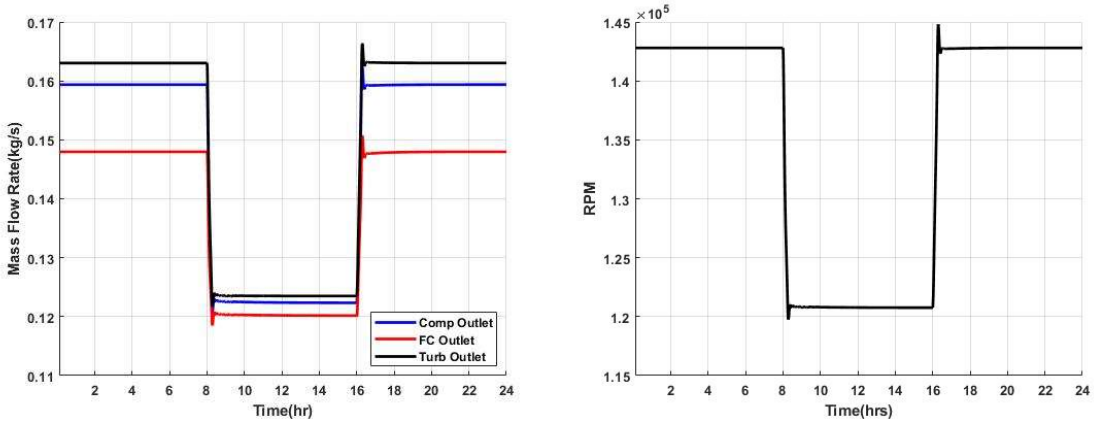

FIGURE 35: MASS FLOW RATES AT COMPRESSOR OUTLET, CATHODE OUTLET, AND TURBINE OUTLET AND RPM

In Figure 34, a blue line and green dot respectively represent a course of operation and final operation point. According to the figures, the hybrid system has been controlled successfully within the compressor surge/stall limits. Although the system air intake is indirectly controlled by imposing different RPM setpoints based on the cathode outlet temperature, the mass flow rate profiles match the change in shaft RPM. Compared to the mass flow rate at the compressor outlet, the mass flow rate at the cathode outlet is decreased because of oxygen ions transferred for the fuel cell operation; the mass flow rate at the turbine outlet is increased because of remaining and additional fuel combusted to maintain turbine inlet temperature (TIT). Figure 36 demonstrates temperature profiles at various points.

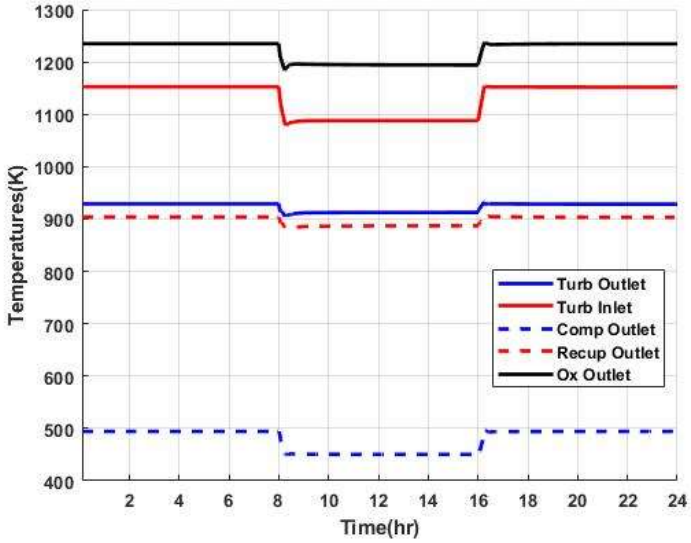

FIGURE 36: TEMPERATURE PROFILES AT VARIOUS POINTS THROUGHOUT THE HYBRID SYSTEM

Over the course of the step change, the turbine inlet temperature is maintained above 1100 K not only to ensure GT power contribution but more importantly to keep the entire system warm

enough. When the fuel cell operates in lower load conditions (= lower current density), less heat is generated that thermal management becomes more challenging and significant. Figure 37 demonstrates anode and cathode flow temperature profiles, respectively.

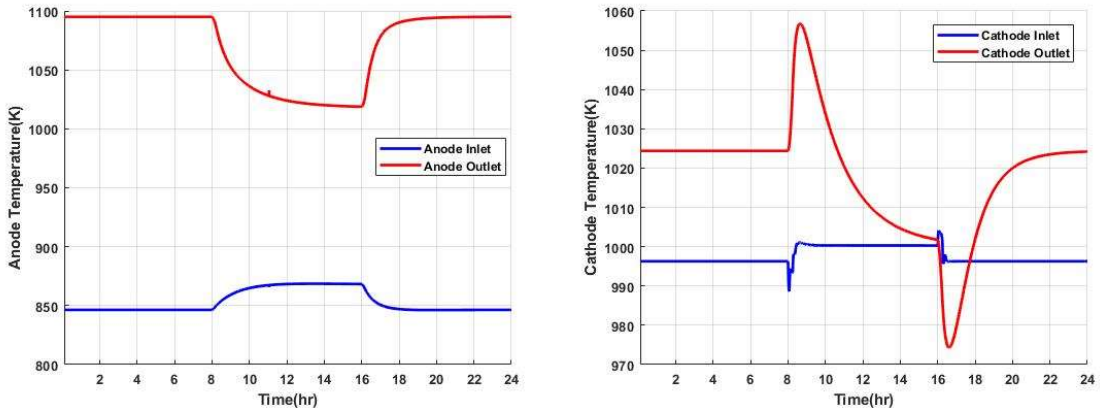

FIGURE 37: ANODE AND CATHODE FLOW TEMPERATURE PROFILES

As expected, for the anode temperature profiles, less amount of heat is generated in the 20% load condition leading to smaller temperature difference between anode inlet and outlet flows during the 20% load condition. For the cathode temperature profiles, the cathode inlet flow temperature is explicitly controlled with the cold air bypass valve while the target temperature depends on the fuel cell power ratio as shown in . In addition, starting at hour 16, the cathode outlet temperature becomes lower than the inlet temperature. The inversion of the inlet and outlet temperature is mainly caused by two reasons. For the lower power setting, the fuel cell experiences less exothermicity due to low current density. In addition, as the system ramps back up to 100%, the shaft RPM is increased leading to a sudden increase in air flow rate; due to thermal inertia of the fuel cell, the outlet temperature stays lower than the inlet for about two hours and reaches a thermal steady-state in about 8 hours.

11.5.2 SOFC+GT systems to complement renewable generation

SOFC-GT hybrid systems have the potential to displace NGCCs as load-following plants in future grids. For a 100 kW size-class system, the SOFC-GT unit is likely to complement a single source of renewable energy, most likely a solar photovoltaic (PV) or wind, in a microgrid as a behind-the-meter configuration, or operate as a modular fleet to follow the increasing fluctuations of the transmission grid. In this work, we restrict to the evaluation of the behind-the-meter microgrid scenario without any energy storage systems. Complementing the renewables represents that at each time instant (t=t_i), the summation of the generating systems (SOFC-GT unit and grid RES) power output must equal the load profile as shown in Equation 76.

$$\dot{W}_{SOFC-GT} + \dot{W}_{RES} = \dot{W}_{Load} \qquad \text{Equation 76}$$

Consequently, given a specified demand profile ($\dot{W}_{Load}$) as a function of time t, if the renewables power output decreases ($\frac{\partial \dot{W}_{RES}}{\partial t} < 0$) – e.g., due to lack of wind or solar resources – the dispatchable and controllable SOFC-GT unit must compensate ($\frac{\partial \dot{W}_{SOFC-GT}}{\partial t} > 0$) to avoid load shedding issues. Therefore, the load-following plants must be able to dynamically dispatch power to complement intermittent renewable power sources in a grid [7]. In the load-follower's operational standpoint, its demand needs to be calculated by subtracting the renewable generation from the load as shown in Equation 77.

$$\dot{W}_{SOFC-GT} = \dot{W}_{Load} - \dot{W}_{RES} \qquad \text{Equation 77}$$

Under this scenario, we assume a microgrid composed of a SOFC-GT hybrid system and single renewable power generator (solar or wind), requires 130 kW baseload generation ($\dot{W}_{Load} = 130$ kW) at all times. The solar and wind profiles are generated via the Holistic Grid Resource

Integration and Deployment (HiGRID) tool [98]. Using the tool, a year-long profile of the grid generation mix is generated. Then, 24-hour profiles of solar and wind are extracted and rescaled to produce the demand profiles for the SOFC-GT hybrid system used alongside a solar photovoltaic or wind. Figure 38 through Figure 40 show the microgrid demand in dashed black, the hybrid system power generation in solid blue, and the solar/wind generated profiles in dashed red. For each scenario, the demand for the load-follower is calculated by subtracting the renewable generation (dashed red) from the microgrid demand (dashed black). Figure 38 through Figure 40 continue with the hybrid system operating in accordance with the calculated demand to complement solar PV in a sunny day, in a cloudy day and wind throughout a week.

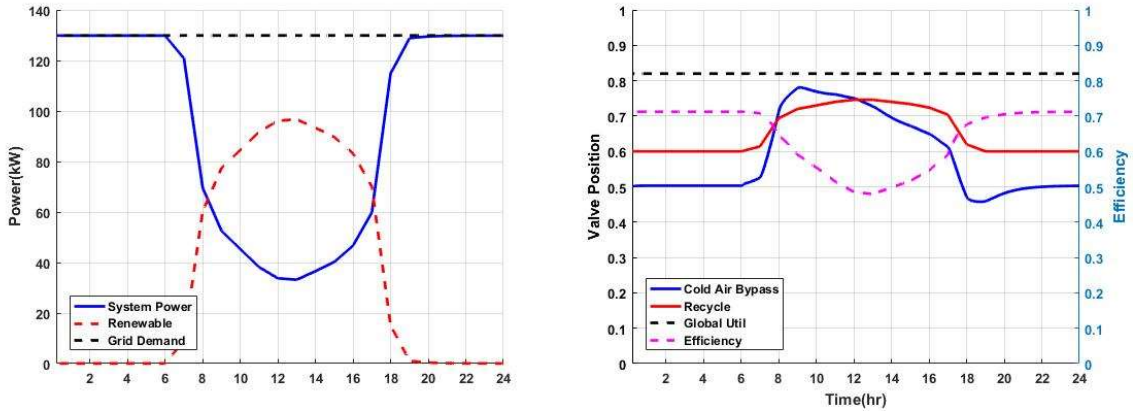

FIGURE 38: HYBRID SYSTEM SIMULATION RESULTS COMPLEMENTING SOLAR ON A SUNNY DAY

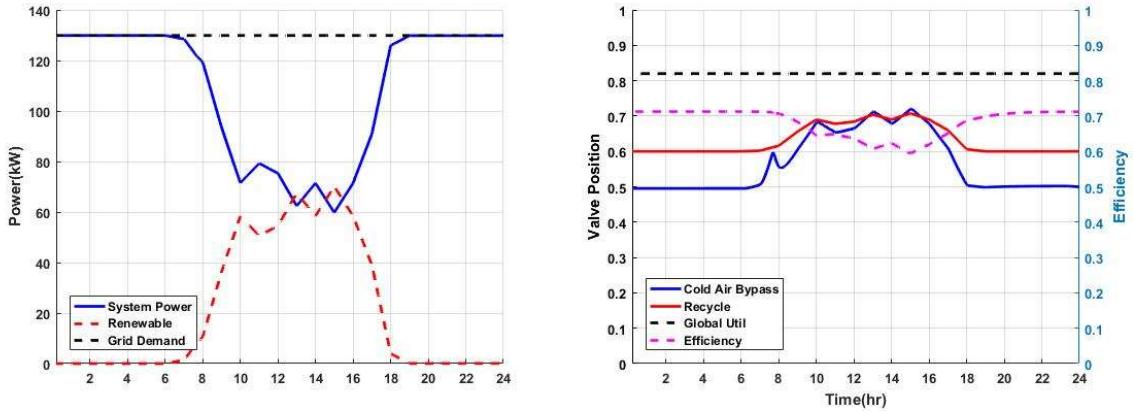

FIGURE 39: HYBRID SYSTEM SIMULATION RESULTS COMPLEMENTING SOLAR ON A CLOUDY DAY

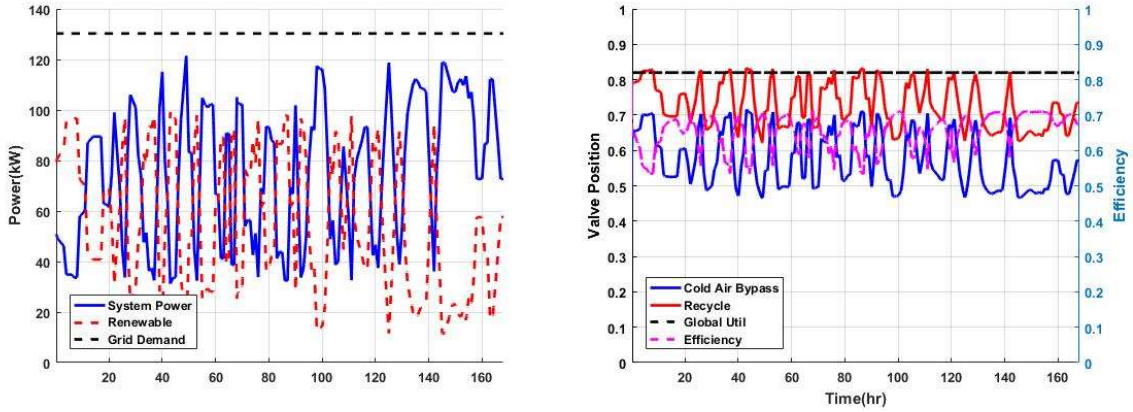

FIGURE 40: HYBRID SYSTEM SIMULATION RESULT COMPLEMENTING WIND FOR A WEEK

The SOFC-GT hybrid system has successfully complemented solar and wind while maintaining global fuel utilization of 82% and system electrical efficiency above 50% at all times. For the scenarios in which the hybrid system complements solar on a sunny day, solar on a cloudy day, and wind, the temperature gradient is controlled at 3.5, 2.6 and 2.6 K/cm respectively, all of which are maintained under the known limit of 10 K/cm to avoid structural failure [107]. At the same time, the temporal temperature gradient is controlled at 4.5, 2.9, and 7.4 K/hr. The power ramping requirements have varied from 15 to 60 kW/hour; while load-following the given demands, the pressure dynamics at the fuel cell inlet is maintained within 15% range from the design condition and within the compressor surge limit.

The SOFC-GT hybrid has not only demonstrated its load-following capability but more importantly achieved superb electrical efficiency even at part-load conditions. The proposed SOFC-GT hybrid system demonstrates the net electrical efficiency of 70% at its nominal condition and >50% at a part-load condition as low as 27% of the nominal load. Comparing the performance

of the hybrid system to that of a conventional combustion-based power generation unit of the same scale, the 100kW-200kW micro turbines demonstrate electrical efficiency between 30% and 33% at their nominal conditions [108], [109]. On top of the high efficiency, because the hybrid system generates most of its power output through electrochemical reactions within the solid-oxide fuel cell, greenhouse gas and particulate emissions are significantly decreased. For a microturbine of the same power scale (100-200 kW), the carbon dioxide emissions factor lies between 705 and 631.8 kg/MWh [110]. The carbon dioxide emissions factor of the proposed hybrid system is approximately 60% lower than that of the microturbine; it is calculated to be 279.6 kg/MWh at its nominal condition when operating with natural gas.

11.5.3 Hot start-up and shut-down

To integrate non-dispatchable renewable resources into the electric grid, the load-following power plants need to operate more dynamically [7]. This would lead into more frequent shut-downs and start-ups of the load-following plants depending on availabilities of the renewable resources. The start-up procedure of the load-following power plant is typically classified into three different classes based on length of time that a power plant stands still before it starts up: hot (up to 8 hours), warm (between 9 and 48 hours), and cold (between 49 and 120 hours) start-ups [111]. For a load-follower in the microgrid complementing single renewable generator, the power plant would encounter the hot shut-down and start-up procedure most frequently as the standstill time could range from 0.5 hour to 10 hours depending on the type of renewable generator in the microgrid. To physically simulate the hot start-up and shut-down processes, the SOFC-GT hybrid system model simulates a demand profile of 100-80-60-40-15-10-5-1-20-100% in a 48-hour timeframe.

The hot shut-down state of the hybrid system is defined as 1% loading condition in which the fuel cell stack generates approximately 1% of its nominal power while operating temperatures of all the system components are maintained above their operational constraints. Figure 41 and Figure 42 demonstrate the power demand and simulated profiles and the current density and voltage of the fuel cell for the same simulation respectively.

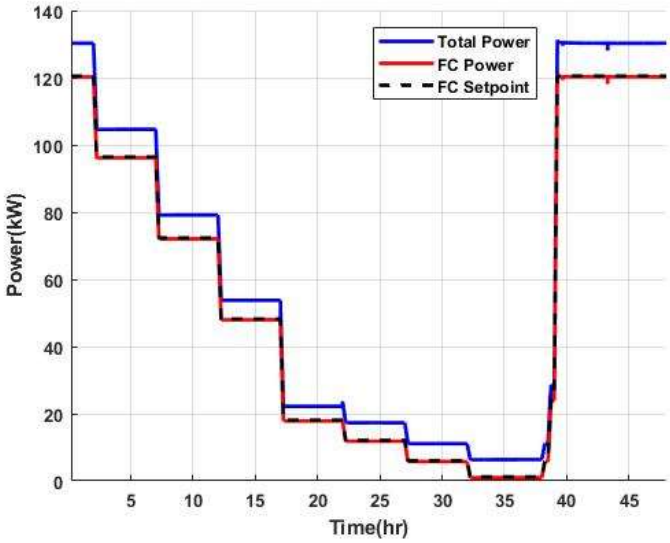

FIGURE 41: SOFC-GT HYBRID SYSTEM POWER DEMAND AND SIMULATED PROFILES

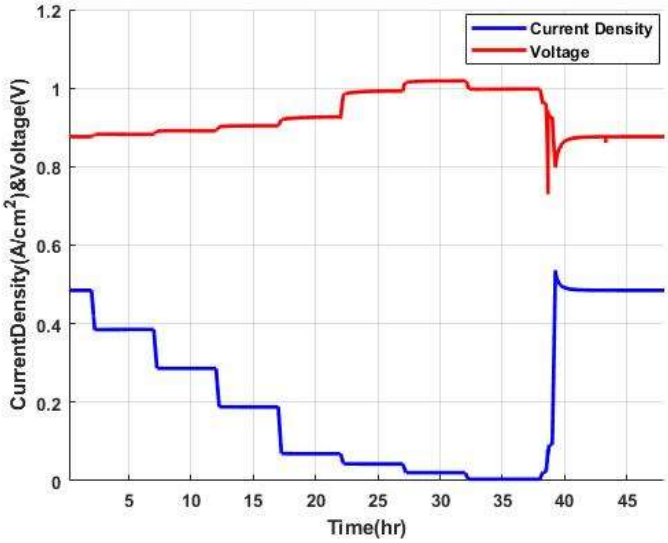

FIGURE 42: CURRENT DENSITY, VOLTAGE, AND VARIOUS SYSTEM PARAMETERS

When the system is hot-shut-down at 1% loading condition, the system generates total power of 6.35 kW: the fuel cell stack generates 0.95 kW at current density of 0.004 $\frac{A}{cm^2}$ and voltage of 0.84 V while the gas turbine generates 5.4 kW. To minimize the system power generation while to maintain the operating temperatures within the operational limits, the two modes of the controller discussed previously are employed. From 100% to 15% of the loading, the control loops 1-6 are active; from 15% to 1% of the loading, the control loops 1-2 become inactive and only the control loops 3-7 become active. From 100% to 15% of the loading conditions, two major heat sources are electrochemical reactions in the fuel cell and combustion of excess fuel for turbine inlet temperature control. However, when the fuel cell power is decreased below 15% of its nominal setting, the heat generated from the electrochemical reactions decreases significantly that the combustion of excess fuel becomes the only source of heat to maintain the entire temperature within the operational limits. Therefore, the cathode outlet temperature does not need to be controlled that the cascade loop (loop #1 and 2) is shut off. At the same time, the cathode inlet temperature is maintained (via loop #3) at the design condition to ensure that the fuel cell does not experience any extreme thermal stress incidents. Figure 43 and Figure 44 demonstrate the profiles of flow temperature at inlets and outlets of the cathode and anode on the right to better explain the rationale behind the changes in active control loops.

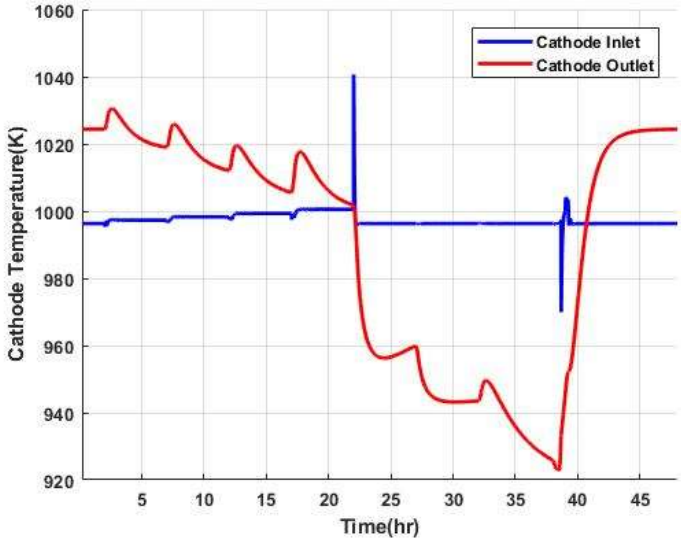

FIGURE 43: FLOW TEMPERATURE PROFILES OF CATHODE AT INLET AND OUTLET

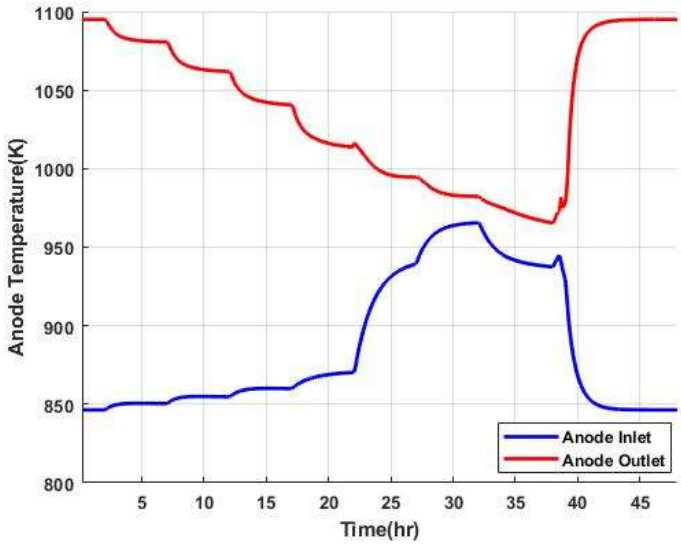

FIGURE 44: FLOW TEMPERATURE PROFILES OF ANODE AT INLET AND OUTLET

As shown in Figure 43, the temperature gradient across the cathode decreases from 28.1 K to 1K. The decreased exothermicity of the fuel cell coincides with the decrease in temperature gradient across the anode, representing that the decreased exothermicity is due to the less electrochemical reactions within the fuel cell. From 15% down, the cathode inlet temperature target is maintained

at 997.1 K while the cathode experiences the negative temperature gradient across, insinuating that endothermic operation of the fuel cell. However, the fuel cell is not operating endothermically because the anode flow temperature slightly increases even for the operation below 15%. Thus, in this case, the negative temperature gradient across the cathode suggests that because there is not enough heat generated from the electrochemical reactions, the thermal energy from the cathode flow is used to heat up the stack during the shutdown and start-up process.

Furthermore, the change in fuel cell operation and its consequences are well-reflected on the temperature profiles at other points in the system. Figure 45 demonstrates temperature profiles at various points in the system including compressor outlet, recuperator outlet, oxidizer outlet and turbine inlet and outlet. The most conspicuous physical phenomenon is the sharp increases in turbine inlet and outlet temperature profiles coinciding with the shutdown-and-start-up controller becoming active. When the controller becomes active, the fuel flow rate is maintained at the 15% level.

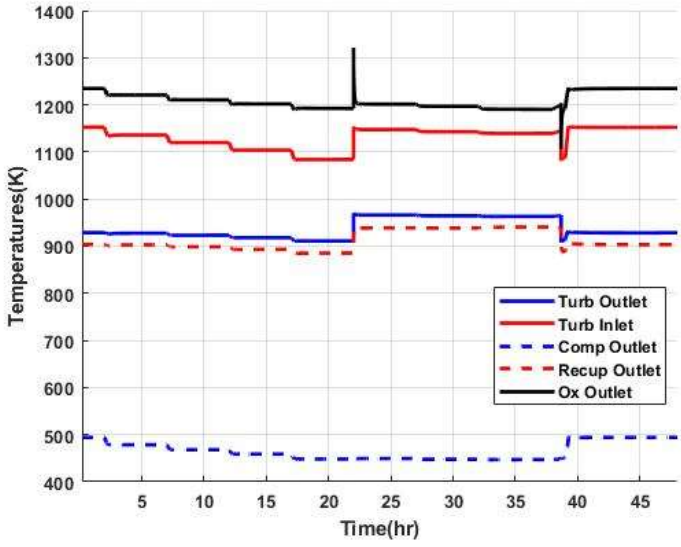

FIGURE 45: TEMPERATURE PROFILES AT VARIOUS POINTS OF THE HYBRID SYSTEM

The sharp increase in the temperature profiles starting 15% loading condition is because of the two factors. First, more fuel is available to be oxidized after the fuel cell. As the system is shutting down (lowering its power output below 15% of the nominal), less fuel is used in the fuel cell for power generation while the fuel flow rate is intentionally maintained at the 15% level. The combustion of more fuel contributes to higher oxidizer and turbine temperatures. Second, excess fuel flow rate increases significantly. Below 15% of the loading condition for the shut-down process, significantly less amount of heat is generated within the fuel cell stack that the excess fuel flow rate becomes the major source of heat input. To keep the entire system ready for instant ramping-up when needed, the turbine inlet temperature has to be maintained above 1140K and this turbine inlet temperature is obtained with supplying more excess fuel flow to the oxidizer.

11.6 Fuel Transition into Hydrogen-rich Fuel

The high operating temperature of the SOFC allows the system operation with a wide range of fuel from natural gas to pure hydrogen. Its fuel flexibility will enable the SOFC systems to play a significant role in the transition from fossil-fuel to renewable fuel. This section demonstrates the SOFC-GT system steady-state simulation results with fuel of varying content of hydrogen. Changing the composition of fuel affects reforming and oxidization reactions throughout the hybrid system and poses unique flow and thermal management challenges. Figure 46 shows the change in the nominal operating point on turbomachinery performance maps with varying content of hydrogen in the fuel.

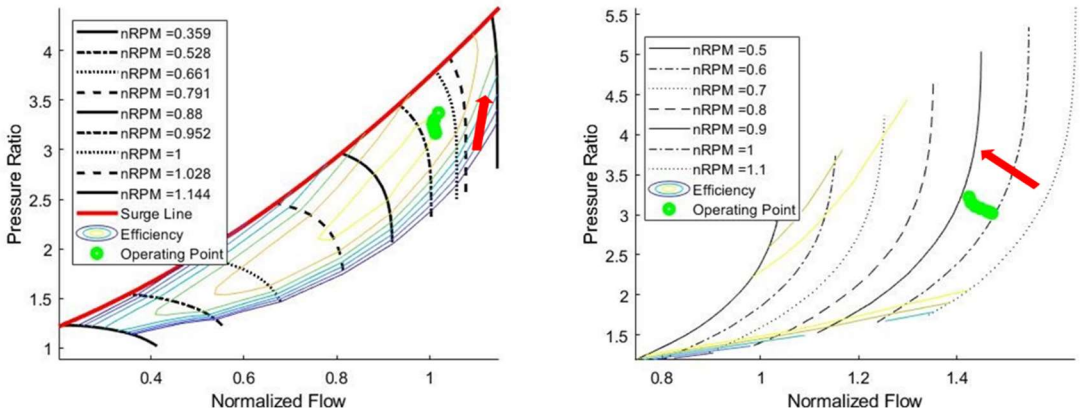

FIGURE 46: CHANGES IN AN OPERATION POINT SHOWN ON TURBOMACHINERY PERFORMANCE MAPS WITH INCREASING HYDROGEN (LEFT: COMPRESSOR, RIGHT: TURBINE)

The movement of the operation point within the compressor and turbine maps demonstrates that increasing hydrogen content in the fuel results in increase of the flow pressure and decrease of the normalized flow. These changes move the operation point closer towards the compressor surge line but not close enough to cause compressor surge. The analysis of the turbomachinery maps only cannot define the flow and thermal management challenges that increasing content of hydrogen would bring about in the hybrid system. Table 10 demonstrates the hybrid system characteristics with varying content of hydrogen when the fuel utilization ratio is not manipulated.

TABLE 10: HYBRID SYSTEM CHARACTERISTICS WITH VARYING CONTENT OF HYDROGEN WITHOUT FU MANIPULATION

Hydrogen Content	System Characteristics						
	$T_{in,cath}$ (K)	$T_{out,cath}$ (K)	$TIT(K)$	$PR_{@Turb}$	P_{GT} (kW)	η_{elec} (%)	FU (%)
NG	997.1	1025.2	1154.3	3.02	9.78	71.73	82
10 %	997.1	1031.8	1170.4	3.03	10.47	71.68	82
20 %	997.1	1039.7	1189.7	3.05	11.28	71.62	82
40 %	997.1	1049.3	1213.1	3.06	12.27	71.56	82
50 %	1041.2	1114.7	1267.8	3.11	14.99	71.07	82
60 %	1059.0	1151.5	1317.6	3.15	17.18	70.71	82
70 %	1071.9	1189.4	1368.7	3.22	19.73	70.07	82

In general, increasing hydrogen content decreases the internal reforming reaction within the fuel cell and thus, increases temperatures of the flows downstream of the fuel cell; consequently, the gas turbine power output has increased. Up until 40% hydrogen, the cathode inlet temperature can be controlled with manipulating the bypass valve position and the gas turbine power output stays within the design power output of 12kW. Above 40%, the cathode inlet temperature can no longer be controlled with just manipulating the bypass valve position (the valve is completely open). Other system parameters such as fuel utilization ratio have to be manipulated to 1) control the cathode inlet temperature at the design condition of 997.1 K, 2) maintain temperatures downstream of the fuel cell within the operational limits, and 3) prevent the gas turbine output from overshooting above the design condition of 12 kW. In response, the fuel utilization ratio is further manipulated to allow the hybrid system and its controller to operate with more than 40% hydrogen in its fuel. Figure 47 demonstrates changes in net electrical efficiency and emissions factor when the hydrogen content of the fuel is varied along with fuel utilization manipulation.

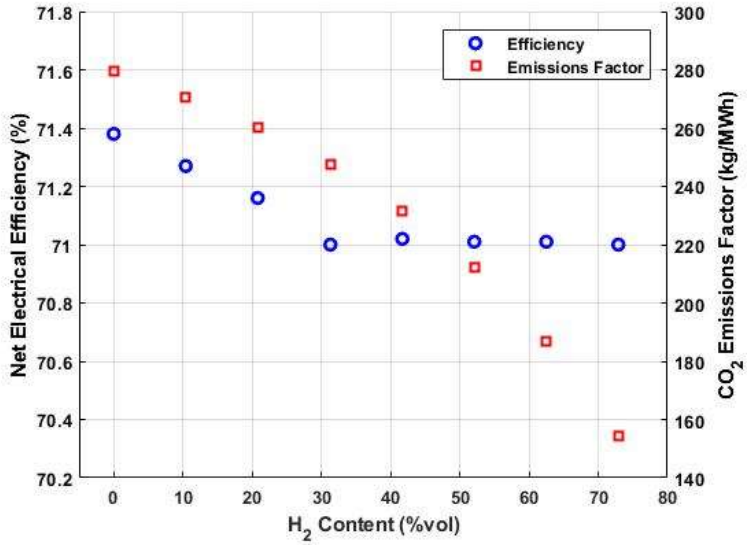

Figure 47: Net electrical efficiency and emissions factor with varying hydrogen content

This specific gas turbine hybrid system is originally designed to operate with natural gas (93% methane) at the net electrical efficiency of 71.38%. With increasing hydrogen content in the inlet fuel, the emissions factor decreases significantly from about 280 kg MWh^{-1} to 155 kg MWh^{-1}. Note that an increase of hydrogen volumetric concentration of more than 70% determines a reduction in CO_2 emissions of approximately 45%. In fact, at 72.9% hydrogen volumetric content in the fuel, only 47.1% of the mass specific primary energy supplied comes from hydrogen itself.

On the other hand, the net electrical efficiency decreases with increasing hydrogen content until about 30% hydrogen, when the global fuel utilization is maintained at the design condition of 82%. This decrease in the net electrical efficiency is related to the amount of internal reforming reaction, which decreases at higher hydrogen content, determining a more exothermic footprint of the SOFC stack. This change is better shown in Figure 48, Figure 49, and Figure 50 that respectively compares the hydrogen concentration profiles, current density profiles over the length of the stack, and temperature distribution profiles when the fuel is natural gas, 41.7%, and 72.9% hydrogen.

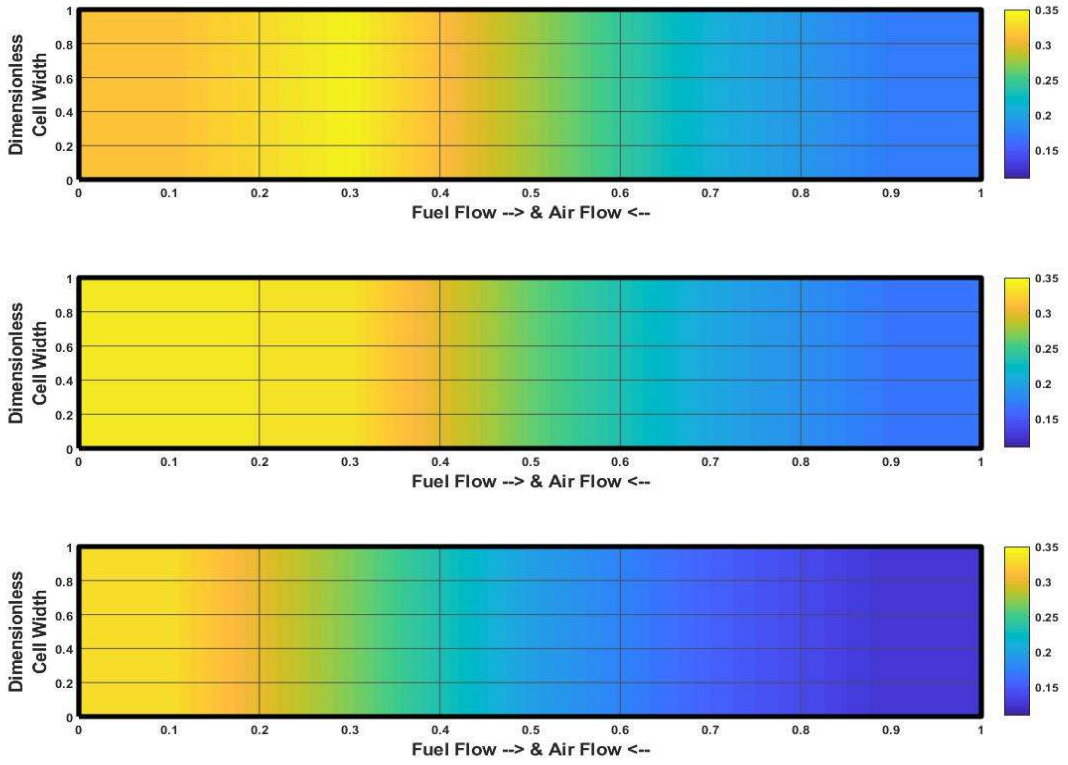

FIGURE 48: COMPARISON OF HYDROGEN CONCENTRATION PROFILE MAPS
(Top: Natural gas case, mid: 41.7% hydrogen, bottom: 72.9% hydrogen)

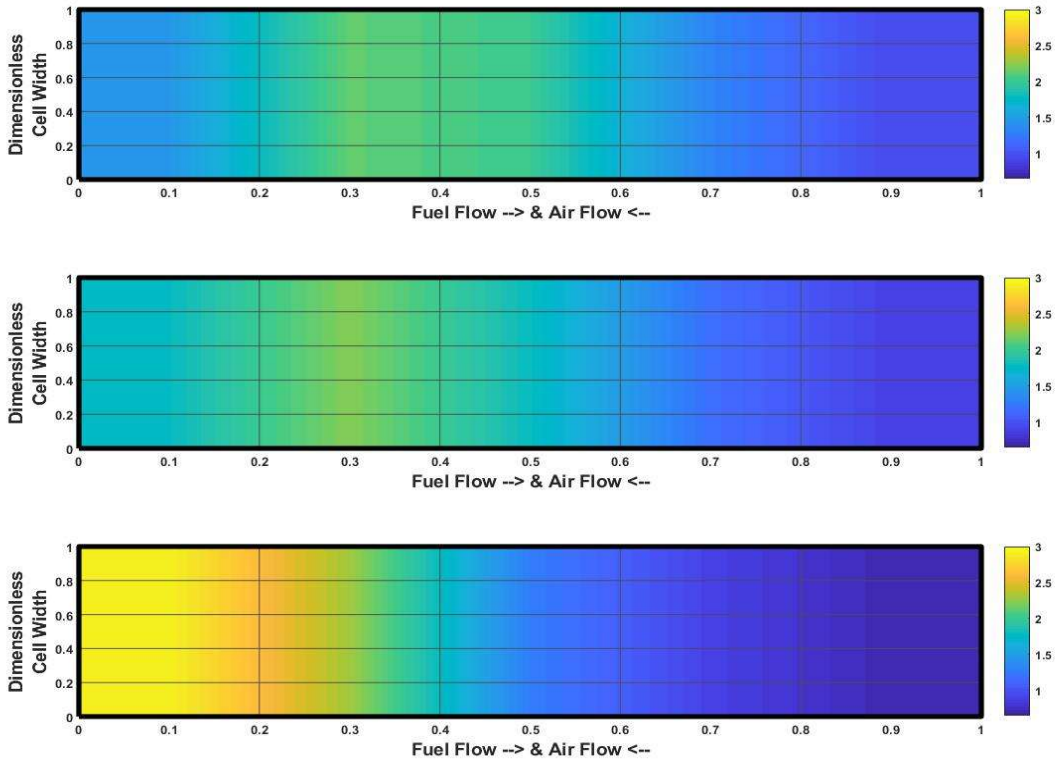

FIGURE 49: COMPARISON OF CURRENT DENSITY PROFILE MAPS

(Top: Natural gas case, mid: 41.7% hydrogen, bottom: 72.9% hydrogen)

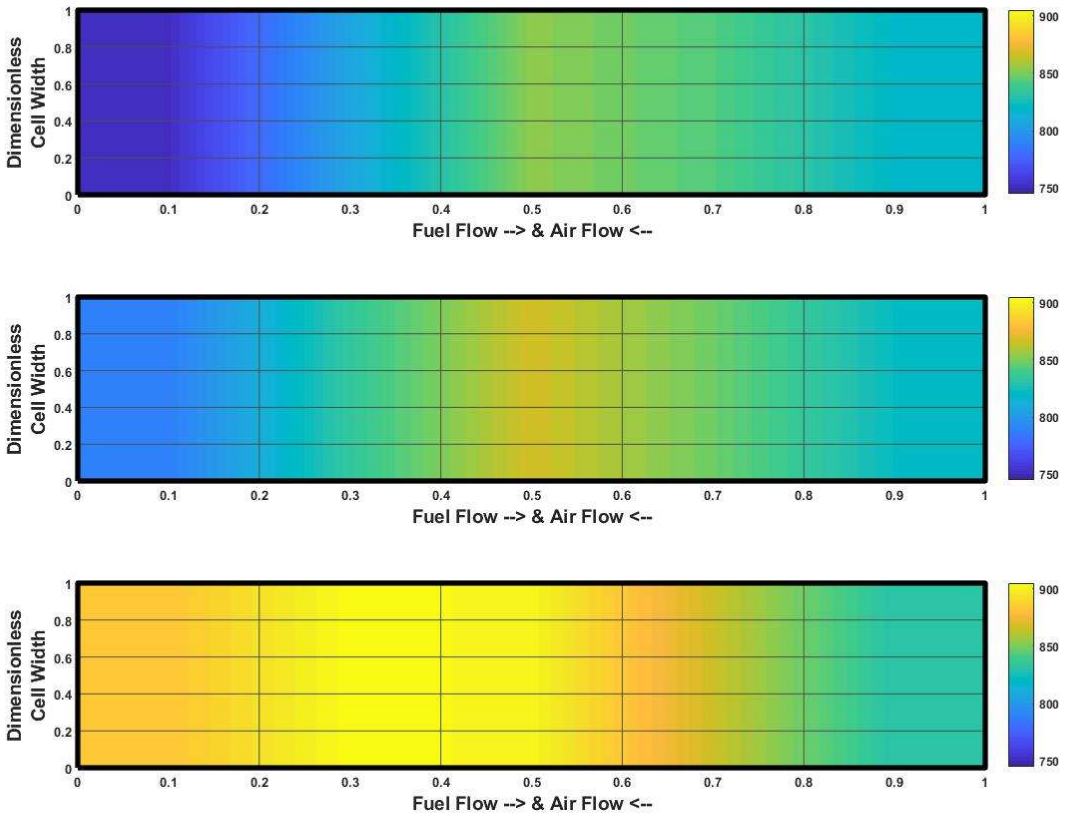

FIGURE 50: COMPARISON OF TEMPERATURE DISTRIBUTION PROFILES
(Top: Natural gas case, mid: 41.7% hydrogen, bottom: 72.9% hydrogen)

The increase in hydrogen concentration in the inlet fuel determines an increase in hydrogen concentration gradient throughout the cell channel and a shift of the peak hydrogen concentration from ~30% of the dimensionless cell channel length to the inlet of the fuel flow. The current density profiles reflect the behavior of the hydrogen concentration profiles. These changes in hydrogen and current density profile across the stack are caused by less methane content in the fuel leading to less endothermic internal reforming.

With the increase in hydrogen content of the fuel, the average stack temperature increases from 815.1 °C to 876.8 °C. In addition, the maximum temperature gradient decreases from 1.46 to 1.05 °C/% channel length . For the natural gas case, the maximum temperature gradient occurs between

0% and 50% of the dimensionless cell channel length position while for the 73% hydrogen case, the gradient occurs between 35% and 100%. The increase in the average temperature and decrease in the maximum temperature gradient are in line with the decrease in the endothermic internal reforming reaction. In the natural gas case, the temperature distribution within the stack is dictated by cooling effect of the counter-flow air flow and endothermic reactions. As the hydrogen content in the fuel is increased, amount of heat utilized by the endothermic reactions decreases that the average temperature across the fuel cell increases. Consequentially, increase in the average temperature results in the decrease in the maximum temperature gradient.

At the same time, the temperature profiles demonstrate the similar peak shifting pattern as in the hydrogen concentration and current density. As the hydrogen content increases from 0% to 41.7% and to 72.9%, the peak temperature shifts from 50% to 35% of the dimensionless cell channel length position and the peak current density shifts from 30% to 5% of the dimensionless cell channel length position. The difference in the peak locations of the current density, hydrogen concentration, and temperature comes from difference in electrochemical and thermal time scales resulting in the spatial delay of the thermal response.

The changes in the temperature dynamics within the stack lead to different system performance characteristics, posing another set of control challenges. Table 11 summarizes various system characteristics when the hydrogen content of the fuel is varied. Even with the increase in the temperature, the cathode inlet temperature can be maintained at the design condition of 997.1 K up until approximately 30% hydrogen, only by manipulating the cold air bypass valve position. When the hydrogen content in the fuel increases above 40%, the amount of heat removed through the steam-methane reforming reaction is significantly reduced that the cathode inlet temperature

cannot be maintained at the design condition only using the bypass valve by decreasing the amount of flow going into the preheater.

TABLE 11: HYBRID SYSTEM CHARACTERISTICS WITH VARYING CONTENT OF HYDROGEN

Hydrogen Content	System Characteristics							
	$T_{in,cath}\ (K)$	$T_{out,cath}\ (K)$	$TIT(K)$	$PR_{@Turb}$	$P_{GT}\ (kW)$	η_{elec} (%)	VO_{cold}	FU
NG	997.1	1025.2	1154.3	3.02	9.78	71.73	.468	82%
10 %	997.1	1031.8	1170.4	3.03	10.47	71.68	.348	82%
20 %	997.1	1039.7	1189.7	3.05	11.28	71.62	.250	82%
40 %	997.1	1049.3	1213.1	3.06	12.27	71.56	.165	82%
50 %	997.1	1087.5	1232.3	3.08	13.19	71.65	.111	84%
60 %	997.1	1118.2	1237.5	3.08	13.51	71.76	.097	86%
70 %	997.1	1155.9	1264.0	3.10	14.73	71.77	.031	88%

The system-wide solution presented in this study is to increase the global fuel utilization ratio. The increase in the fuel utilization brings about more exothermicity within the fuel cell stack. However, it decreases the overall fuel flow rate thus reducing the remaining unoxidized fuel downstream the fuel cell, contributing to lower the turbine outlet temperature. Therefore, the global fuel utilization ratio has to be manipulated at the same time to control the cathode inlet temperature along with the cold air bypass valve position for the cases with the hydrogen content higher than 40%. Figure 51 demonstrates temperature at inlet and outlet of the fuel cell and inlet of the turbine as well as the power generated by the turbine at respective temperatures.

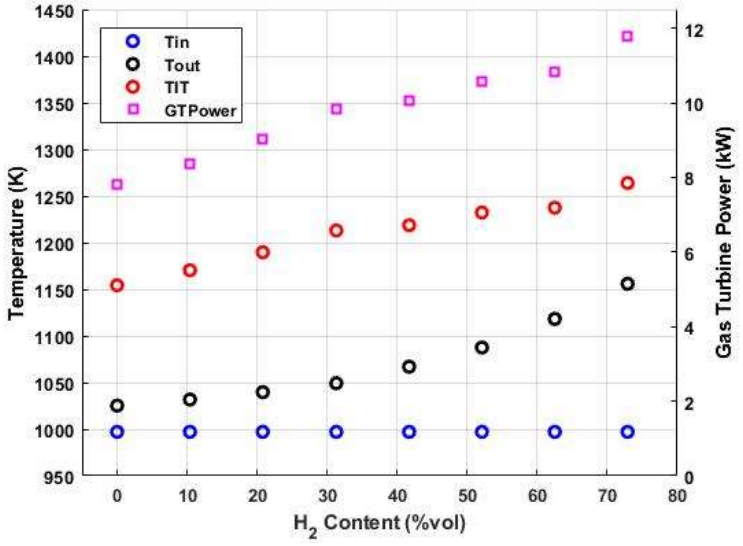

FIGURE 51: TEMPERATURES AND GAS TURBINE POWER OUTPUT WITH VARYING HYDROGEN CONTENT

In system perspectives, the electrical efficiency is slightly compromised with increasing hydrogen content while maintaining the fuel utilization ratio. Along with the increase in the fuel utilization ratio needed to maintain the cathode inlet temperature at the design condition, the electrical efficiency rises back up. On the other hand, the temperature profiles along with the gas turbine power output have increased with increasing hydrogen content. The hydrogen content in the fuel affects the amount of heat removed through steam-methane reforming reaction within the fuel cell, thereby increasing the cathode outlet temperature as well as the turbine inlet temperature and gas turbine power downstream.

The current SOFC-GT system can accommodate up to 72.9 % hydrogen in its fuel without any modification in the system configuration and control scheme. The system components such as heat exchangers and turbomachinery in the current configuration may need minor modifications in order to accommodate more than 72.9 % hydrogen and to tolerate the consequential increase in

the operating temperature. However, the fact that the system can tolerate such a high level of hydrogen proves the fuel flexibility of the SOFC systems. More importantly, this result demonstrates that the SOFC-GT hybrid system can pivotally contribute to transition from fossil fuel-power grids to renewable grids for the system's demonstrated dispatchability and fuel flexibility.

12. Summary & Conclusions

This dissertation has identified the challenges associated with operation of load-followers in the current and future grid with high renewable penetration, proposed fleet and grid-wide solutions to resolve the challenges, and further analyzed implications of climate change and of future load-following technology on future grid operation. For the current grid, the NGCC technology has been analyzed as a load-following option during the energy transition in which renewable power generation systems such as hydrogen turbines and fuel cells replace the NGCC technology. Furthermore, the analysis has been extended to operation of the load-followers under grid mix scenarios when the climate change affects renewable resource availabilities. By simultaneously accounting for power plant fleet and grid dynamics within various grid mix scenarios, this work has demonstrated the enhanced significance of load-following plants for maintaining grid reliability while pursing progressive environmental targets for the state of California.

As the era of the NGCC technology may have to come to an end for accomplishing either zero-emissions or 100% renewable goal for the electricity sector, the SOFC-GT technology has been analyzed as a future load-following option in the grid. With the grids having higher renewable penetration and becoming more vulnerable to intermittency of the renewable availabilities

exacerbated by climate change, dynamic dispatchability will only become more significant. In this context, the dynamic potential of the SOFC-GT technology as a future load-follower has been fully evaluated by physically simulating all modes of operation, especially start-up, shut-down, and lower part-load operation. Integrating two systems with different operating principles (fuel cell-electrochemistry and turbine-combustion) has demonstrated a significant efficiency boost but at the same time required proper design and control of the hybrid system. In this study, a decentralized control strategy has been developed to 1) enable significant load-following and transient operation and 2) maintain physical constraints on fuel cell thermal gradients and turbine surge margin. Hybridizing fuel cell and gas turbine technology will be a step forward to 100% renewable grid with its ultra-high efficiency, ultra-low-emission, and dispatchable power generation capability.

The major conclusions of the current research are as follows:

- The part-load efficiency of natural gas combined cycle power plants can be improved by up to 13.5% by introducing variable inlet guide vanes and by up to 28.4% by introducing variable speed operation to improve their overall efficiency to complement renewable dynamics.
- An NGCC fleet dispatch strategy in which most plants are operated as on-off plants and only a few plants operate dynamically is found to reduce emissions of GHG by up to 54%.
- Under climate change impacts, expected to complicate dynamics of renewable generation, thereby increasing grid wide GHG emissions, the NGCC fleet dispatch strategy is found to reduce emissions of GHG by up to 49%.

- The proposed solid oxide fuel cell-gas turbine hybrid system achieves net electrical efficiency of over 70% even for distributed energy resources application (71.4% at 130 kW in this dissertation).
- The SOFC-GT hybrid system can complement high levels of renewable penetration without thermally stressing the fuel cell by maintaining the spatial thermal gradient across the fuel cell stack under 7.4K/cm.
- The SOFC-GT hybrid system can operate with fuel up to 72.9% hydrogen by volume without any system and control modifications.
- The SOFC-GT hybrid systems have potential to displace NGCCs as load-following plants in future electric grids featuring their high efficiency, dynamic dispatchability, and fuel flexibility.

13. References

[1] Agency IE. Global Energy Review 2021 2021.

[2] Liu Y, Chen Y. Impact of population growth and land-use change on water resources and ecosystems of the arid Tarim River Basin in Western China. Int J Sustain Dev World Ecol 2006;13:295–305. https://doi.org/10.1080/13504500609469681.

[3] Zhou E. U . S . Renewable Energy Policy and Industry Presentation at CNREC U . S . Renewable Energy Policy and Industry Federal and State Drivers for RE Solar Update Wind Update Biofuel Update . 2015.

[4] TITLE XVII | Department of Energy n.d. https://www.energy.gov/lpo/title-xvii (accessed February 14, 2022).

[5] California SOF, Material EL. Senate Bill No. 100. 2018.

[6] Christopher W. Lim. UC Irvine UC Irvine Electronic Theses and Dissertations UNIVERSITY ! OF ! CALIFORNIA , ! 2015:1982–2004.

[7] Balling L. Flexible future for combined cycle. Mod Power Syst 2010.

[8] Mclarty D, Brouwer J, Samuelsen S. Fuel cell e gas turbine hybrid system design part I : Steady state performance. J Power Sources 2014;257:412–20. https://doi.org/10.1016/j.jpowsour.2013.11.122.

[9] Mclarty D, Brouwer J, Samuelsen S. Fuel cell e gas turbine hybrid system design part II : Dynamics and control. J Power Sources 2014;254:126–36. https://doi.org/10.1016/j.jpowsour.2013.11.123.

[10] Guo Z, Ai N, Polenske KR. Evaluating environmental and economic benefits of yellow dust storm-related policies in north China. Int J Sustain Dev World Ecol 2008;15:457–70.

https://doi.org/10.3843/SusDev.15.5:7.

[11] Miri A, Ahmadi H, Ekhtesasi MR, Panjehkeh N, Ghanbari A. Environmental and socio-economic impacts of dust storms in Sistan Region, Iran. Int J Environ Stud 2009;66:343–55. https://doi.org/10.1080/00207230902720170.

[12] Clark CE, Barker A, King J, Clark CE, Barker A, King J. Wind and Solar Hybrid Power Plants for Energy Resilience Wind and Solar Hybrid Power Plants for Energy Resilience 2022.

[13] IRENA. Renewable power generation costs in 2019 - Key findings. Int Renew Energy Agency 2020:160.

[14] Zhai P, Larsen P, Millstein D, Menon S, Masanet E. The potential for avoided emissions from photovoltaic electricity in the United States. Energy 2012;47:443–50. https://doi.org/10.1016/j.energy.2012.08.025.

[15] Bukhary S, Ahmad S, Batista J. Analyzing land and water requirements for solar deployment in the Southwestern United States. Renew Sustain Energy Rev 2018;82:3288–305. https://doi.org/10.1016/j.rser.2017.10.016.

[16] Gagnon P, Margolis R, Melius J, Phillips C, Elmore R. Peak heat flux and temperature difference. Nrel 2016:82.

[17] Wiser, Millstein D, Mai T, Macknick J, Carpenter A, Cohen S, et al. The environmental and public health benefits of achieving high penetrations of solar energy in the United States. Energy 2016;113:472–86. https://doi.org/10.1016/j.energy.2016.07.068.

[18] Wiser R, Barbose G, Holt E. Supporting solar power renewables portfolio standards: Experience from the United States. Sol Power, Renew Portf Stand Sol Renew Energy Certif 2012:1–53.

[19] Work R. An Empirical Analysis of Project Cost , Performance , and Pricing Trends in the United States Authors : Mark Bolinger , Joachim Seel , Kristina Hamachi LaCommare 2014.

[20] Bolinger M, Seel J. Utility-Scale Solar: Empirical trends in project technology, cost, performance, and PPA pricing in the United States. Lawrence Berkeley Natl Lab 2018:62.

[21] Molina MG, Espejo EJ. Modeling and simulation of grid-connected photovoltaic energy conversion systems. Int J Hydrogen Energy 2014;39:8702–7. https://doi.org/10.1016/j.ijhydene.2013.12.048.

[22] McTigue JD, Castro J, Mungas G, Kramer N, King J, Turchi C, et al. Hybridizing a geothermal power plant with concentrating solar power and thermal storage to increase power generation and dispatchability. Appl Energy 2018;228:1837–52. https://doi.org/10.1016/j.apenergy.2018.07.064.

[23] Zhu Q, Li Q, Zhang B, Wang L, Li G, Wang R. Capacity optimization for electrical and thermal energy storage in multi-energy building energy system. Energy Procedia 2019;158:6425–30. https://doi.org/10.1016/j.egypro.2019.01.183.

[24] González A, Riba JR, Rius A, Puig R. Optimal sizing of a hybrid grid-connected photovoltaic and wind power system. Appl Energy 2015;154:752–62. https://doi.org/10.1016/j.apenergy.2015.04.105.

[25] Sun K, Li KJ, Pan J, Liu Y, Liu Y. An optimal combined operation scheme for pumped storage and hybrid wind-photovoltaic complementary power generation system. Appl Energy 2019;242:1155–63. https://doi.org/10.1016/j.apenergy.2019.03.171.

[26] Maton JP, Zhao L, Brouwer J. Dynamic modeling of compressed gas energy storage to complement renewable wind power intermittency. Int J Hydrogen Energy 2013;38:7867–

80. https://doi.org/10.1016/j.ijhydene.2013.04.030.

[27] Valverde-Isorna L, Ali D, Hogg D, Abdel-Wahab M. Modelling the performance of wind-hydrogen energy systems: Case study the Hydrogen Office in Scotland/UK. Renew Sustain Energy Rev 2016;53:1313–32. https://doi.org/10.1016/j.rser.2015.08.044.

[28] Prăvălie R, Patriche C, Bandoc G. Spatial assessment of solar energy potential at global scale. A geographical approach. J Clean Prod 2019;209:692–721. https://doi.org/10.1016/j.jclepro.2018.10.239.

[29] Niblick B, Landis AE. Assessing renewable energy potential on United States marginal and contaminated sites. Renew Sustain Energy Rev 2016;60:489–97. https://doi.org/10.1016/j.rser.2015.12.045.

[30] Feng C, Sun M, Cui M, Chartan EK, Hodge BM, Zhang J. Characterizing forecastability of wind sites in the United States. Renew Energy 2019;133:1352–65. https://doi.org/10.1016/j.renene.2018.08.085.

[31] He G, Kammen DM. Where, when and how much wind is available? A provincial-scale wind resource assessment for China. Energy Policy 2014;74:116–22. https://doi.org/10.1016/j.enpol.2014.07.003.

[32] He G, Kammen DM. Where, when and how much solar is available? A provincial-scale solar resource assessment for China. Renew Energy 2016;85:74–82. https://doi.org/10.1016/j.renene.2015.06.027.

[33] Tarroja B, AghaKouchak A, Samuelsen S. Quantifying climate change impacts on hydropower generation and implications on electric grid greenhouse gas emissions and operation. Energy 2016;111:295–305. https://doi.org/10.1016/j.energy.2016.05.131.

[34] Tarroja B, Chiang F, AghaKouchak A, Samuelsen S. Assessing future water resource

constraints on thermally based renewable energy resources in California. Appl Energy 2018;226:49–60. https://doi.org/10.1016/j.apenergy.2018.05.105.

[35] Hunter CA, Michael M, Reznicek EP, Rustagi N, Baldwin F, Baldwin SF. Article Techno-economic analysis of long-duration energy storage and flexible power generation technologies to support high-variable renewable energy grids storage and flexible power generation technologies to support high-variable renewable energy grids. Joule 2021;5:2077–101. https://doi.org/10.1016/j.joule.2021.06.018.

[36] Rohde D, Knudsen BR, Andresen T, Nord N. Dynamic optimization of control setpoints for an integrated heating and cooling system with thermal energy storages. Energy 2020;193:116771. https://doi.org/10.1016/j.energy.2019.116771.

[37] Lund R, Mathiesen BV. Large combined heat and power plants in sustainable energy systems. Appl Energy 2015;142:389–95. https://doi.org/10.1016/j.apenergy.2015.01.013.

[38] Bloess A. Modeling of combined heat and power generation in the context of increasing renewable energy penetration. Appl Energy 2020;267:114727. https://doi.org/10.1016/j.apenergy.2020.114727.

[39] Brouwer AS, van den Broek M, Seebregts A, Faaij A. Operational flexibility and economics of power plants in future low-carbon power systems. Appl Energy 2015;156:107–28. https://doi.org/10.1016/j.apenergy.2015.06.065.

[40] Beiron J, Montañés RM, Normann F, Johnsson F. Flexible operation of a combined cycle cogeneration plant – A techno-economic assessment. Appl Energy 2020;278. https://doi.org/10.1016/j.apenergy.2020.115630.

[41] Yu H, Nord LO, Yu C, Zhou J, Si F. An improved combined heat and power economic dispatch model for natural gas combined cycle power plants. Appl Therm Eng

2020;181:115939. https://doi.org/10.1016/j.applthermaleng.2020.115939.

[42] Keatley P, Shibli A, Hewitt NJ. Estimating power plant start costs in cyclic operation. Appl Energy 2013;111:550–7. https://doi.org/10.1016/j.apenergy.2013.05.033.

[43] Liu Z, Karimi IA. Simulation of a combined cycle gas turbine power plant in Aspen HYSYS. Energy Procedia 2019;158:3620–5. https://doi.org/10.1016/j.egypro.2019.01.901.

[44] Wang Y, Bhattacharyya D, Turton R. Dynamic Modeling And Control Of A Natural Gas Combined Cycle Power Plant For Load-Following Operation. vol. 47. Elsevier Masson SAS; 2019. https://doi.org/10.1016/B978-0-12-818597-1.50017-5.

[45] Alobaid F, Postler R, Ströhle J, Epple B, Kim HG. Modeling and investigation start-up procedures of a combined cycle power plant. Appl Energy 2008;85:1173–89. https://doi.org/10.1016/j.apenergy.2008.03.003.

[46] Alobaid F, Starkloff R, Pfeiffer S, Karner K, Epple B, Kim HG. A comparative study of different dynamic process simulation codes for combined cycle power plants-Part A: Part loads and off-design operation. Fuel 2015;153:692–706. https://doi.org/10.1016/j.fuel.2015.02.010.

[47] Alobaid F, Starkloff R, Pfeiffer S, Karner K, Epple B, Kim HG. A comparative study of different dynamic process simulation codes for combined cycle power plants-Part B: Start-up procedure. Fuel 2015;153:707–16. https://doi.org/10.1016/j.fuel.2015.02.011.

[48] Bany Ata A, Alobaid F, Heinze C, Almoslh A, Sanfeliu A, Epple B. Comparison and validation of three process simulation programs during warm start-up procedure of a combined cycle power plant. Energy Convers Manag 2020;207:112547. https://doi.org/10.1016/j.enconman.2020.112547.

[49] Haji Haji V, Fekih A, Monje CA, Fakhri Asfestani R. Adaptive model predictive control design for the speed and temperature control of a V94.2 gas turbine unit in a combined cycle power plant. Energy 2020;207. https://doi.org/10.1016/j.energy.2020.118259.

[50] Rúa J, Nord LO. Optimal control of flexible natural gas combined cycles with stress monitoring: Linear vs nonlinear model predictive control. Appl Energy 2020;265:114820. https://doi.org/10.1016/j.apenergy.2020.114820.

[51] Huang X, Luo X, Chen J, Yang Z, Chen Y, María Ponce-Ortega J, et al. Synthesis and dual-objective optimization of industrial combined heat and power plants compromising the water-energy nexus. Appl Energy 2018;224:448–68. https://doi.org/10.1016/j.apenergy.2018.04.095.

[52] Ticâ A, Guéguen H, Dumur D, Faille D, Davelaar F. Design of a combined cycle power plant model for optimization. Appl Energy 2012;98:256–65. https://doi.org/10.1016/j.apenergy.2012.03.032.

[53] Variny M, Mierka O. Improvement of part load efficiency of a combined cycle power plant provisioning ancillary services. Appl Energy 2009;86:888–94. https://doi.org/10.1016/j.apenergy.2008.11.004.

[54] Sunil PU, Barve J, Nataraj PSV. Boiler model and simulation for control design and validation. vol. 3. IFAC; 2014. https://doi.org/10.3182/20140313-3-IN-3024.00132.

[55] Manassaldi JI, Mussati MC, Scenna NJ, Mussati SF. Optimization of triple-pressure combined-cycle power plants by generalized disjunctive programming and extrinsic functions. Comput Chem Eng 2021;146:107190. https://doi.org/10.1016/j.compchemeng.2020.107190.

[56] Polyzakis AL, Koroneos C, Xydis G. Optimum gas turbine cycle for combined cycle

power plant. Energy Convers Manag 2008;49:551–63. https://doi.org/10.1016/j.enconman.2007.08.002.

[57] Bassily AM. Enhancing the efficiency and power of the triple-pressure reheat combined cycle by means of gas reheat, gas recuperation, and reduction of the irreversibility in the heat recovery steam generator. Appl Energy 2008;85:1141–62. https://doi.org/10.1016/j.apenergy.2008.02.017.

[58] Pinelli M, Bucci G. Numerical based design of exhaust gas system in a cogeneration power plant. Appl Energy 2009;86:857–66. https://doi.org/10.1016/j.apenergy.2008.08.016.

[59] Kim T., Park H., Ro S. Characteristics of transient operation of a dual-pressure bottoming system for the combined cycle power plant. Energy 2001;26:905–18. https://doi.org/10.1016/S0360-5442(01)00039-1.

[60] Kim TS, Lee DK, Ro ST. Dynamic behaviour analysis of a heat recovery steam generator during start-up. Int J Energy Res 2000;24:137–49. https://doi.org/10.1002/(SICI)1099-114X(200002)24:2<137::AID-ER568>3.0.CO;2-0.

[61] Benato A, Stoppato A, Bracco S. Combined cycle power plants: A comparison between two different dynamic models to evaluate transient behaviour and residual life. Energy Convers Manag 2014;87:1269–80. https://doi.org/10.1016/j.enconman.2014.06.017.

[62] Sunil PU, Barve J, Nataraj PS V. Mathematical modeling, simulation and validation of a boiler drum: Some investigations. Energy 2017;126:312–25. https://doi.org/10.1016/j.energy.2017.02.140.

[63] Neshumayev D, Rummel L, Konist A, Ots A, Parve T. Power plant fuel consumption rate during load cycling. Appl Energy 2018;224:124–35.

https://doi.org/10.1016/j.apenergy.2018.04.063.

[64] Rossi I, Sorce A, Traverso A. Gas turbine combined cycle start-up and stress evaluation: A simplified dynamic approach. Appl Energy 2017;190:880–90. https://doi.org/10.1016/j.apenergy.2016.12.141.

[65] Brouwer J. Hybrid Gas Turbine Fuel Cell Systems. In: Dennis RA, editor. Gas Turbine Handb., Morgantown, West Virginia: U.S Department of Energy, DOE/NETL-2006/1230; 2006.

[66] McLarty D, Brouwer J, Samuelsen S. Fuel cell-gas turbine hybrid system design part I: Steady state performance. J Power Sources 2014;257:412–20. https://doi.org/10.1016/j.jpowsour.2013.11.122.

[67] McLarty D. UNIVERSITY OF CALIFORNIA , Thermodynamic Modeling and Dispatch of Distributed Energy Technologies including Fuel Cell – Gas Turbine Hybrids DISSERTATION submitted in partial satisfaction of the requirements for the degree of Doctor of Philosophy in Mechan 2013.

[68] Yang WJ, Park SK, Kim TS, Kim JH, Sohn JL, Ro ST. Design performance analysis of pressurized solid oxide fuel cell / gas turbine hybrid systems considering temperature constraints 2006;160:462–73. https://doi.org/10.1016/j.jpowsour.2006.01.018.

[69] Arsalis A. Thermoeconomic modeling and parametric study of hybrid SOFC – gas turbine – steam turbine power plants ranging from 1 . 5 to 10 MWe 2008;181:313–26. https://doi.org/10.1016/j.jpowsour.2007.11.104.

[70] Tarroja B, Mueller F, Maclay J, Brouwer J. Parametric thermodynamic analysis of a solid oxide fuel cell gas turbine system design space. J Eng Gas Turbines Power 2010;132:1–11. https://doi.org/10.1115/1.4000263.

[71] Cheddie DF, Murray R. Thermo-economic modeling of an indirectly coupled solid oxide fuel cell/gas turbine hybrid power plant. J Power Sources 2010;195:8134–40. https://doi.org/10.1016/j.jpowsour.2010.07.012.

[72] Santin M, Traverso A, Magistri L, Massardo A. Thermoeconomic analysis of SOFC-GT hybrid systems fed by liquid fuels. Energy 2010;35:1077–83. https://doi.org/10.1016/j.energy.2009.06.012.

[73] Wang J, Yan Z, Ma S, Dai Y. Thermodynamic analysis of an integrated power generation system driven by solid oxide fuel cell. Int J Hydrogen Energy 2012;37:2535–45. https://doi.org/10.1016/j.ijhydene.2011.10.079.

[74] Zabihian F, Fung AS. Thermodynamic sensitivity analysis of hybrid system based on solid oxide fuel cell. Sustain Energy Technol Assessments 2014;6:51–9. https://doi.org/10.1016/j.seta.2013.12.004.

[75] Reyhani HA, Meratizaman M, Ebrahimi A, Pourali O, Amidpour M. Thermodynamic and economic optimization of SOFC-GT and its cogeneration opportunities using generated syngas from heavy fuel oil gasification. Energy 2016;107:141–64. https://doi.org/10.1016/j.energy.2016.04.010.

[76] Eisavi B, Chitsaz A, Hosseinpour J, Ranjbar F. Thermo-environmental and economic comparison of three different arrangements of solid oxide fuel cell-gas turbine (SOFC-GT) hybrid systems. Energy Convers Manag 2018;168:343–56. https://doi.org/10.1016/j.enconman.2018.04.088.

[77] Pirkandi J, Mahmoodi M, Ommian M. An optimal configuration for a solid oxide fuel cell-gas turbine (SOFC-GT) hybrid system based on thermo-economic modelling. J Clean Prod 2017;144:375–86. https://doi.org/10.1016/j.jclepro.2017.01.019.

[78] Sghaier SF, Khir T, Ben Brahim A. Energetic and exergetic parametric study of a SOFC-GT hybrid power plant. Int J Hydrogen Energy 2018;43:3542–54. https://doi.org/10.1016/j.ijhydene.2017.08.216.

[79] Pirkandi J, Jahromi M, Zeynab S, Mohammad S. Thermodynamic performance analysis of three solid oxide fuel cell and gas microturbine hybrid systems for application in auxiliary power units. Clean Technol Environ Policy 2018;20:1047–60. https://doi.org/10.1007/s10098-018-1534-2.

[80] Pirkandi J, Ommian M. Thermo-Economic Operation Analysis of SOFC-GT Combined Hybrid System for Application in Power Generation Systems. J Electrochem Energy Convers Storage 2019;16:1–12. https://doi.org/10.1115/1.4040056.

[81] Hedberg G, Hamilton R, McLarty D. Design and performance analysis of a de-coupled solid oxide fuel cell gas turbine hybrid. Int J Hydrogen Energy 2020;45:30980–93. https://doi.org/10.1016/j.ijhydene.2020.08.084.

[82] Weil KS. The state-of-the-art in sealing technology for solid oxide fuel cells. Jom 2006;58:37–44. https://doi.org/10.1007/s11837-006-0052-6.

[83] Willich C, Westner C, Seidler S, Leucht F. Pressurized Solid Oxide Fuel Cells: Operational Behavior. CoreKmiOpenAcUk 2018.

[84] Rossi I, Traverso A, Hohloch M, Huber A, Tucker D. Physics-Based Dynamic Models of Three SOFC/GT Emulator Test Rigs. J Eng Gas Turbines Power 2018;140:1–10. https://doi.org/10.1115/1.4038152.

[85] Azizi MA, Brouwer J. Progress in solid oxide fuel cell-gas turbine hybrid power systems : System design and analysis , transient operation , controls and optimization. Appl Energy 2018;215:237–89. https://doi.org/10.1016/j.apenergy.2018.01.098.

[86] Huang Y, Turan A. Mechanical equilibrium operation integrated modelling of hybrid SOFC e GT systems : Design analyses and off-design optimization. Energy 2020;208:118334. https://doi.org/10.1016/j.energy.2020.118334.

[87] Kandepu R, Imsland L, Foss BA, Stiller C, Thorud B, Bolland O. Modeling and control of a SOFC-GT-based autonomous power system 2007;32:406–17. https://doi.org/10.1016/j.energy.2006.07.034.

[88] Chen J, Liang M, Zhang H, Weng S. ScienceDirect Study on control strategy for a SOFC-GT hybrid system with anode and cathode recirculation loops. Int J Hydrogen Energy 2017;42:29422–32. https://doi.org/10.1016/j.ijhydene.2017.09.165.

[89] Chen J, Li J, Zhou D, Zhang H, Weng S. Control strategy design for a SOFC-GT hybrid system equipped with anode and cathode recirculation ejectors. Appl Therm Eng 2018;132:67–79. https://doi.org/10.1016/j.applthermaleng.2017.12.079.

[90] Ferrari ML. Solid oxide fuel cell hybrid system : Control strategy for stand-alone configurations. J Power Sources 2011;196:2682–90. https://doi.org/10.1016/j.jpowsour.2010.11.029.

[91] Zhou N, Yang C, Tucker D. Evaluation of Cathode Air Flow Transients in a SOFC / GT Hybrid System Using Hardware in the Loop Simulation 2015;12:1–7. https://doi.org/10.1115/1.4028950.

[92] Emami T, Tsai A, Tucker D. Decentralized PID Controller Design for SOFC-GT. Proc ASME 2020 Power Conf 2020;POWER2020.

[93] Zaccaria V, Tucker D, Traverso A, Pezzini P, Bryden KM. Active Control of Fuel Cell Degration in an SOFC/GT Hybrid System. Proc ASME Turbo Expo 2017 Turbomach Tech Conf Expo 2017;GT2017.

[94] Mueller F, Gaynor R, Auld AE, Brouwer J, Jabbari F, Samuelsen GS. Synergistic integration of a gas turbine and solid oxide fuel cell for improved transient capability 2008;176:229–39. https://doi.org/10.1016/j.jpowsour.2007.10.081.

[95] Incropera FP, DeWitt DP. Fundamentals of Heat and Mass Transfer 1996:890. https://doi.org/10.1016/j.applthermaleng.2011.03.022.

[96] Cooke DH. On Prediction of Off-Design Multistage Turbine Pressures by Stodola's Ellipse. J Eng Gas Turbines Power 1985;107:596. https://doi.org/10.1115/1.3239778.

[97] Achenbach E, Riensche E. Methane/steam reforming kinetics for solid oxide fuel cells 1994;7753:0–5.

[98] Eichman JD, Mueller F, Tarroja B, Schell LS, Samuelsen S. Exploration of the integration of renewable resources into California's electric system using the Holistic Grid Resource Integration and Deployment (HiGRID) tool. Energy 2013;50:353–63. https://doi.org/10.1016/j.energy.2012.11.024.

[99] McLarty D, Brouwer J, Samuelsen S. A spatially resolved physical model for transient system analysis of high temperature fuel cells. Int J Hydrogen Energy 2013;38:7935–46. https://doi.org/10.1016/j.ijhydene.2013.04.087.

[100] Ebrahimi S, Mac Kinnon M, Brouwer J. California end-use electrification impacts on carbon neutrality and clean air. Appl Energy 2018;213:435–49. https://doi.org/10.1016/j.apenergy.2018.01.050.

[101] EPA. AP 42, Fifth Edition Compilation of Air Pollutant Emission Factors, Volume 1: Stationary and Point Sources. AP 42, Fifth Ed Compil Air Pollut Emiss Factors, Vol 1 Station Point Sources 1995:1–10.

[102] Xu Z, Di Vittorio A, Chang A. Evaluating and projecting of climate extreme events using

a variable-resolution global climate model (VR-CSM). AGU Fall Meet., 2021.

[103] Masters GM. Renewable and Efficient Electric Power Systems. 2004. https://doi.org/10.1002/0471668826.

[104] Abdalla AM, Hossain S, Azad AT, Petra PMI, Begum F, Eriksson SG, et al. Nanomaterials for solid oxide fuel cells: A review. Renew Sustain Energy Rev 2018;82:353–68. https://doi.org/10.1016/j.rser.2017.09.046.

[105] Fang Q, de Haart U, Schäfer D, Thaler F, Rangel-Hernandez V, Peters R, et al. Degradation Analysis of an SOFC Short Stack Subject to 10,000 h of Operation. J Electrochem Soc 2020;167:144508. https://doi.org/10.1149/1945-7111/abc843.

[106] Zarabi Golkhatmi S, Asghar MI, Lund PD. A review on solid oxide fuel cell durability: Latest progress, mechanisms, and study tools. Renew Sustain Energy Rev 2022;161:112339. https://doi.org/10.1016/j.rser.2022.112339.

[107] Aguiar P, Adjiman CS, Brandon NP. Anode-supported intermediate temperature direct internal reforming solid oxide fuel cell. I: Model-based steady-state performance. J Power Sources 2004;138:120–36. https://doi.org/10.1016/j.jpowsour.2004.06.040.

[108] Ansaldo Energia. AE-T100 Natural Gas Micro Turbine 2019.

[109] Farmer R, Jaeger H, Janson J. Gas Turbine World 2014.

[110] States U. US Department of Energy, ‘Combined Heat and Power Technology Fact Sheet Series: Microturbines.’’, DOE/EE-1329 July 2016.’ 2016:1–4.

[111] Sabia G, Heinze C, Alobaid F, Martelli E, Epple B. ASPEN dynamics simulation for combined cycle power plant – Validation with hot start-up measurement. Energy 2019;187:115897. https://doi.org/10.1016/j.energy.2019.115897.

14. Appendix

14.1 Turbomachinery Performance Maps

The compression/expansion efficiencies and flow rates are determined from empirical correlations using RPM, pressure ratio and inlet temperature. The empirical correlations that determine flow rate and compression/expansion efficiency are formatted in forms of performance maps.

$$\dot{n}_{out}, \eta_C = f(N_{RPM}, Pr, T_{in})$$

$$\dot{n}_{out}, \eta_T = f(N_{RPM}, Pr, T_{in})$$

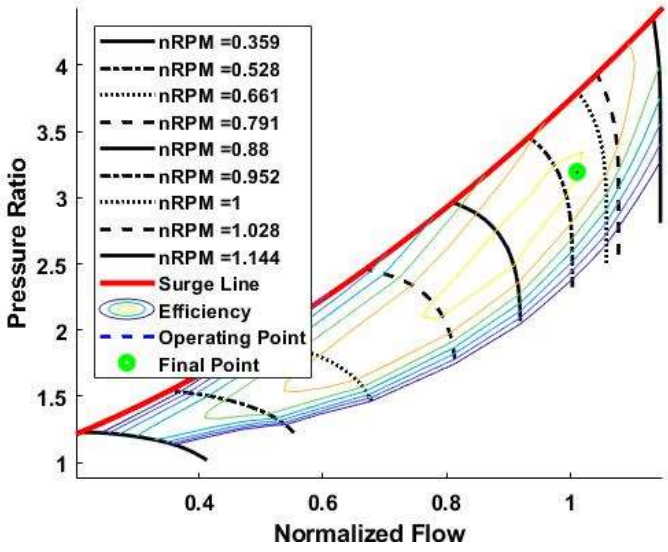

FIGURE 52: COMPRESSOR PERFORMANCE MAP USED IN THIS DISSERTATION

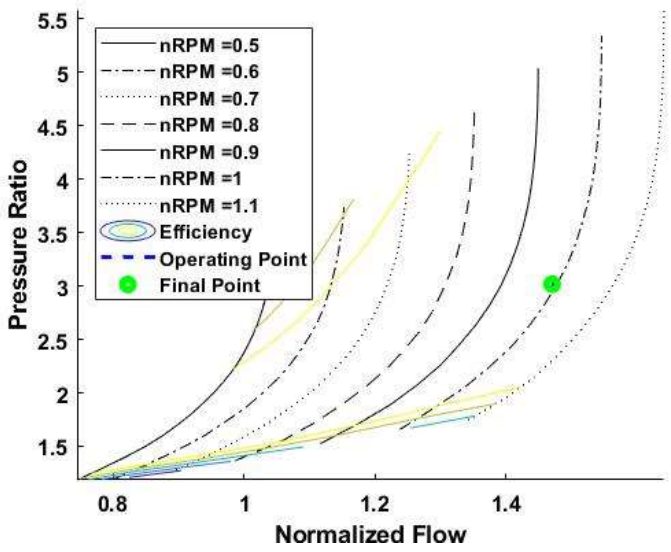

FIGURE 53: TURBINE PERFORMANCE MAP USED IN THIS DISSERTATION

14.2 Table of Thermodynamic Properties for Flows

TABLE 12: THERMODYNAMIC PROPERTIES OF FLOWS FOR NATURAL GAS SIMULATION

	Temp (K)	Temp (°C)	Pressure (kPa)	MassFlow (kg/s)	MolarFlow (kmol/s)	mxLHV	CH4	CO	CO2	H2	H2O	N2	O2
1	298.000	25.0	101.000	0.159	1.000	0.000	0.000	0.000	0.000	0.000	0.000	0.790	0.210
2	495.839	222.8	322.764	0.159	0.006	0.000	0.000	0.000	0.000	0.000	0.000	0.790	0.210
3	905.322	632.3	321.764	0.159	0.006	0.000	0.000	0.000	0.000	0.000	0.000	0.790	0.210
4	905.322	632.3	321.764	0.085	0.003	0.000	0.000	0.000	0.000	0.000	0.000	0.790	0.210
5	905.322	632.3	321.764	0.074	0.003	0.000	0.000	0.000	0.000	0.000	0.000	0.790	0.210
6	1099.706	826.7	321.764	0.074	0.003	0.000	0.000	0.000	0.000	0.000	0.000	0.790	0.210
7	997.100	724.1	319.764	0.159	0.006	0.000	0.000	0.000	0.000	0.000	0.000	0.790	0.210
8	1025.213	752.2	315.764	0.148	0.005	0.000	0.000	0.000	0.000	0.000	0.000	0.845	0.155
9	1154.289	881.3	310.765	0.163	0.006	0.000	0.000	0.000	0.038	0.000	0.076	0.760	0.126
10	930.384	657.4	102.999	0.163	0.006	0.000	0.000	0.000	0.038	0.000	0.076	0.760	0.126
11	553.125	280.1	101.999	0.163	0.006	0.000	0.000	0.000	0.038	0.000	0.076	0.760	0.126
12	549.953	277.0	101.000	0.163	0.006	0.000	0.000	0.000	0.038	0.000	0.076	0.760	0.126
14	288.000	15.0	101.000	0.003	0.000	0.000	0.000	0.000	0.000	0.000	1.000	0.000	0.000
15	399.583	126.6	101.000	0.003	0.000	0.000	0.000	0.000	0.000	0.000	1.000	0.000	0.000
16	288.000	15.0	350.000	0.004	0.000	0.174	0.977	0.000	0.011	0.000	0.000	0.011	0.000
17	653.975	381.0	340.249	0.026	0.001	0.236	0.180	0.065	0.210	0.129	0.411	0.005	0.000
18	978.629	705.6	316.773	0.026	0.001	0.236	0.180	0.065	0.210	0.129	0.411	0.005	0.000
19	847.093	574.1	315.770	0.026	0.001	0.242	0.138	0.057	0.232	0.249	0.319	0.005	0.000
20	1095.673	822.7	315.764	0.038	0.002	0.102	0.000	0.080	0.255	0.158	0.503	0.004	0.000
21	1095.673	822.7	313.765	0.015	0.001	0.041	0.000	0.080	0.255	0.158	0.503	0.004	0.000
22	1095.673	822.7	313.765	0.023	0.001	0.061	0.000	0.080	0.255	0.158	0.503	0.004	0.000
23	663.421	390.4	305.215	0.023	0.001	0.061	0.000	0.080	0.255	0.158	0.503	0.004	0.000
24	669.951	397.0	340.249	0.023	0.001	0.061	0.000	0.080	0.255	0.158	0.503	0.004	0.000
25	288.000	15.0	350.000	0.000	0.000	0.000	0.977	0.000	0.011	0.000	0.000	0.011	0.000

TABLE 13: THERMODYNAMIC PROPERTIES OF FLOWS FOR 41.7 % HYDROGEN SIMULATION

	Temp (K)	Temp (°C)	Pressure (kPa)	MassFlow (kg/s)	MolarFlow (kmol/s)	mxLHV	CH4	CO	CO2	H2	H2O	N2	O2
1	298.000	25.000	101.000	0.159	1.000	0.000	0.000	0.000	0.000	0.000	0.000	0.790	0.210
2	498.651	225.651	327.818	0.159	0.006	0.000	0.000	0.000	0.000	0.000	0.000	0.790	0.210
3	953.886	680.886	326.820	0.159	0.006	0.000	0.000	0.000	0.000	0.000	0.000	0.790	0.210
4	953.886	680.886	326.820	0.135	0.005	0.000	0.000	0.000	0.000	0.000	0.000	0.790	0.210
5	953.886	680.886	326.820	0.023	0.001	0.000	0.000	0.000	0.000	0.000	0.000	0.790	0.210
6	1240.369	967.369	326.820	0.023	0.001	0.000	0.000	0.000	0.000	0.000	0.000	0.790	0.210
7	997.102	724.102	324.826	0.159	0.006	0.000	0.000	0.000	0.000	0.000	0.000	0.790	0.210
8	1067.015	794.015	320.836	0.147	0.005	0.000	0.000	0.000	0.000	0.000	0.000	0.845	0.155
9	1218.736	945.736	315.832	0.162	0.006	0.000	0.000	0.000	0.032	0.000	0.087	0.755	0.126
10	980.955	707.955	103.006	0.162	0.006	0.000	0.000	0.000	0.032	0.000	0.087	0.755	0.126
11	564.176	291.176	102.003	0.162	0.006	0.000	0.000	0.000	0.032	0.000	0.087	0.755	0.126
12	560.886	287.886	101.000	0.162	0.006	0.000	0.000	0.000	0.032	0.000	0.087	0.755	0.126
14	288.000	15.000	101.000	0.003	0.000	0.000	0.000	0.000	0.000	0.000	1.000	0.000	0.000
15	404.183	131.183	101.000	0.003	0.000	0.000	0.000	0.000	0.000	0.000	1.000	0.000	0.000
16	288.000	15.000	350.000	0.003	0.000	0.178	0.561	0.000	0.011	0.417	0.000	0.011	0.000
17	653.975	380.975	340.248	0.026	0.001	0.235	0.134	0.044	0.163	0.218	0.434	0.007	0.000
18	974.162	701.162	322.167	0.026	0.001	0.235	0.134	0.044	0.163	0.218	0.434	0.007	0.000
19	860.947	587.947	321.059	0.026	0.001	0.241	0.104	0.048	0.174	0.297	0.371	0.006	0.000
20	1098.759	825.759	320.836	0.037	0.002	0.095	0.000	0.058	0.211	0.155	0.570	0.005	0.000
21	1098.759	825.759	320.836	0.015	0.001	0.038	0.000	0.058	0.211	0.155	0.570	0.005	0.000
22	1098.759	825.759	320.836	0.022	0.001	0.057	0.000	0.058	0.211	0.155	0.570	0.005	0.000
23	662.885	389.885	305.277	0.022	0.001	0.057	0.000	0.058	0.211	0.155	0.570	0.005	0.000
24	669.810	396.810	340.248	0.022	0.001	0.057	0.000	0.058	0.211	0.155	0.570	0.005	0.000
25	288.000	15.000	350.000	0.000	0.000	0.178	0.561	0.000	0.011	0.417	0.000	0.011	0.000

TABLE 14: THERMODYNAMIC PROPERTIES OF FLOWS FOR 72.9 % HYDROGEN

	Temp (K)	Temp (°C)	Pressure (kPa)	MassFlow (kg/s)	MolarFlow (kmol/s)	mxLHV	CH4	CO	CO2	H2	H2O	N2	O2
1	298.0	25.0	101.000	28.840	1.000	0.000	0.000	0.000	0.000	0.000	0.000	0.790	0.210
2	500.5	227.5	331.055	0.159	0.005	0.000	0.000	0.000	0.000	0.000	0.000	0.790	0.210
3	988.3	715.3	330.058	0.159	0.005	0.000	0.000	0.000	0.000	0.000	0.000	0.790	0.210
4	988.3	715.3	330.058	0.154	0.005	0.000	0.000	0.000	0.000	0.000	0.000	0.790	0.210
5	988.3	715.3	330.058	0.005	0.000	0.000	0.000	0.000	0.000	0.000	0.000	0.790	0.210
6	1271.6	998.6	330.058	0.005	0.000	0.000	0.000	0.000	0.000	0.000	0.000	0.790	0.210
7	997.1	724.1	328.065	0.159	0.005	0.000	0.000	0.000	0.000	0.000	0.000	0.790	0.210
8	1155.9	882.9	324.079	0.147	0.005	0.000	0.000	0.000	0.000	0.000	0.000	0.846	0.154
9	1264.0	991.0	319.055	0.162	0.006	0.000	0.000	0.000	0.022	0.000	0.102	0.749	0.127
10	1016.3	743.3	103.022	0.162	0.006	0.000	0.000	0.000	0.022	0.000	0.102	0.749	0.127
11	572.9	299.9	102.011	0.162	0.006	0.000	0.000	0.000	0.022	0.000	0.102	0.749	0.127
12	569.6	296.6	101.000	0.162	0.006	0.000	0.000	0.000	0.022	0.000	0.102	0.749	0.127
13													
14	288.0	15.0	101.000	0.003	0.000	0.000	0.000	0.000	0.000	0.000	1.000	0.000	0.000
15	407.8	134.8	101.000	0.003	0.000	0.000	0.000	0.000	0.000	0.000	1.000	0.000	0.000
16	288.0	15.0	350.000	0.003	0.000	0.181	0.248	0.000	0.011	0.729	0.000	0.011	0.000
17	654.0	381.0	340.249	0.025	0.002	0.219	0.076	0.017	0.106	0.303	0.488	0.009	0.000
18	971.4	698.4	325.885	0.025	0.002	0.219	0.076	0.017	0.106	0.303	0.488	0.009	0.000
19	874.2	601.2	324.620	0.025	0.002	0.225	0.056	0.031	0.106	0.349	0.450	0.009	0.000
20	1107.6	834.6	324.079	0.037	0.002	0.063	0.000	0.025	0.149	0.113	0.706	0.008	0.000
21	1107.6	834.6	322.090	0.015	0.001	0.025	0.000	0.025	0.149	0.113	0.706	0.008	0.000
22	1107.6	834.6	322.090	0.022	0.001	0.038	0.000	0.025	0.149	0.113	0.706	0.008	0.000
23	662.3	389.3	305.078	0.022	0.001	0.038	0.000	0.025	0.149	0.113	0.706	0.008	0.000
24	668.3	395.3	340.249	0.022	0.001	0.038	0.000	0.025	0.149	0.113	0.706	0.008	0.000
25	288.0	15.0	350.000	0.000	0.000	0.000	0.248	0.000	0.011	0.729	0.000	0.011	0.000

14.3 Dynamic Simulation – Step Change

TABLE 15: PROPORTIONAL AND INTEGRAL GAINS FOR EACH CONTROL LOOP

	Proportional Gain	Integral Gain
1	5	1e-1

2	1e2	1e1
3	2	1e-1
4	0	1
5	0	0
6	1e8	1e5
7	0	0

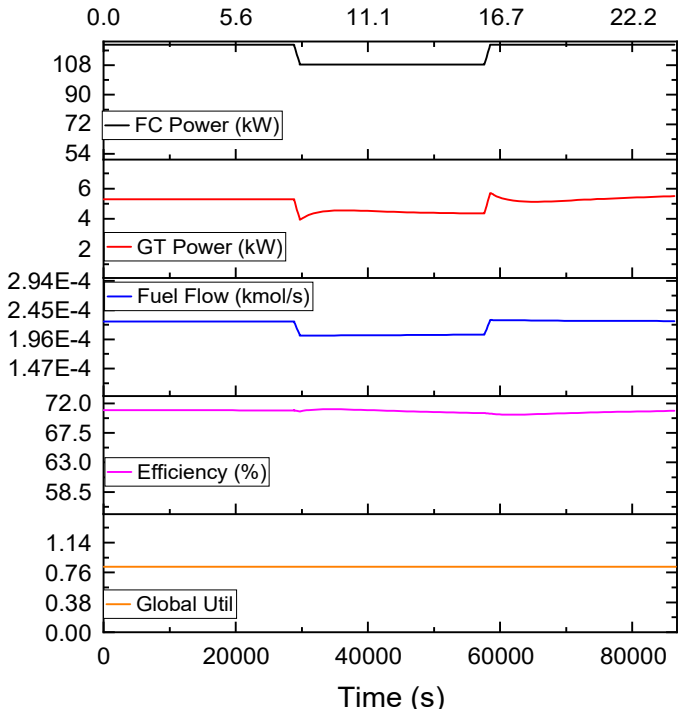

FIGURE 54: HYBRID SYSTEM CHARACTERISTICS SIMULATING 100-90-100% STEP CHANGE

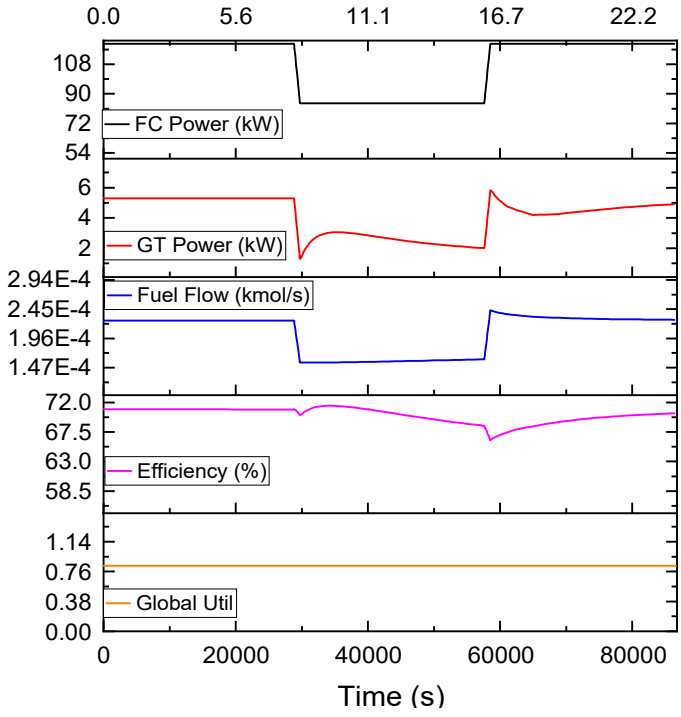

FIGURE 55:HYBRID SYSTEM CHARACTERISTICS SIMULATING 100-70-100% STEP CHANGE

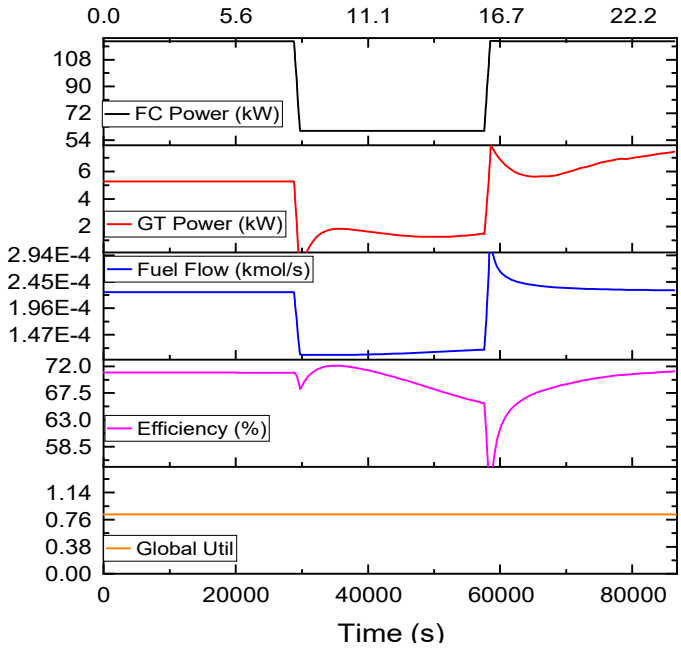

FIGURE 56:HYBRID SYSTEM CHARACTERISTICS SIMULATING 100-50-100% STEP CHANGE

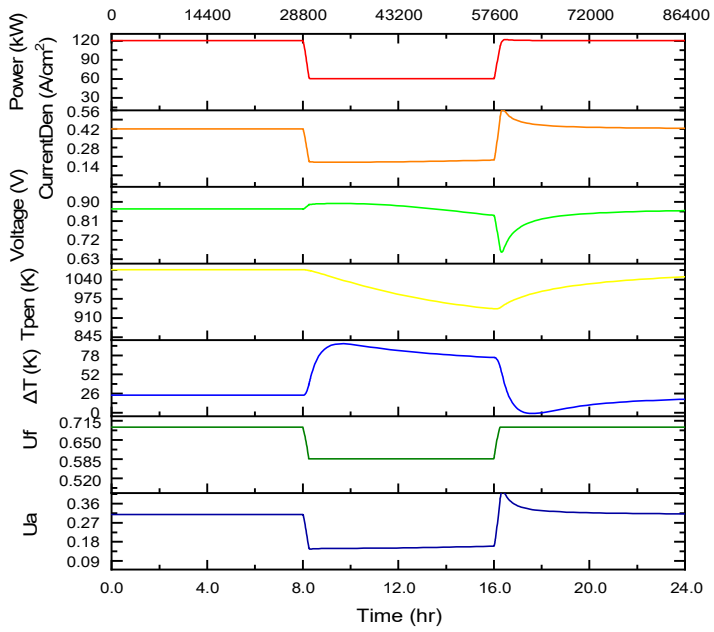

FIGURE 57: FUEL CELL CHARACTERISTICS SIMULATING 100-50-100% STEP CHANGE

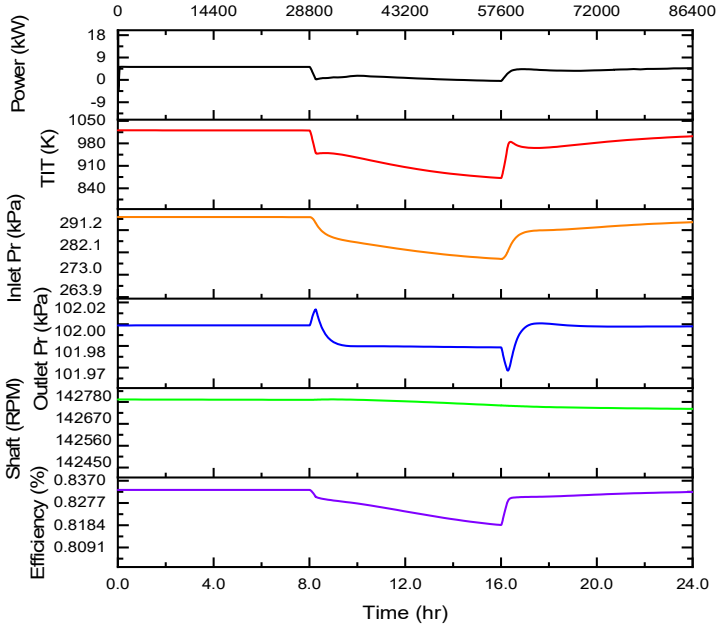

FIGURE 58:GAS TURBINE CHARACTERISTICS SIMULATING 100-50-100% STEP CHANGE

14.4 Dynamic Simulation – Complementing Solar and Wind

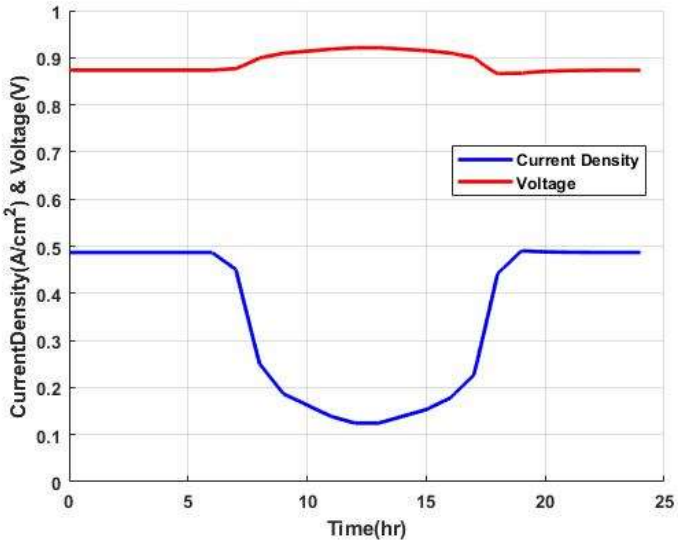

FIGURE 59: CURRENT DENSITY AND VOLTAGE FOR HYBRID SYSTEM COMPLEMENTING SOLAR ON A SUNNY DAY

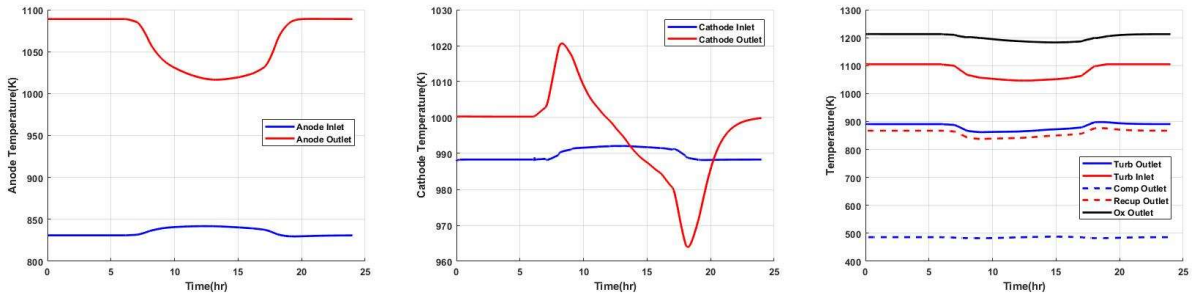

FIGURE 60: FLOW TEMPERATURE PROFILES FOR HYBRID SYSTEM COMPLEMENTING SOLAR ON A SUNNY DAY

(LEFT: ANODE, MID: CATHODE, RIGHT: OTHERS)

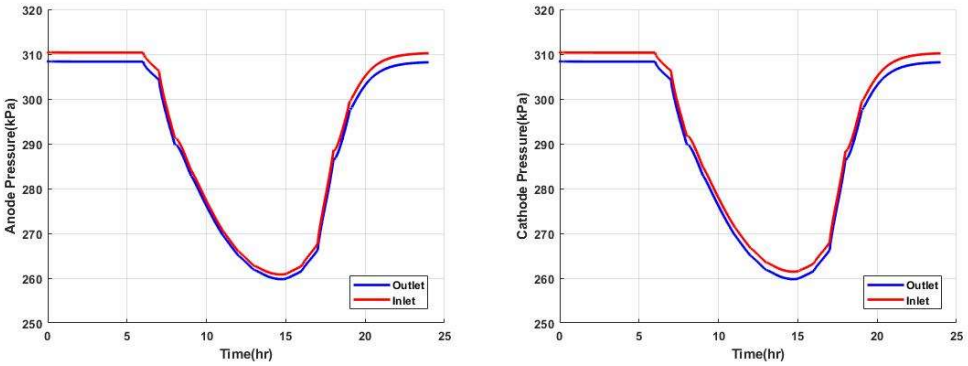

FIGURE 61: PRESSURE DYNAMICS FOR HYBRID SYSTEM COMPLEMENTING SOLAR ON A SUNNY DAY

(LEFT: ANODE, RIGHT: CATHODE)

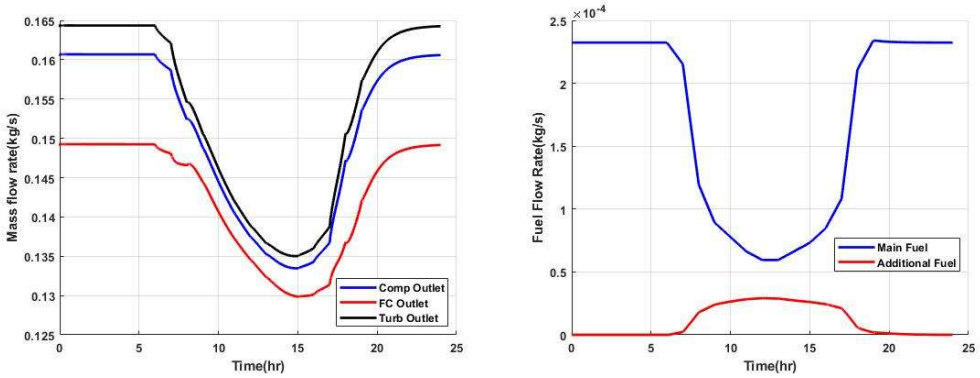

FIGURE 62: FLOW RATES FOR HYBRID SYSTEM COMPLEMENTING SOLAR ON A SUNNY DAY

(LEFT: MASS FLOW RATES, RIGHT: FUEL FLOW RATES)

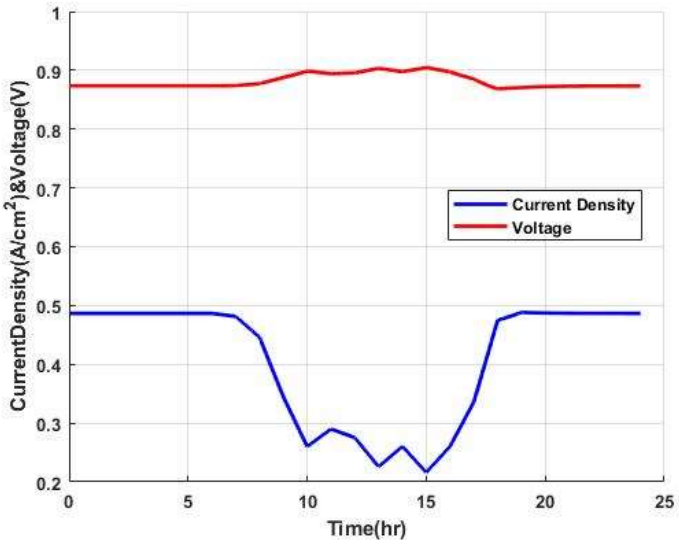

FIGURE 63: CURRENT DENSITY AND VOLTAGE FOR HYBRID SYSTEM COMPLEMENTING SOLAR ON A CLOUDY DAY

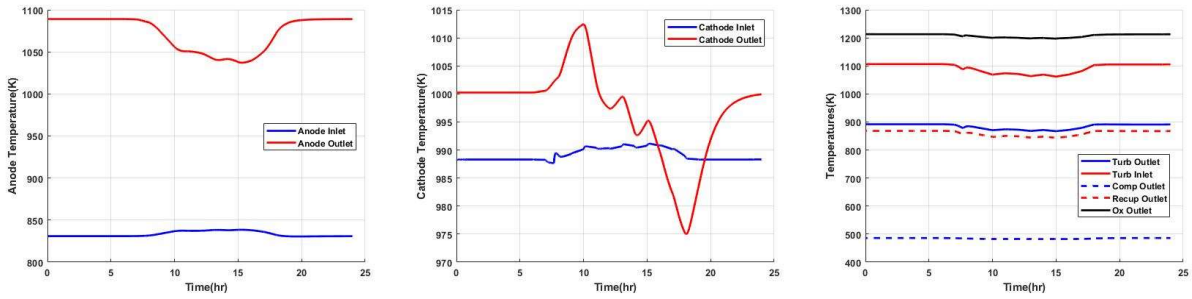

FIGURE 64: FLOW TEMPERATURE PROFILES FOR HYBRID SYSTEM COMPLEMENTING SOLAR ON A CLOUDY DAY

(LEFT: ANODE, MID: CATHODE, RIGHT: OTHERS)

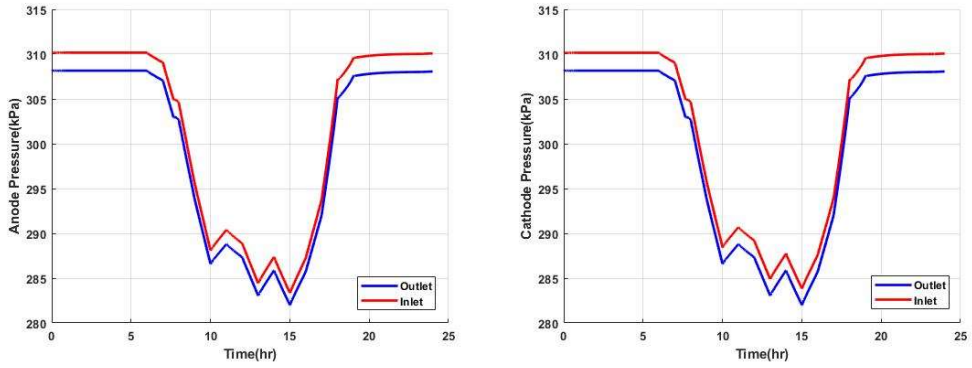

FIGURE 65: PRESSURE DYNAMICS FOR HYBRID SYSTEM COMPLEMENTING SOLAR ON A CLOUDY DAY

(LEFT: ANODE, RIGHT: CATHODE)

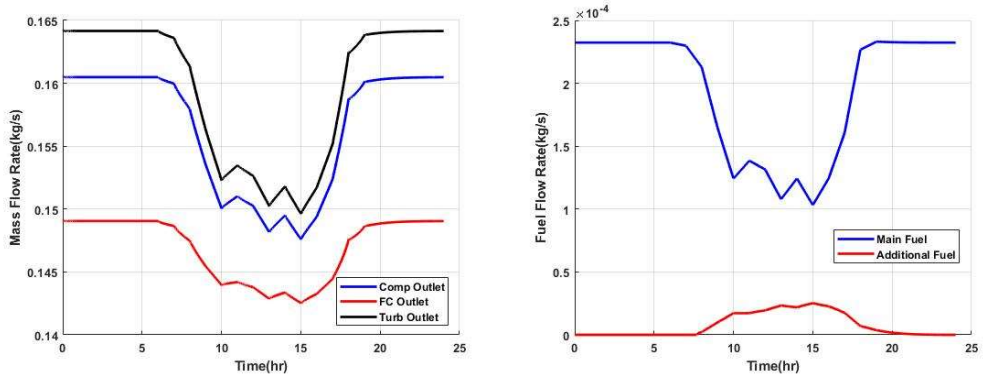

FIGURE 66: FLOW RATES FOR HYBRID SYSTEM COMPLEMENTING SOLAR ON A CLOUDY DAY

(LEFT: MASS FLOW RATES, RIGHT: FUEL FLOW RATES)

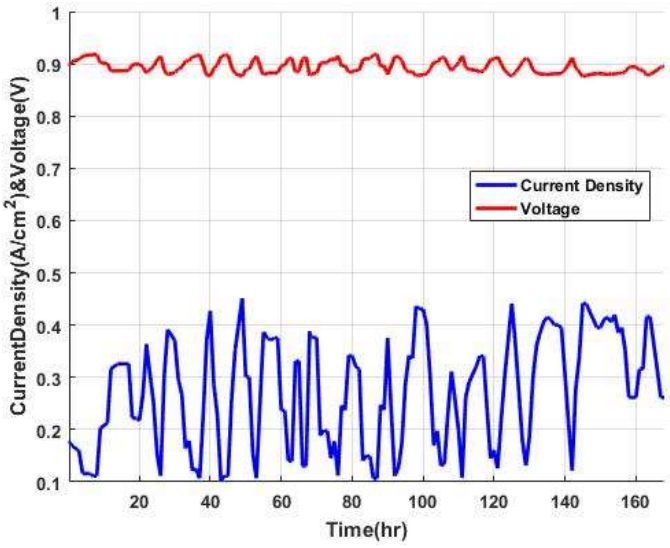

FIGURE 67: CURRENT AND VOLTAGE FOR HYBRID SYSTEM COMPLEMENTING WIND

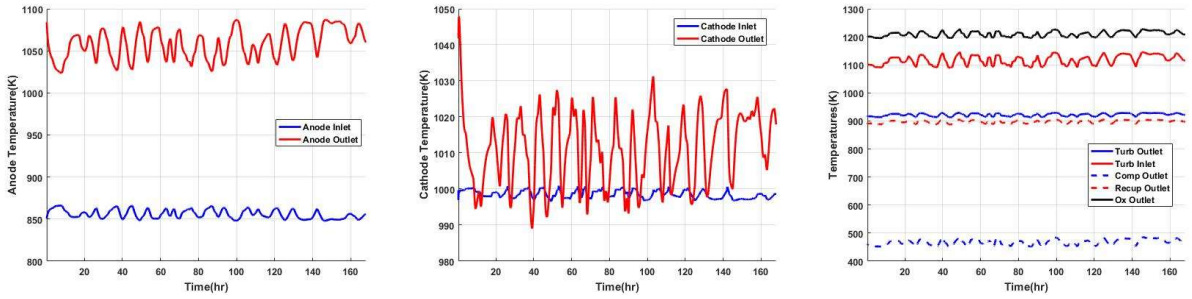

FIGURE 68: FLOW TEMPERATURE PROFILES FOR HYBRID SYSTEM COMPLEMENTING WIND

(LEFT: ANODE, MID: CATHODE, RIGHT: OTHERS)

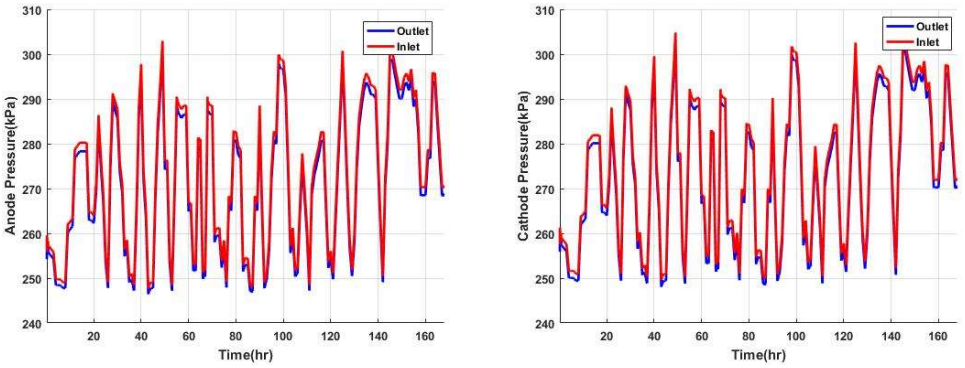

FIGURE 69: PRESSURE DYNAMICS FOR HYBRID SYSTEM COMPLEMENTING WIND

(LEFT: ANODE, RIGHT: CATHODE)

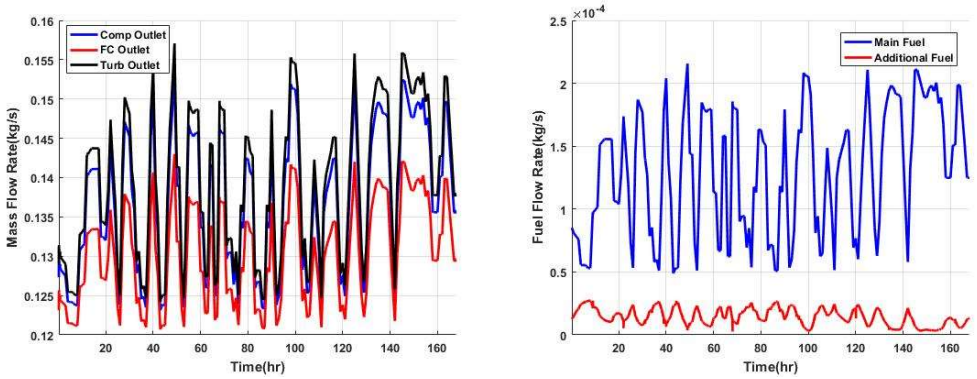

FIGURE 70: FLOW RATES FOR HYBRID SYSTEM COMPLEMENTING WIND

(LEFT: MASS FLOW RATES, RIGHT: FUEL FLOW RATES)